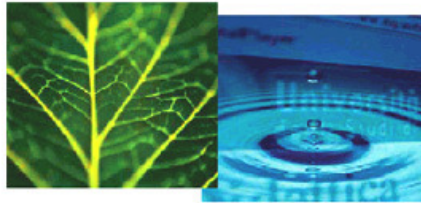


PhD Dissertation



International Doctorate School in Information and
Communication Technologies

DISI - University of Trento

SIMULATION AND CHARACTERIZATION OF
SINGLE PHOTON DETECTORS FOR
FLUORESCENCE LIFETIME SPECTROSCOPY AND
GAMMA-RAY APPLICATIONS

Michele Benetti

Advisor:

Prof. Gian-Franco Dalla Betta

Università degli Studi di Trento

Co-Advisor:

Dr. David Stoppa

Fondazione Bruno Kessler

April 2012

Abstract

*Gamma-ray and Fluorescence Lifetime Spectroscopies are driving the development of non-imaging silicon photon sensors and, in this context, **Silicon Photo-Multipliers (SiPM)s** are leading the starring role. They are 2D array of optical diodes called **Single Photon Avalanche Diodes (SPAD)s**, and are normally fabricated with a dedicated silicon process. **SPADs** amplify the charge produced by the single absorbed photon in a way that recalls the avalanche amplification exploited in **Photo-Multiplier Tubes (PMT)s**. Recently 2D arrays of **SPADs** have been realized also in standard **CMOS** technology, paving the way to the realization of completely custom sensors that can host ancillary electronic and digital logic on-chip. The designs of scientific apparatus have been influenced for years by the bulky **PMT**-based detectors. An overwhelming interest in both **SiPMs** and **CMOS SPADs** lies in the possibility of displacing these small sensors realizing new detectors geometries. This thesis examines the potential deployment of **SiPM**-based detector in an apparatus built for the study of the **Time-Of-Flight (TOF)** of Positronium (**Ps**) and the displacement of 2D array of **CMOS SPADs** in a lab-on-chip apparatus for Fluorescence Lifetime Spectroscopy. The two design procedures are performed using Monte-Carlo simulations. Characterizations of the two sensor have been carried out, allowing for a performance evaluation and a validation of the two design procedures.*

Keywords [SiPM, CMOS SPAD, Monte-Carlo, Fluorescence Lifetime Spectroscopy, Gamma-ray Spectroscopy]

Contents

1	Introduction	1
1.1	Photon-starved Applications	1
1.1.1	Background filtering	2
1.1.2	Small dimension scale system integration.	5
1.1.3	Large dimension scale system integration.	6
1.1.4	Sensitivity.	7
1.2	Single-Photon Sensors	8
1.2.1	SiPM	14
1.2.2	CMOS SPAD arrays	16
1.3	Fluorescence lifetime Spectroscopy	18
1.4	Positron Emission Tomography detectors	21
1.5	Time of Flight of positronium	22
1.6	Thesis content	24
1.7	Innovative Aspects	26
1.8	Materials and Methods	26
2	The NPD detector	29
2.1	DCR	31
2.2	Optical Cross-Talk	32
2.3	Dynamic Range	33
2.4	Time Gating	34
2.5	Device Data Throughput	35

2.6	Acquisition system	36
2.7	Fluorescent measurements	37
2.8	Conclusions	38
3	Lab-on-chip design	39
3.1	Simulation results	42
3.2	Conclusions	45
4	CMOS for gamma detection	47
4.1	Coupling procedure	48
4.2	Optical Glue	51
4.3	Gamma detection	52
4.4	Conclusions	56
5	Light yield in crystals	59
5.1	Case history	60
5.2	PDE and crystals	63
5.2.1	Optical Simulation	66
5.2.2	Energy Deposition	68
5.2.3	Relative light distribution at crystal interface	69
5.2.4	Light distribution at sensor interface	70
5.2.5	Light transport inside SiPM coating	71
5.2.6	Simulation resume	71
5.3	Conclusions	71
6	Energy deposition	77
6.1	SLitrani structure	77
6.2	Cross section calculation	78
6.3	Example of calculations	82
6.4	Conclusions	82

7 TOF of Positronium	85
7.1 TOF Measurements	90
7.2 Figures of Merit	94
7.3 Discussion	98
7.3.1 Choice of the shield thickness	99
7.3.2 Distance from the chamber wall	101
7.3.3 Temperature of the sample	103
7.4 Conclusions	104
8 Conclusions	105
8.1 Future Perspectives	106
Bibliography	111

Chapter 1

Introduction

The outline of this introductory chapter can be derived reading in reverse order the title “*Simulation and characterization of Single Photon Detectors for Fluorescence Lifetime Spectroscopy and Gamma-ray applications*”. At first the reader will find two brief overviews: the first is dedicated to photon-starved applications that are related to Fluorescence Lifetime and *Gamma-ray* (γ -ray) spectroscopies while the second one is dedicated to Single-Photon Detectors. The purpose of the first overview is to familiarize the reader with the problems that are faced by the two types of Single-Photon Detectors used in this thesis. The purpose of the second overview is to introduce the two detectors providing figures of merit that can be useful in their evaluation. At the end of the two overviews the three applications that have been studied during this thesis are briefly described. The last two sections introduce the thesis content underlining its innovative aspects.

1.1 Photon-starved Applications

In a large number of measurements the revealed physical quantity is related to the detection of a very few number of photons. If this characteristic is one of the main technological issues of the measurement, the application

is called photon-starved. Photon-starved applications need single-photon sensors that are able to detect, with a sufficiently high probability, the single photons impinging onto their surfaces. Some photon-starved applications require also the recording of the arrival time of the photons and are then called *Time Correlated Single Photon Counting* (TCSPC) applications. Nowadays the list of both photon-starved and TCSPC applications has items in many science fields. We can divide the items in categories following the most demanding technical challenge that has to be faced in the application. Then we can select from this list the items that are related to the two main subjects of this thesis that are Fluorescence lifetime and γ -ray spectroscopies. The resulting list, divided by main issues, should appear as follows [1, 2, 3]:

1.1.1 Background filtering

The main issue in the applications that belong to this category is the distinction of the signal from the background. This distinction requires the implementation of some type of filter. The two most used filters are color filters and time filters. The color filter selects photons according to their wavelength while time filter selects photons according to their time of arrival. Example of applications in this category are:

- *Single-molecule spectroscopy in solution*: In the past decade there has been a considerable research effort to push the sensitivity of single photon detectors in order to permit the detection of the fluorescence produced by a single excited molecule in a solution [4, 5]. The single-molecule sensitivity in a solution is an ability that should greatly improve applications such as *Confocal Laser Scanning Microscopy* (CLSM), *Near-field Scanning Optical Microscopy* (NSOM), *Fluorescence Lifetime Imaging Microscopy* (FLIM) and *Förster Resonance Energy*

Transfer (FRET) [6, 7]. Molecules in the solution are excited to fluorescent states through the use of light sources (see section 1.3) that cause also unwanted background from the medium surrounding the target molecule. A large number of materials are fluorescent especially when excited with short wavelengths (biological tissues, oils, minerals, some type of glasses and ceramic). Therefore detected photons can arise from the solvent through autofluorescence¹ or also from scattering phenomena, such as elastic Rayleigh and inelastic Raman scattering [8]. The number of photons produced by scattering and solvent fluorescence is orders of magnitude larger than the single-molecule signal, requiring a high filtering efficiency.

- *Raman Scattering Spectroscopy*: The spectroscopy in the domain of the wavelength of the scattered photons has virtually many possible applications. Indeed a shift in the wavelength of a small portion of scattered photons can be observed in almost all molecules, in both gaseous and liquid state, and in almost all solids, when these samples are excited with monochromatic laser sources. This inelastic scattering, namely *Raman scattering*, gives fingerprint information of the vibrational frequency modes of molecules and solids but it is feasible only if two main difficulties are solved. The first difficult task is the separation of the inelastically scattered light from the larger portion of elastic (Rayleigh) scattered photons. This is usually overcome with highly efficient color filters such as holographic gratings. Unfortunately the second difficulty arises if the environment is fluorescent. This is challenging because the probability, namely the *cross-section*, of a Raman interaction is typically 10^{-6} times lower than the proba-

¹The term *autofluorescence* is normally used to indicate all the unwanted sources of fluorescence in an experiment.

bility of a fluorescent absorption and thus the shift in wavelength due to Raman scattering is hardly distinguishable in the stronger fluorescent emission. As a consequence, Raman spectroscopy is nowadays relegated to the analysis of non fluorescent specimen conducted in non fluorescent environment, practically only to the after-synthesis analysis of artificial non-fluorescent specimens. A filter that selects Raman scattering and neglects fluorescent emission can be obtained by harnessing the delay time between the two emissions. The Raman scattering is synchronous with the exciting light while the fluorescent emissions typically occurs some hundreds of *ps* after the excitation. Such a filter has been recently demonstrated [9] using fast excitation laser and fast time-gated detection.

- *Multi-spectral and Fluorescence Diffuse Optical Tomography (DOT)*: Time-filtering is also the main issue in DOT. In a typical DOT a pulsed light laser source, emitting in the near infrared wavelength range, is positioned on the patient skin. Detectors are located in the near proximity and detected photons are tagged with the time elapsed from emission to detection. Thanks to a light scatter model of the tissue, information about under-skin structures are extracted and, as example, some type of cancer as breast tumor [10] can be detected. The use of multi-spectral excitation and fluorescence spectroscopy greatly enhance this technique and the concentration of chemicals in the tissue can be better determined, allowing as an example the functional study of brain [11]. If the tissue is thin enough it is also possible to study the fraction of directly transmitted photons obtaining high-resolution images and tomography.

1.1.2 Small dimension scale system integration.

In this category all the applications that require the miniaturization of the detector can be grouped. Shrinking the sensor dimension gives rise to technological issues that are not only related to the realization of the detector itself but are also related to other aspects of the interface with the device. Consider as an example the data throughput. Single-photon applications inherently generate large amount of data being the elementary information associated to the arrival of a single-photon. If the detector dimension are shrunk a large number of detectors can be localized in a small area and data reduction at detector level is needed to manage the high data throughput.

- *DNA micro-array scanner and RNA:* These equipments were conceived in the first 90's [12] and became popular in few a years [13]. A DNA sample labeled by fluorescent dye is combined with a spotted 2D array of DNA probes whose arrangement is known and fixed at a high density on a glass plate or silicon substrate. In some cases a laser beam is used to scan the 2D array of probes and the resulting fluorescent intensity is measured to investigate the gene information. In other cases the 2D array of probes is coupled one-to-one to a 2D array of detectors. The second measurement geometry can be realized in compact devices, commonly called lab-on-chip [14]. Chapter 2 is dedicated to the characterization of a sensor for lab-on-chip applications. In-vitro assay is used for physical checkup diagnosis, and evaluation of drug efficiency by making use of the specific antigen/antibody reaction characteristics of tiny amounts of insulin, hormones, drugs and viruses that are contained in blood or urine. Single-Photon detectors are used to optically measure the amount of antigens labeled by radioisotopes

or fluorescent, chemiluminescent or bioluminescent substances.

1.1.3 Large dimension scale system integration.

If the detectors of the photon-starved application have to be placed in a given volume, an area or, more generally in a network of large dimension, issues related to the detector scalability have to be faced. This type of issues are for example: the management of the data throughput of the application, the inter-communication between the nodes of the detector network, the cost of the single detector, the cost of building and managing the network.

- **Positron Emission Tomography (PET):** PET is a tomography that reveals the distribution of radioactive tracers in patients or in laboratory animals [15]. The tracers are synthesized using isotopes that emits *positron* (e^+), the anti-matter counterpart of *electron* (e^-), during their β^+ -decays. The emitted e^+ travels inside the tissue until it forms an instable atom of *Positronium* (Ps) with an e^- [16]. The Ps can be formed as *para-positronium* (p -Ps) or *ortho-positronium* (o -Ps), depending on the mutual orientation of the spins of e^+ and e^- , and annihilates emitting γ -rays. Annihilations of p -Ps produce two γ -rays with an approximatively² equal distributed energy of 511 keV and propagating forming an angle of approximatively 180°. The two γ -rays travel out of the patient and likely deposit their energy in a ring of PET detectors, that will be described in section 1.4. The diameter of the rings range from several centimeters (small animal PET scanners) to ~ 90 cm (clinical PET scanners) and can host tens of PET

²due to differences in the momentum of the e^- s at annihilation, differences in the order of 1% in energy are registered as well as little deviations from collinearity

detectors with hundreds of read-out channels. All the read-out channels have to be promptly read after the detection of one of the two γ -rays searching the evidence of the signal of the second one.

1.1.4 Sensitivity.

Strong research efforts have been spent to increase the efficiency of photon sensor in detecting single-photon. But there are still physical phenomena that emit so little photons that their detection remains challenging and requires to minimize as much as possible the optical losses.

- *Cerenkov detectors*: Cerenkov photon emission occurs when a particle travels in a medium with a speed higher than the speed of light in that medium. The particle can be, as example, an e^- or a e^+ emitted during a β -decay of a radioactive compound in a tissue, or a recoil electron emitted during a γ -ray absorption in a scintillating crystal [17]. Recently [18, 19, 20] it has been demonstrated that it is possible to detect the Cerenkov emission of photons produced from e^+ traveling in mice tissues during *in-vivo* measurements. These pioneering works demonstrated the feasibility of a new technique (so far called *Cerenkov Luminescence Imaging* (CLI) [18]). Authors of cited works foresee that CLI should be used in association with PET. In particular it may be used to visualize the distribution of radiotracers with α -decay or β^- -decay. However the sensitivity of an optical CLI experiment for in vivo applications is expected to be much lower than the sensitivity of a PET scanner due to tissue absorption and scattering.

As an aside, it might be worth pointing out that many photon-starved applications (Quantum cryptography [2], Neutrino telescopes [21, 22],

Light Detection And Ranging (LIDAR), **Time of Flight (TOF)** of light [23, 24]) that are of prominent interest for their impact, dimension and fundings have not been listed because not correlated to γ -ray and fluorescence spectroscopy. However, they have many technological issues and possible solutions in common with the listed photon-starved applications. In the three sections 1.3, 1.4 and 1.5, which will follow, the three photon-starved applications that have been studied during this thesis are briefly described.

1.2 Single-Photon Sensors

Single-Photon Sensors became available after the first commercial [25] **Photo Multiplier Tube (PMT)** in late 1930s [26], and since this date **PMTs** have been the main actors of the single photon sensor market despite a huge research effort in developing new detectors and in pushing sensor performance. Performance is expressed in terms of:

- **Photon Detection Efficiency (PDE)**: A great research effort is focused on pushing the limits of the single-photon sensors in order to increase their single-photon detection efficiency. **PDE** (also know as Photon Detection Probability) expresses the detection efficiency as the percentage of incoming photons that are detected by the device. An ideal detector should detect all the incoming photons and should have a **PDE** equal to 100%. The real **PDE** of a detector depends on the wavelength λ and on the angle of incidence of the photon and it is then experimentally measured using a collimated monochromatic light source [27].
- **Dark-Count Rate (DCR)**: The **DCR** is the rate of detector output pulses measured in the absence of any incoming photons. The **DCR**

pulse is not distinguishable from a pulse generated by a single photon and it is the equivalent of noise in single photon measurements, i.e. if the detector is used as a photon counter the ratio of detected single photon events and **DCR** can be assumed as the Signal-to-Noise ratio.

- *Time jitter (δt):* It is the variation from event to event in the delay time between the input of the optical signal and the output of the electrical signal. Time jitter can be practically expressed as the resolution of the measure of the arriving times of periodic light pulses with narrow time amplitudes, such as produced by Titanium Sapphire *fs* lasers. The resolution is commonly expressed as the **Full Width Half-Maximum (FWHM)** of the frequency histogram of the arriving times of the pulses.
- *Dead time:* The detection of a photon disables the single-photon detection ability for a certain amount of time. This time is a characteristic of both the detector and the front-end electronic circuit.
- *Photon-number resolution:* It is the ability to distinguish the number of photons in an incident light pulse.

As suggested in [1], a score can be assigned to a detector in order to express its overall performance using a formula that reassembles the three first quantities previously listed:

$$\frac{PDE}{\delta t \cdot DCR} \quad (1.1)$$

Nowadays the single-photon sensor market is populated by a few number of devices:

- **PMT:** The photoelectric effect is exploited to generate, as a consequence of the absorption of a photon in a charged cathode, an electron

that is accelerated to an anode in vacuum. This electron hits the anode with enough kinetic energy to cause a cascade of emitted electrons that in turns are accelerated towards anode at lower potential, producing a multiplication effect that proceed by geometrical progression. The multiplication process in the chain of anodes is the best low noise gain procedure available [28], being only affected by statistical variation in the number of produced electrons (shot noise). The device consists of a glass vacuum tube that contains the cathode and the chain of opportunely shaped anodes, or dynodes. The voltage difference between the cathode, namely the bias voltage, and the last anode is typically several thousands of Volts. The **PDE** is affected by reflection in the entry windows, partial absorption of photons in the cathode and self quenching of the produced electron in the bulk of the cathode . A **PDE** in the range from 10% to 30% is normally expected [1] and strong research effort has been spent since the first device to reduce reflections at the entry glass window, to optimize the cathode material as a function of incoming photons wavelength, and in shaping the anodes to optimize electron multiplication. The **DCR** is caused by thermo-ionic effects and increases as temperature increases and as bias voltage increases. It's possible to discriminate the number of incoming photons through an analysis of the output pulses with the aid of dedicated front-end (see as example the time-over-threshold Asic described in [29]). Main drawbacks are related to the bulk and fragile vacuum technology. Moreover **PMTs** do not provide information on the position of the incoming photons and are sensitive to magnetic fields.

- **Multi Channel Plate PMT (MCP-PMT)**: In **MCP-PMT** a 2D array of **PMT** micro-dynodes are dug in a stack of plates obtaining a 2D array of micro-channels. The detector is position sensitive, has an

improved time resolution with respect to **PMT**, and is little affected by strong magnetic fields [30].

- **Gated Image Intensifier Unit (GII) coupled to Charge-Coupled Device (CCD)**: This is a single-photon imager that is assembled positioning a low noise **CCD** camera at the output of an image intensifier. The image intensifier converts photon to electron at the photocatode, accelerates and multiplies electrons, and then back-convert electrons to photons using phosphorous screens. The gain can reach 10^6 with **PDE** comparable to the ones of **PMT** [31] but, due to the decay time of their phosphorous screen (hundred of ns in the best case), **GII** can be used in **TCSPC** applications only if the photocatode is polarized in time-gated windows. Indeed the main application of this detector is time resolved imaging in biology and medicine [32]. The minimum time interval of the polarizing gate window, found in commercial **GII** [31], is $250ps$, with a maximum repetition rate in the order of $10kHz$. The image has low spatial resolution having pixel of $0.020 - 0.040 mm^2$ [33].
- **Single Photon Avalanche Diode (SPAD)** All the previous detector are based on the vacuum technology of **PMT** and are thus prone to similar disadvantages. In particular previous instruments: (i) are quite big and delicate as they get damaged if exposed to the environment light (ii) are sensitive to magnetic fields (iii) are expensive and mostly handmade. These reasons forced the search for an alternative to **PMT** Detection of single photons by means of silicon $p-n$ junction was first achieved in 1960s, during the study on the physics of avalanche in semiconductors [34, 35]. When a $p-n$ junction photo-diode is reversed biased with a voltage V_{bias} , an electric field exists in the vicinity of the junction that keeps electrons confined to the n side and holes con-

fined to the p side of the junction, delimiting a charge-free zone that is known as space-charge region. When an incident photon of energy higher than the energy band-gap (1.14 eV) is absorbed in silicon, an electron-hole pair is generated. Pairs generated in the space-charge region of a p - n junction are separated by the electric field. If the field in the space-charge region is high enough, i.e. V_{bias} greater than the breakdown voltage (V_{break}), an electron-hole pair may be accelerated strongly enough to create a new pair in a collision with the lattice. An avalanche of generated carriers may be thereafter generated and at the external leads of the device we observe an exponentially growing current. The current increases until it is quenched by an external circuit (commonly called ballast or quenching circuit), otherwise it would reach destructive level [36]. If, for example, there is a series resistance, more and more voltage is dropped across that resistance as the current grows. This effect reduces the voltage drop across the high-field region, and when the voltage approaches V_{break} the avalanche stops. The quenching resistor R_q acts also as a decoupling element between the **SPAD** and the rest of the circuit because, with the diode capacitance C_{spad} , it constitutes a filter with a time constant $\tau_q = R_q \cdot C_{spad}$ much larger than the time of a discharge. The total number of electron-hole pairs produced is fixed by the external circuit, not by the number of original incident photons. In the simple resistor-quenching case, for example, the avalanche has no further opportunity to die out until the diode has discharged from its initial bias down to the breakdown voltage. The single photo-diode is operating in Geiger mode (high gain, digital behavior; fired, not-fired) and thus is called **Geiger Avalanche Photodiode** (**G-APD**) or **SPAD**. The main technological issue in **SPAD** realization is the control of the potential drop in the electric field at the boundary of the p - n junction. The projection of this zone on

Detector type	Operation temperature [K]	Detection efficiency, wavelength (PDE[%] @ λ [nm])	Timing jitter δt [ns] (FWHM)	Dark-count rate (ungated) 1/s
PMT (visible-near infrared)	300	40@500	0.3	100
PMT (infrared)	200	2@1550	0.3	200000
MCP-PMT	270	30@1064	0.2	30000

Table 1.1: Examples of commercial available single-photon detectors

the surface of the diode is called the active area of the **SPAD**. If the potential drop is not homogeneous through the boundary it would reach V_{break} earlier in small zones and an abrupt p - n junction would results in a very small active area. An homogeneous potential drop is obtained using proper doped regions (guard-rings) that have been realized both in dedicated silicon technologies and in some standard *Complementary Metal Oxides Semiconductor* (**CMOS**) technologies [37]. One of the figures of merit of a **SPAD** is the ratio between the active area and the total area of the device, namely its *Fill Factor* (**FF**), that is commonly expressed in percent. Several types of **SPADs** are available in the market.

Other Single-photon detectors, less commonly used due to their fragile structures, are *Hybrid Photo-Detectors* (**HPD**) [38]. The design of a prototype of *Multi Channel Plate Hybrid Photo-Detector* (**MCP-HPD**) is reported in [39]. In table 1.1 data extracted from data sheets of commercial available single photon sensor have been reported³.

In the following subsections the two types of single-photon sensors that have been used during this thesis are described.

³Devices available until April 2012. Equipment, instruments and materials are identified in this report to foster understanding.

1.2.1 SiPM

As previously stated the signal of a **G-APD** is not proportional to the initial flux of light. At the end of 90s a matrix of **G-APDs**, realized in a dedicated silicon technology, was connected all in parallel via an individual limiting resistor by Golovin and Sadygov [40, 41] to obtain the first **Silicon Photo-Multiplier (SiPM)**. For small quantities of incident photons the output signal of this device is proportional to the number of fired **G-APDs** in the matrix (N_{fired}); the output is the sum of individual cells signals. The output signal amplitude (A) remains proportional to the number of incident photons ($N_{photons}$) as long as this number is significantly smaller than the total number of **G-APDs** in the matrix (N_{total}). If a “successful interaction” is defined as an interaction between a photon and a cell that starts an avalanche, the output signal can be expressed as a function of $N_{photons}$ using Poisson statistic. Poisson statistic is commonly used when there are a large number of small probable events. The probability P that $N_{photons}$ give $n_{succ.}$ successful interaction is expressed as:

$$P(N_{photons}, n_{succ.}) = \frac{\frac{N_{photons}}{N_{total}}^{n_{succ.}} \cdot e^{-\frac{N_{photons}}{N_{total}}}}{n_{succ.}!} \quad (1.2)$$

N_{fired} can be calculated from the probability $P(N_{photons}, 0)$ that $N_{photons}$ do not give any successful interaction ($n_{succ.} = 0$ in previous equation). In fact $(1 - P(N_{photons}, 0))$ is the probability that a photon gives a successful interaction with at least one cell. This number times the cell number in the matrix gives the number of fired cells and the signal area (A) can be expressed as a function of $N_{photons}$ using the **PDE** as :

$$A = \sum_i A_i \propto N_{fired} = N_{total} \left(1 - e^{-\frac{N_{photons} \cdot PDE}{N_{total}}} \right) \quad (1.3)$$

where A_i is the individual cell signal area. It can be noticed that, for a number of impinging photons small with respect to the number of the **SiPM** cells, the area of the signal can be assumed as linearly dependent on the incoming flux of photons. **SiPMs** have an intrinsic statistical behavior and the characteristics of these devices are typically extracted from the study of distribution of large signal pulse collections. The distribution of signal pulse amplitudes is spread mainly by three phenomena: thermally generated carriers, after-pulse and optical-crosstalk.

Thermally generated carriers are carriers that are generated by thermal energy and not by photo absorption. These carriers generate avalanches when the device is not exposed to light; the number of these avalanches is the **DCR** of the device (thermal noise). The study of the **DCR** pulse allows complete characterizations of the devices since the signal triggered by absorbed photons and by thermally generated carriers are identical.

Sometimes during an avalanche some carriers are trapped by lattice defects. These carriers can generate avalanches after the main pulse during a period of several μs after the main breakdown. The resulting pulses are called after-pulses.

As photo absorption also photo generation is possible in silicon lattice, with a low probability. This phenomenon, called optical cross-talk, is due to the annihilation of an electron-hole pair. In an avalanche breakdown there are in average 3 photons emitted per 10^5 carriers with photon energy higher enough to generate, if absorbed, a new electron-hole pair. When these photons travel to a neighboring cell they can trigger an avalanche breakdown there.

At the beginning of 2005, in a collaborative framework between the *Italian National Institute of Nuclear Physics* (**INFN**) and the *Center for Scientific and Technological Research of Trento* (ITC-irst) (presently *Fondazione Bruno Kessler* (**FBK**)), a project aimed at the development

and application of **SiPMs** was launched. The role of **FBK** laboratories has been the technological development of the dedicated silicon process and the electrical characterization of the device. A small but significant number of publications can be found in literature that document this activity [42, 43, 44]. Nowadays **SiPMs** are expected to witness higher uptake due to their ability to reduce the cost of clinical systems such as **PET** and are candidate to substitute **PMTs** in a large number of Photon-starved applications. The **SiPM** devices that have been used in this thesis are one of the results achieved in the last years by the **FBK** laboratories, in particular by the *Silicon Radiation Sensors* (**SRS**) group.

1.2.2 CMOS SPAD arrays

The realization of **SPADs** in a standard **CMOS** technology permits the integration of the detector, the front-end electronic and the first data processing logic on the same die. Moreover this technology offers a high production yield allowing, in principle, a high cost reduction from the prototype to products. The first implementation of a **SPAD** in standard $0.8\ \mu\text{m}$ *High Voltage* (**HV**) **CMOS** technology dates back to 2003 [45]. The same authors documented also the first 2D array of **HV-CMOS SPAD** [46]. The **HV CMOS** technology was needed to realize the guard-ring, that was implemented with a *p*-tub implant. In the following years several structures have been proposed using $0.35\ \mu\text{m}$ **HV CMOS** technologies [47] as well as advanced 180 [48] and 130 *nm* **CMOS** technologies [49, 50, 51, 52]. At the same time the **CMOS** logic processing the **SPAD** output has been tuned to solve specific tasks, to the extent that nowadays the wide horizon of **CMOS SPAD** applications can be divided in categories. In particular a division can be made between imaging and non imaging application because this greatly influence the **FF**. Indeed the integration of processing logic at the sensor level has many advantages, as example it permits to minimize par-

asitics and stray capacitance and to reduce the complexity of the external measurement systems, but it has as drawback the amount of space needed on the surface of the sensor for its implementation. The required area grows with the complexity of the functions that have to be accomplished by the implemented logic to do the measurement. For a given function the problem becomes worse in imaging detectors with respect to non imaging detectors. This is because in imagers the function has to be accomplished at pixel level to acquire an image of the requested feature. Consider as example the 32×32 TCSPC imager developed in the last 5 years during the Megaframe⁴ European project [53, 54, 55]. The authors of these imagers, all realized in 130 nm CMOS, conceived different strategies to implement the TCSPC function at pixel level, achieving FF < 1%. On the contrary, in non imaging application, the positioning of the electronic and the sensitive area are customizable. Moreover, the greater design freedom, permits the customization of the SPAD structure in order to maximize the FF. As example the detector presented in [56] is a linear detector developed for Spectral Lifetime Microscopy. Light should be focused by the optics of the microscopy over the linear array of pixels. The active area is a rectangle of $100 \times 1600 \mu m^2$ and the processing electronic is realized at its periphery. Pixels are composed by 4 SPADs, binned together and realized in the same deep N-well implant. Thanks to the sharing of the deep N-well implant, the area losses between the neighboring SPADs has been reduced and a FF of 34% has been reached. Besides having the drawbacks described for SiPMs (DCR, after-pulsing, optical cross-talk), SPAD arrays realized in CMOS technology suffer also a higher defectiveness that can affect a rele-

⁴MEGAFRAME Mega Frame per second, Time correlated Single Photon Camera. European project that aimed to “to bring single photon imaging technology to an advanced low-cost deep-submicron CMOS platform, so that massive arrays of single photon detectors can coexist with and interface to large networks of parallel digital processing units on the same chip. The target fields are biology, physics, and medical imaging. However, any disciplines requiring time-resolved ultra-fast optical sensors are prime candidates.” www.megaframe.eu

vant percentage (10-20 %) of its **SPADs**. The **SPADs** that are affected by fabrication defect present a higher **DCR**. The influence of this defectiveness can be mitigated conceiving the **CMOS** read-out in order to disable the **SPADs** that present high **DCR**. The first part of this thesis is dedicated to the characterization of a **CMOS SPAD** array designed by the *Smart Optical Sensors and Interfaces* (**SOI**) group of **FBK**. The sensor has been realized in 0.35 μm **HV** technology provided by *Austria Micro System* (**AMS**), exploiting the same structure of the sensor presented in [56] and will be detailed in the following chapter. The characterization has been performed in the framework of a project funded by Provincia Autonoma di Trento, the *NAno On MIcro* (**NAOMI**) collaboration⁵. Therefore the sensor is referred in the following as *NAOMI-Pixel Device* (**NPD**).

1.3 Fluorescence lifetime Spectroscopy

The measurement of the decay time of fluorescent molecules, namely fluorescence lifetime spectroscopy, is a powerful tool that is becoming increasingly popular in biology research laboratories [32]. The lifetime conventionally is the decay time of the exponential that fits the curve of the light fluorescent emission along time. Lifetime spectroscopy is performed exciting fluorescent molecules with a large number of ultrashort (tens of *ps*) laser pulses and measuring the lifetime of the fluorescent emission. A *ps*-second laser pulse is needed because the decay time of studied molecules is in the order of a few nanoseconds. A large number of laser pulses is needed because the number of photons that reach the detector is typically low due to both the low number of fluorescent molecules in the sample and to the high optical losses of the system. Lifetime spectroscopy applications

⁵**NAOMI** aims to “the development of analytical tools for proteomic, to both discriminate among protein families and to give information on the conformational state of the proteins.” <http://naomi.science.unitn.it>

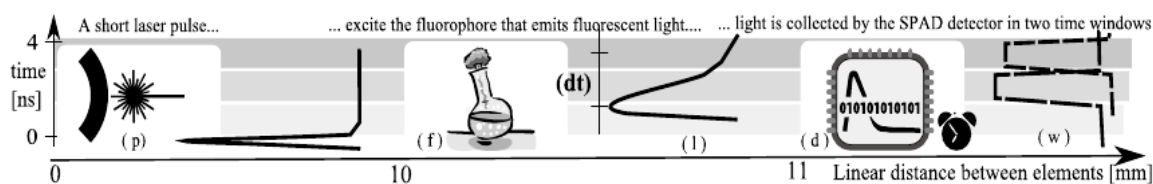


Figure 1.1: A ps Laser diode (p) is used to excite the fluorophore (f). The fluorescent emission (l) is collected by the detector (d) through two different sampling time windows (w) to calculate the light emission decay time (dt), namely the Lifetime, of the fluorophore (f).

can be divided in imaging and non imaging. An example of imaging application is the fluorescence lifetime imaging microscopy while an example of non imaging application is the read out of fluorescent micro-array assay of spotted probes. Focusing on the last one, recently have been reported in literature imagers that have been fitted for the application [57, 58, 59, 60, 61], as well as custom non-imaging sensors that have been developed to best fit the request of portable lab-on-chip instruments [14]. In the case of custom non-imaging sensor the sensitive area can be properly shaped and laid out where it is needed. In particular, in the case of micro-array assays produced in biological labs, the spotted probes have a dimension that is typically few hundreds of μm , with a pitch having similar dimensions. Therefore the sensitive area can be designed to suit the dimension of the spotted probes while the processing electronics can be placed in the space between the probes. Thanks to the available space the processing electronic in the read-out channel can be conceived to minimize the data-throughput of the application. This can be done exploiting the time-gated technique, described in [62], that is sketched in figure 1.1. In this sketch a **SPAD CMOS** detector (d) collects the fluorescent light emission (l) that is subsequent to a large number of laser-pulses (p). The collection is done in two subsequent time-windows (w) that integrates two portions of the exponential decay. For mono-exponential fluorescence intensity decays the

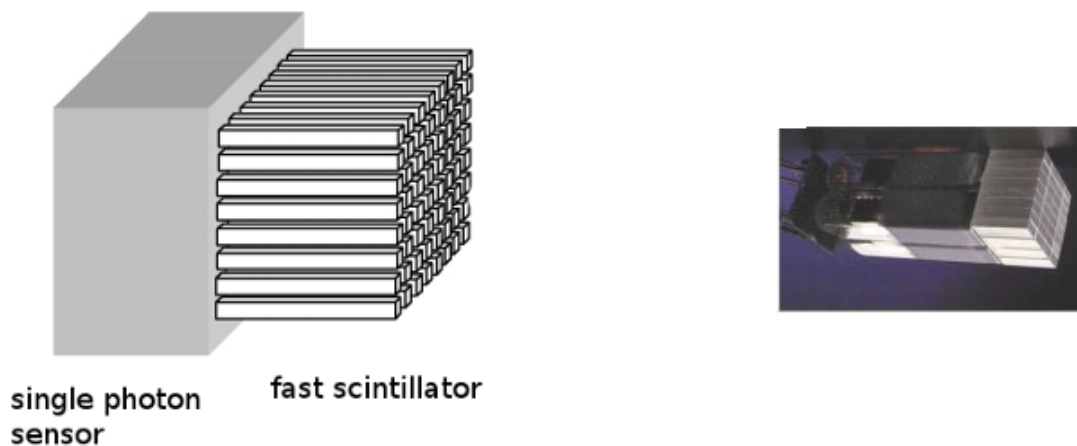


Figure 1.2: PET detector

lifetime τ is given by [62]:

$$\tau = \frac{\delta T}{\ln \frac{I_2}{I_1}} \quad (1.4)$$

where δT is the time-offset between the start of the two time-windows and I_1 and I_2 are the corresponding integrated fluorescence intensities. The method well suits the logic features that can be realized in CMOS logic while the calculation can be implemented in *Field-Programmable Gate Array* (FPGA) [63]. The NPD detector described in the first part of this thesis has been conceived to fit the needs of a lab-on-chip application, as will be shown in chapter 2.

1.4 Positron Emission Tomography detectors

In the framework of *Single Photon Avalanche Diode network* (SPADnet)⁶ collaboration the NPD has been used to evaluate the feasibility of the realization of a CMOS digital SiPM using a standard HV CMOS technology. This evaluation is reported in chapter 4. First digital SiPM has been demonstrated in 2009 [64] using a customized CMOS technology. Achieving the know-how that is needed to develop this detector in a standard CMOS technology have the potential to resolve the data-throughput problem in large system applications at an unprecedented low cost. The target application is PET detectors, that has been driven the development of SiPM during the last years [65]. As sketched in figure 1.2, a PET detector is built using a γ -ray fast scintillator coupled to a single-photon sensor. The scintillator can be, as an example, an *Ortho Silicate of Lutetium* (LYSO) crystal that converts the energy of a γ -ray to several thousands of blue photons [66]. Research projects have been recently conducted to push the technology of PET detectors to achieve low-cost PET scanners⁷. As an example the two projects Ax-PET⁸ [67] and COMPET⁹ [68] are exploring

⁶SPADnet is an European funded research program that “*aims to develop a new generation of smart, large area networked image sensors, based on a conventional CMOS fabrication technology (the same as used for microchips or sensors in cellphone cameras, for example), for photon-starved biomedical applications*” <http://www.spadnet.eu>

⁷see, as an example, <http://medicalphysicsweb.org/cws/article/research/48970> report of the presentation: “*The technology of solid state detectors in Nuclear Medicine*” held by Sibylle Ziegler at ICTR-PHE 2012

⁸CERN project: “*AX-PET is a novel PET detector based on long axially arranged crystals and orthogonal Wavelength shifter (WLS) strips, both individually readout by Geiger-mode Avalanche Photo Diodes (G-APD). Its design was conceived to reduce the parallax error and simultaneously improve spatial resolution and sensitivity. A ‘Demonstrator’ has been built which consists of 2 detector modules (in total 96 LYSO crystals and 312 WLS strips)*” <https://twiki.cern.ch/twiki/bin/view/AXIALPET/WebHome>

⁹University of Oslo project: “*COMPET is a MRI compatible preclinical PET scanner aiming towards a high sensitivity and a high point source resolution (PSR) by implementing a novel block detector geometry. Layers of matrices consisting of long LYSO crystals and wavelength shifter (WLS) fibers are used to determine the point of interaction (POI) of the γ -ray within the LYSO crystal.*” . <http://www.mn.uio.no/fysikk/english/research/projects/compet>

new geometries of PET detectors playing with long LYSO, *Wave Length Shifter* (WLS), SiPMs and digital SiPMs [69].

1.5 Time of Flight of positronium

As previously stated the Ps exists in two flavors: spin parallel *p*-Ps, annihilating into two γ -rays with a mean lifetime of 125 ps in vacuum, and spin anti-parallel *o*-Ps, annihilating into three γ -rays with a mean lifetime of 142 ns in vacuum [70]. In the framework of *Antihydrogen Experiment: gravity, Interferometry, Spectroscopy* (AEgIS) collaboration, the group *Hydrogen, Energy, Environment* (IDEA) of University of Trento is drawing experiences that aims to the production of cooled (slow) atoms of *o*-Ps. The sought slow *o*-Ps should be deserved for the planned production of anti-hydrogen, obtained by charge-exchange process between *o*-Ps atoms and antiprotons [71, 72]. The production of cooled *o*-Ps has been obtained with the experiment sketched in figure 1.3 [73, 74], that has been conceived also to study the temperature, velocity, of the cooled Ps. Referring to figure 1.3, a bounce of e^+ is linearly accelerated towards a cooled porous sample of Silicon. Hitting the surface of the sample, the bounce of e^+ produced a cloud of scattered e^- (1), that is revealed by a ChannelTron. The signal of the ChannelTron fixes the start-time of the experiment. The bounce of e^+ enters in the Silicon lattice, at a depth that depends from the implantation energy (some keV with the accelerator of the University of Trento), forming atoms of Ps with e^- . Preferential sites for Ps formation are defects in the lattice, vacancies, dislocations as well as pores boundaries. 25% of Ps is formed as *p*-Ps, that completely annihilates in few hundreds of ps, while the remaining 75% is formed as *o*-Ps. A part of the *o*-Ps that is formed into open pores may escape (2) from the sample and may be re-emitted in the vacuum with a velocity (or temperature) that results from

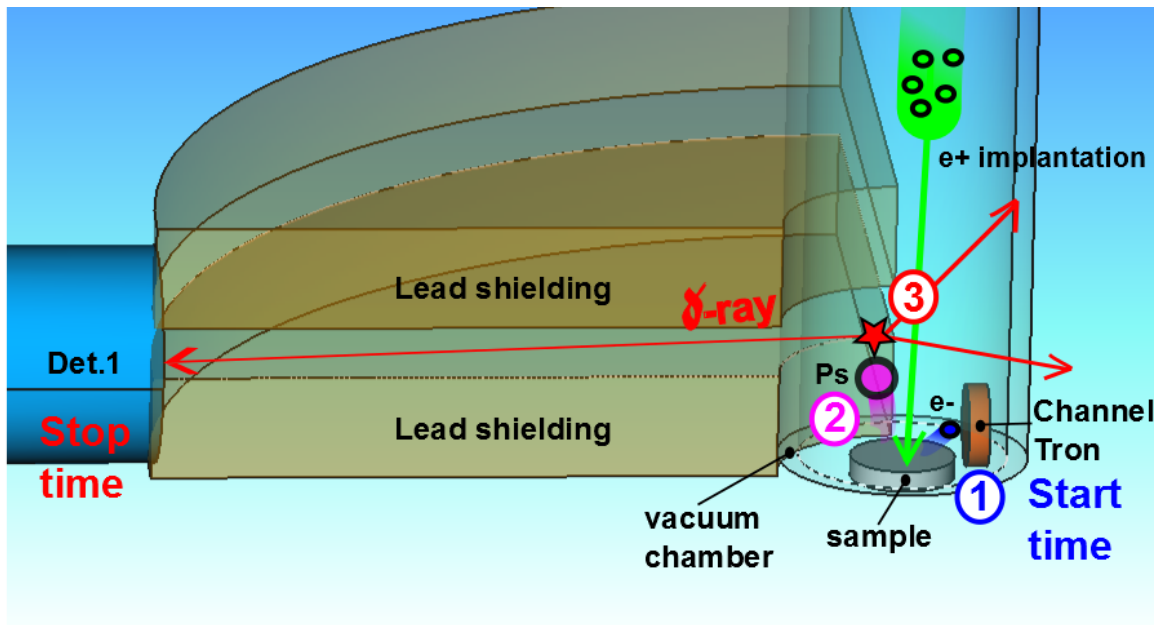


Figure 1.3: A bounce of e^+ is linear accelerated towards a cooled porous sample of Silicon. Hitting the surface of the sample, the bounce of e^+ produced a cloud of scattered e^- (1), that is revealed by a ChannelTron. The signal of the ChannelTron fixes the start-time of the experiment. A part of the o -Ps that is formed into open pores may escape from the sample (2) and may be re-emitted in the vacuum with a velocity (or temperature) that results from the interactions with the walls of the pores during its travel towards the sample surface. The emitted o -Ps travels in the vacuum until annihilation, with the following emission of three γ -rays (3).

the interactions with the walls of the pores during its travel towards the sample surface. The emitted *o*-Ps travels in the vacuum until annihilation, with the following emission of three γ -rays (3). Experimentally it has been found that cooling the sample decreases the velocity of emitted *o*-Ps, that has been measured in various solids [75, 73]. The velocity of *o*-Ps is determined recording the TOF of the *o*-Ps, i.e. the difference between the time of the detection of a γ -ray in a collimated detector and the start-time of the experiment. The detector currently mounted on Trento apparatus are PMTs coupled with *Sodium Iodide activated with Thallium* (NaI:Tl) crystals. The detectors are collimated using two lead shields as illustrated in figure 1.3 and are displaced in a single ring. In the last chapter of this thesis the advantages of the replacement of this detectors with SiPMs are discussed and a multi-ring detector is designed with the aid of Monte-Carlo simulations.

1.6 Thesis content

The order of topics follows the order of the three applications cited in the previous three paragraphs. The thesis is composed by a part dedicated to the characterization of the detectors and a part dedicated to the study of applications by means of Monte-Carlo simulations. The discussion starts with the characterization of the NPD detector developed by SOI FBK group, chapter 2. The characterization examines cited points of weakness of the SPAD detectors: DCR, defectiveness, optical cross-talk. At the same time the points of strength of the detector in the target application, i.e. time-gated fluorescence lifetime spectroscopy in lab-on-chip, are discussed. In chapter 3 simulations are performed to study the deployment of NPD sensors in a lab-on-chip applications, with particular attention to the cross-talk between adjacent sensors. The same NPD detector has been used in

an exploratory experiment to evaluate if its technology (**HV CMOS**) is suitable for the realization of a digital-**SiPM**, chapter 4. The experiment directly compare the performances of the **NPD** with the performances of a **SiPM** provide by **SRS FBK** group, putting the two detectors at the two sides of the same **LYSO** crystal. The effect of this configuration in light propagation is discussed in detail in chapter 5. In this chapter an experiment setup is built using two **SiPMs** coupled to the same **LYSO** crystal. The two crystals used in the two experiments of chapter 4 and of chapter 5 have similar aspect ratio ($1 \times 1 \times 15$ and $3 \times 3 \times 30$, respectively) and are both oriented in the same way with respect to the radioactive source. Examining the aspects of light emission from a scintillator, the discussion comes to a method for the application of measured value of **PDE**, which is determined with collimated light sources, to the diffused light output of scintillator crystals. In the discussion of this method the interaction between **γ -rays** and matter is assumed following a Lambert-Beer law. Chapter 6 is dedicated to the discussion of this assumption and to its refinement. In this chapter the algorithm implemented in the SLitrani Monte-Carlo library to model **γ -ray**-matter interaction is discussed underlining the assumption made at its foundation as well as its range of validity. The SLitrani open-source library is used in chapter 7 to evaluate the application of **SRS SiPM** to the apparatus of **IdEA** group of University of Trento. The new design of the apparatus should use crystals similar in aspect ratio to the ones used in the experiments of 4 and 5 and oriented in the same way with respect to ***o*-Ps** annihilations. The deployment of **γ -rays** detector in this apparatus is discussed with particular attention to the cross-talk between adjacent detector rings and to the poissonian noise.

1.7 Innovative Aspects

The characterization methods described in chapter 2 follow methods of characterization that are applied in literature to similar devices. The innovation resides in the structure of the device developed by the SOI group and, in particular, in its customization performed to fit the needs of lab-on-chip applications. To stress the innovative content of this customization, the simulations in chapter 3 are presented. Chapter 4 can be read as a proof of concept. The discussion is focused to practical aspects of the preliminary work conducted in collaboration with the SOI group that is deeply engaged in the realization of innovative CMOS digital SiPMs. Similarly the experiments presented in chapter 5 can be read as a case history useful to introduce the simulation framework presented in the chapter. The framework stressed the importance of the analysis of the angular light distribution at interfaces and it is innovative in its applications to SiPMs devices developed by SRS group. Chapter 7 is dedicated to the optimization of the apparatus built by IdEA group. The optimization exploits the compactness of the the SiPM-based detectors to reach a new multi-ring design. The novelty resides in the optimization method that has been developed for the specific experiment.

1.8 Materials and Methods

The CMOS SPAD NPD prototype, used in the experimental activity reported in chapters 2 and 4, has been interfaced with the external acquisition system using an FPGA¹⁰. The firmware on the FPGA, and the corresponding software on the PC, has been written using VHDL and C++ libraries¹¹. The signal of SiPMs have been acquired, in the experimental

¹⁰Xilinx Spartan 3, Opalkelly XEM3001

¹¹Opalkelly Frontpanel VHDL and C++ library

activity reported in chapters 5, using Ztec zt4211 digital oscilloscope [76]. Acquisition and processing software have been written using the ROOT framework [77]. Other informations about materials and instrumentation are detailed in the description of the experiments. Similarly, details about the simulations procedures, developed using the Monte-Carlo method [78], are provided in chapters 5 and 7.

Chapter 2

The NPD detector

In this chapter the characterization of the **NPD** detector is reported. Figure 2.1 is the micro-photograph of the detector realized in the $0.35 \mu m$ **AMS HV CMOS** technology. Figure 2.2 is a sketch representing the main components of the detectors. The sensitive area (A in the sketch) has a size of $260 \times 260 \mu m^2$ and consists of an array of 10×10 **SPADs** with a pitch of $26 \mu m$. The array has been divided into four 5×5 sectors, where all the 25 **SPADs** in a block are binned to the same digital read-out channel. The rest of the silicon area is devoted to the read out electronic composed by 4 read-out channels. The total area of the **NPD** detector is $600 \times 900 \mu m^2$. The read-out channels are able to perform the time-gated lifetime measurement, as described in section 1.3 [62]. The **SPADs** have been realized with the structure presented in [47], and share the same deep *n-tub* implant in order to achieve a high fill factor of 48%. Each **SPAD** can be individually enabled or disabled using a 100-bit memory (m in the sketch) that is programmed by the user through an external driver. The photon counts generated by each sectors are gated separately by the gates (g). All the gates in the device are controlled by two timing signals, which can be generated by an on-chip *Phase Locked Loop* (**PLL**) or alternatively by an external device (t). The two timing signals enable in sequence two 10-

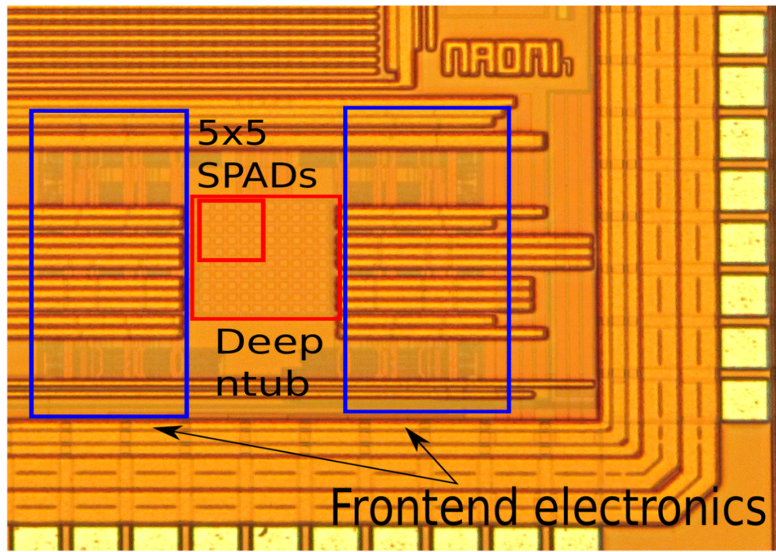


Figure 2.1: Micro photograph of the NPD detector

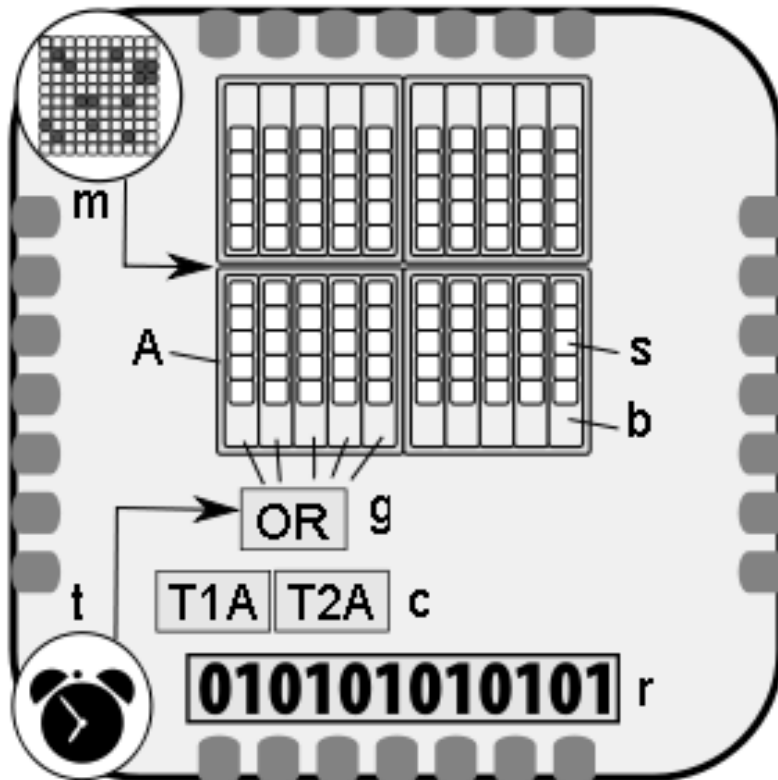


Figure 2.2: Functional description of the NPD detector

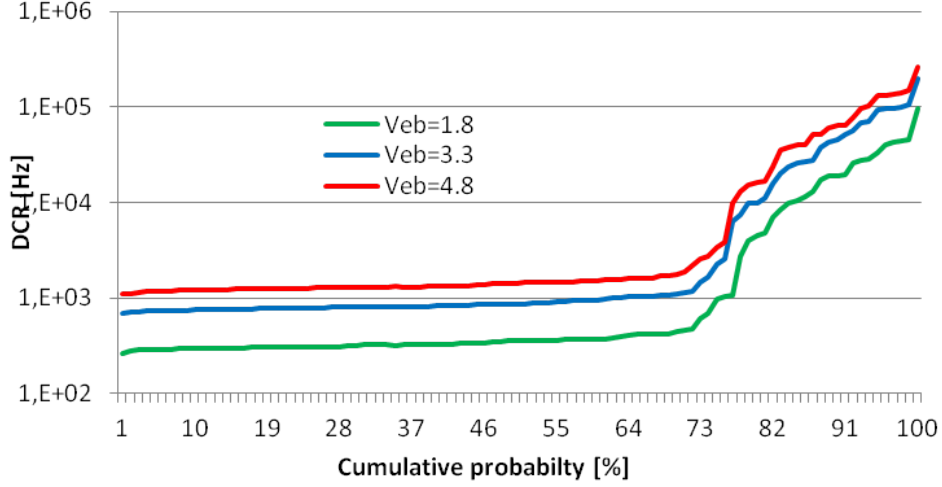


Figure 2.3: **DCR** cumulative distribution of the **NPD** detector at three different excess bias voltage values

bit counters (c) that collect the **SPAD** pulses. The **SPAD** pulses are thus counted during two consecutive gating windows and a single exponential fluorescence decay can be reconstructed using evaluation 1.3. The digital contents of all the eight counters, two for each sector, are transferred to a shift register (r) for data transmission. Only the two values expressing the total number of photons detected for each time window are communicated to the external acquisition system, and therefore the decay curve of the fluorescent light emission can be calculated with a low data throughput.

2.1 DCR

Keeping the device in the dark and at ambient temperature the memory (m) was used to enable one single **SPAD** at a time and to register the associated dark count rate. The measurement was repeated at different excess bias voltage values in order to obtain the bias-dependent distribution of the dark count rate as shown in figure 2.3. In figure 2.4 the dependence of **DCR** from the excess bias voltage can be observed for different **SPADs**.

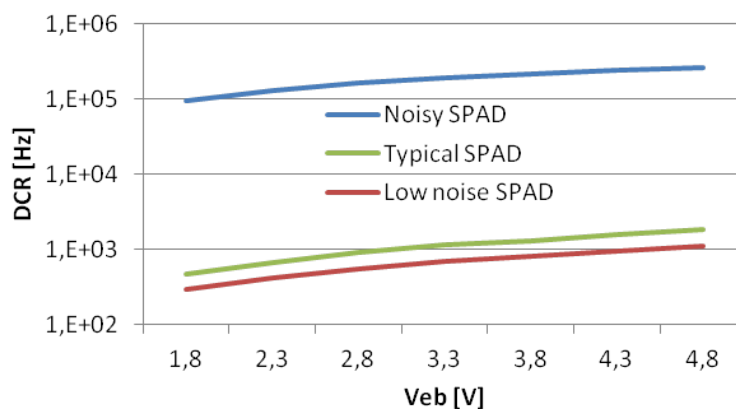


Figure 2.4: **DCR** dependence of the **NPD** detector from excess bias voltage

The **DCR** of three different **SPADs** is graphed from the noisiest to the less noisy one. More than 70 % of single **SPADs** have a **DCR** lower than 1 *kHz* at the lowest excess bias voltage and do not exceed 2 *kHz* at the highest one, whereas about 20% of **SPADs** (the exact number depends on the applied excess bias voltage) show **DCRs** higher than 10 *kHz* . This happens due to random distributed defects within the **SPAD** active area. Total dark count rate over the **SPAD** array can be kept below 100 *kHz* by switching-off noisy **SPADs** (up to 30% of the 10×10 **SPAD** array).

2.2 Optical Cross-Talk

As stated in section 1.2.1, a potential drawback affecting **SPAD** arrays is optical crosstalk: when a device detects a photon, secondary photons are emitted by the **SPAD** itself, due to hot carrier relaxation. These photons can be detected by adjacent detectors [79, 80], and this phenomenon increases in importance at increasing **FF**. The division of the device in sectors permits the observation of the optical cross talk between neighboring **SPADs**. A value between 2 % and 3 % was measured for lateral neighbors, whereas for diagonal neighbors the value decreases to 0.3 % - 0.5% because

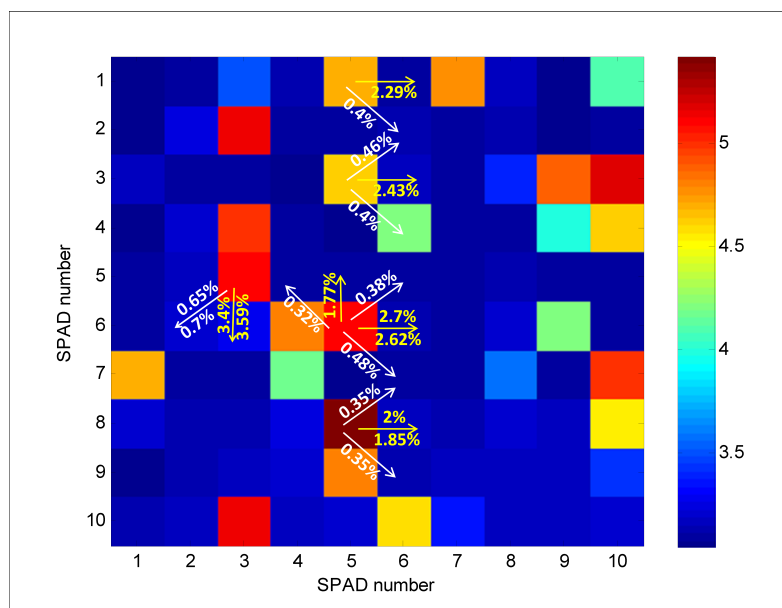


Figure 2.5: Measurement of the cross-talk in the **NPD** detector. Order of magnitude of the **DCR**, expressed in Hz , is reported on the colormap

of larger distance. The measure is reported in figure 2.5, on the top of the map of the device **DCR**.

2.3 Dynamic Range

The overwhelming interest in **SPADs** is their ability to detect extremely weak signals. However the highest detectable power is also very important and therefore the ratio between the maximum and the minimum detectable power, namely the dynamic range, is also a significant figure of merit. A characterization of sensor dynamic range was performed using a wide spectrum stabilized halogen lamp and a set of neutral density filters. With this setup, optical light intensities spanning more than four orders of magnitude could be generated. The noisiest **SPADs** of the array were disabled, so that 81 of the 100 **SPADs** were active during the measurement, and the total **DCR** was lower than 100 $kcps$. A graph showing the number of counts in

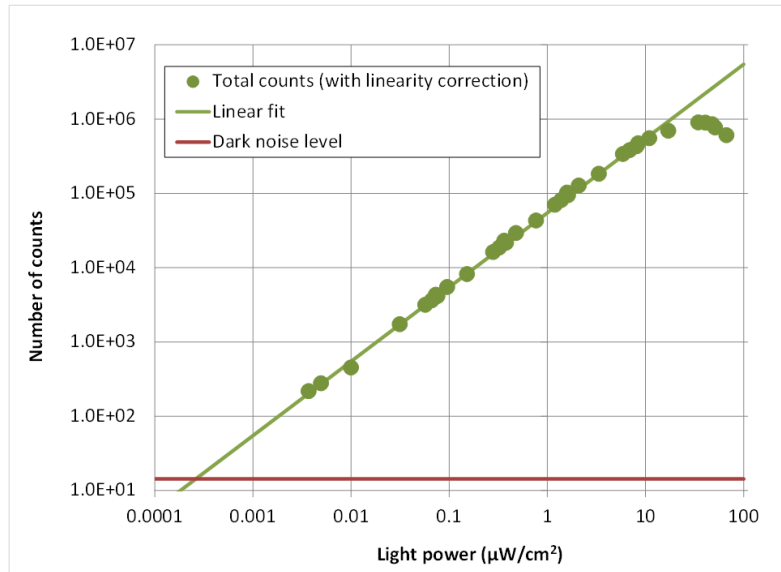


Figure 2.6: NPD detector dynamic range

the array as a function of incident optical power density is shown in figure 2.6. A total exposure time of 2 ms was used in the measurement, and the count rate was corrected for the total dead time and for the DCR. The sensor dynamic range, limited at the low end by the DCR noise and on the high end by sensor saturation, is about 5 orders of magnitude. The count rate reduction at very high light intensities is due to the bandwidth limitations due to dead time. It is worth noting that the maximum count rate of the sensor before saturation is 500 MHz. A dynamic range exceeding 120 dB is observed with 1 s integration time

2.4 Time Gating

A picosecond pulsed laser diode¹ has been used to characterize the gating performance of the sensor. The attenuated laser beam hits a diffuser placed in front of the sensor, while two time gates with variable time delays from

¹Picoquant, $\lambda = 470\text{nm}$, pulse width FWHM = 70ps

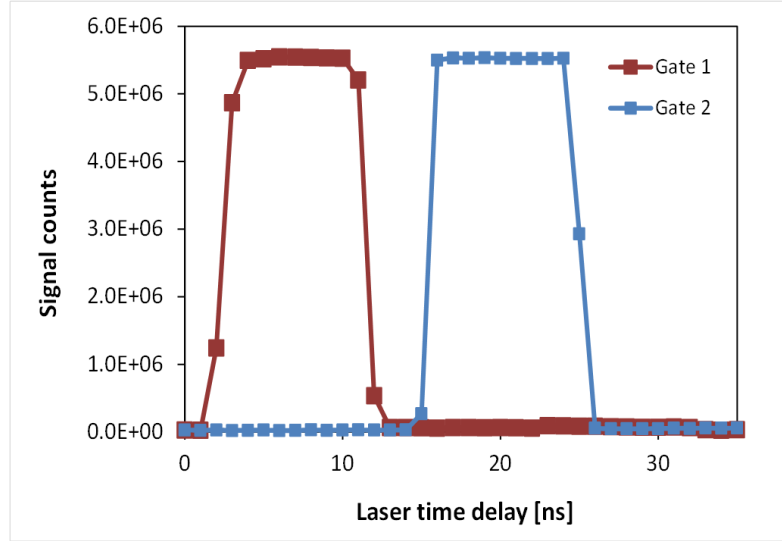


Figure 2.7: NPD time resolution

the laser trigger were generated by using a two-output pulse generator². The output of two gated counters as a function of time delay is shown in figure 2.7, with the two gates width set to 9 ns . A sub-ns time resolution can be observed in the rising edges of this measurement.

2.5 Device Data Throughput

To perform the previously presented measurement regarding the dynamic range, the system data throughput has to be fast enough to manage the count rate due to all the SPADs triggering at their maximum toggling speed. Taking into account the dead time of 200 ns , the number of SPADs binned in a sector (25 SPADs), the capacity of the counters (1023 counts) and the shift register width (80 bit), the expected data throughput is 1.2 MBps . However this condition is quite far from a real experimental situation. Taking into account a laser frequency of 40 MHz , the maximum photon counting rate to avoid *pile-up* artifacts should be around 2

²HP 8110A

MHz [81]. This condition can be considered as a *worst case scenario* corresponding to the case where the total number of fluorescence light photons collected is 5% of the total number of laser pulses, a condition that is difficult to reach in a typical experimental setup. The expected sensor read-out rate in this condition is approximately 2 kHz . In this case the driver should read the shift register every $500\ \mu s$ and the total required bit rate is 160 kbps .

2.6 Acquisition system

The low data throughput of the **NPD** detector permits a great simplification of the measurement system. An **FPGA** development board³ was chosen as data buffer between the **NPD** detector and a PC. Data are transferred from the **FPGA** driver to PC using the USB connection. Using USB communication libraries⁴, the maximum transfer rate reported is 38 MBps . Therefore the driver can be used to control a large number of detectors in a future configuration. The feasibility of feeding the time phases to the **SPAD** matrix using the internal clock resources of the **FPGA** was also tested. The chosen **FPGA** provides advanced clocking capabilities using four dedicated devices called *Digital Clock Manager* (**DCM**)s. Due to innards of this **FPGA** device an offset between an imposed delay value and the one produced by the **FPGA** was expected⁵. The characterization of this offset has been reported in figure 2.8. The offset is constant at different settings, the behavior is linear, and the measured time errors are

³Opalkelly XEM3001

⁴Opalkelly VHDL and C++ Frontpanel USB libraries

⁵The four **DCM** devices are connectible in groups of two but one has been allocated by the Opalkelly Frontpanel firmware. In order to enable the two time phases of the **NPD** device, three **DCM** were remaining and two was thus allocated to generate the signals. But due to internal limitation of the Spartan 3 device and to the number of requested resources, not all the clock signals could be routed using dedicated clock buffers and this fact has been created the reported offset.

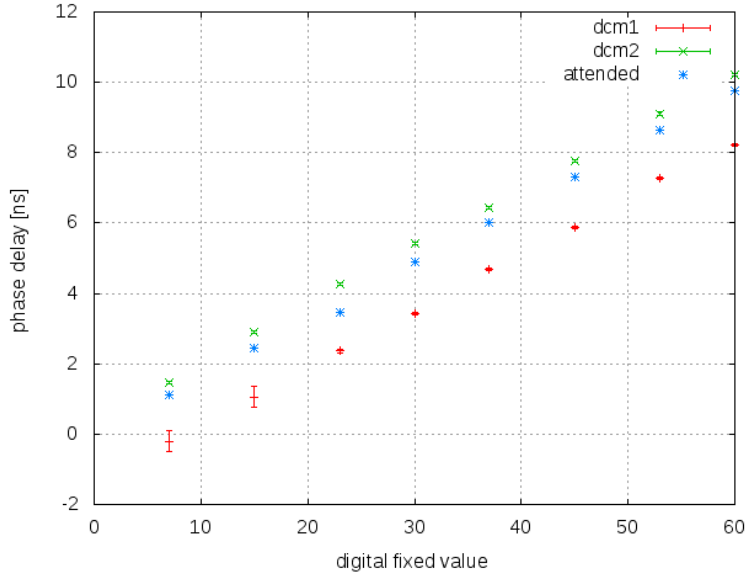


Figure 2.8: Measurement of the offset between two imposed phase delays (DCM1 and DCM2) and the values that were programmed. The measure was obtained using a Tektronix DPO Oscilloscope.

negligible for the considered application. To drive a conclusion, we can state that a simple driver, as the one realized during this experiment, offers enough resources to build a complete measurement system. This is a remarkable result, especially if compared with the complex acquisition systems usually employed in Fluorescence Lifetime apparatus.

2.7 Fluorescent measurements

A set of fluorescence lifetime measurements was performed on ZnS-ZnSe Quantum-Dot reference slides⁶ placed in front of the chip, exploiting the time-filtering capabilities of gated measurements. Fluorescence was excited with the same laser used in the previous experiment. A lifetime non-uniformity lower than 1% was observed among the four 5×5 quadrants with 500 *kHz* fluorescence counts per quadrant in the first window.

⁶Evidot, Evident technology inc.

2.8 Conclusions

The architecture of **NPD** detector is well designed for applications where the constraints of the measurement scenario are single-photon detection capability and on-chip data reduction. In particular, the main points of interest that have been raised from the **NPD** detector characterization can be summarized in the following list:

- A **CMOS SPAD** detector can be designed to fit the needs of a specific application. In particular the **NPD** detector has been customized to fit the needs of lab-on-chip devices. The structure of the sensitive area has been conceived to maximize the **FF**.
- **CMOS SPAD** detectors need low bias voltage and have a low data-throughput. Both these aspects facilitate the integration of **CMOS SPAD** detectors in simple portable instruments.
- **SPADs** have good intrinsic timing resolution (50-200 *ps*). The overall time resolution of the measurement system based on the **NPD** detector is in sub-*ns* range. Measurements performed with a reference sample indicate a good uniformity along the sensor.
- The inherent defectiveness of the **SPAD CMOS** technology can be mitigated disabling **SPADs** with high **DCR**. Optical cross-talk is well below 5%.

Chapter 3

Lab-on-chip design

The **NPD** pixel is designed to fit the dimensions of a fluorescent spotted probe. These fluorescent probes are deployed in 2D array to form a protein assay. Therefore, in order to build a lab-on-chip, several **NPD** pixels have to be positioned on the silicon die and coupled to the 2D assay. Monte-Carlo simulations have been performed in order to investigate how the spatial positioning of the **NPD** influences the measurement performance. The simulations take in account the structure that should be employed to drive the sample over the sensors, namely the fluidic layer. The fluidic layer should be divided in channel using septa. The aim of the simulations is to study the influence in the light diffusion of different septa design. The figure of merit used in the comparison of different geometries is the optical cross-talk, i.e. the mutual optical influence between two pairs of adjacent measurement sites.

The system has been modeled using three different layers (figure 3.1 is an explosive view of our simulated system). The blue colored plane represents the detector. Detector has been conceived as composed by a grid of previously described **NPD** array; this grid should be based on either square or triangular cells. A minimum grid-pitch of $500 \mu m$ should be feasible for a small number of cells distributing some electronic elements along

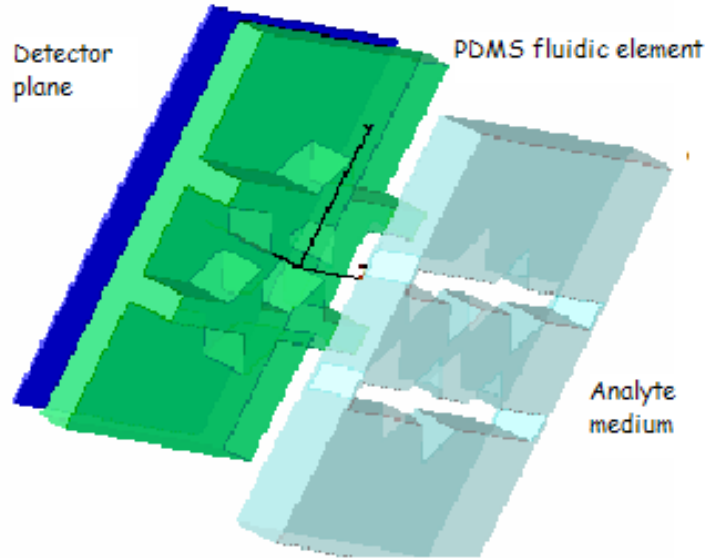


Figure 3.1: Scketch of the setup

detector boundary, while a pitch bigger than the longest side of the actual detector cell ($900 \mu m$) would be unjustified due to the waste of silicon area; therefore grids of **NPD** detectors have been modeled having pitch in the range of $500-900 \mu m$. Each detector is aligned to a fluorescence spot forming a measurement site (micro-reactor). A dimension of $360 \mu m$ in diameter for each spot has been assumed, a size that is well compliant with actual realizable spots dimensions and permits to cover all the area of the corresponding **NPD** detector, which has a diagonal of $367 \mu m$. The green colored element in figure 3.1 represents the *Polydimethylsiloxane* (**PDMS**) layer; it has been conceived as composed by a transparent base, that will give mechanical strength to the structure, and by some chemical-etched septa elements that should accomplish two tasks: septa should split the pumped flux of the sample in different path and should also reduce optical cross-talk among different reactors, if injected with proper light-absorbing inks. In the simulated systems the base of **PDMS** layer has a thickness of $100 \mu m$ and distances $100 \mu m$ from detector plane, allowing wire bond-

ing. It should be feasible to decrease transparency of PDMS injecting dark inks or forming with nano-powders, therefore the walls of septa have been modeled as perfect absorbers. In the design of septa elements some geometrical assumptions have been made taking into account fluidic constraints and practical realizable geometries. The assumption can be summarized as follows:

- A minimum cross section of $50 \times 100 \mu m^2$ for the fluidic channels
- A minimum width of septa elements of $100 \mu m$
- A maximum height of septa elements of $200 \mu m$

Following these constraints the septa height has been simulated choosing values in a range from 50 to $200 \mu m$. Three different geometries have been simulated. In each geometry the sample is assumed to flow through channels built using septa. In particular :

- The first (A in figure 3.2) is based on a triangular grid. Septa are obtained using elements with rectangular and triangular bases. Rectangular elements split analyte fluid and prevent light diffusion between measurement sites of different paths (red and yellow circles in figure 3.2). Triangular based elements are intended to prevent light sharing between two adjacent elements on the same fluid path (red and blue circles in figure 3.2).
- Second geometry (B in figure 3.2) is similar to the previous one but is based on a squared grid.
- The last geometry (C in figure 3.2) is based on a squared grid and split elements are v-shaped.

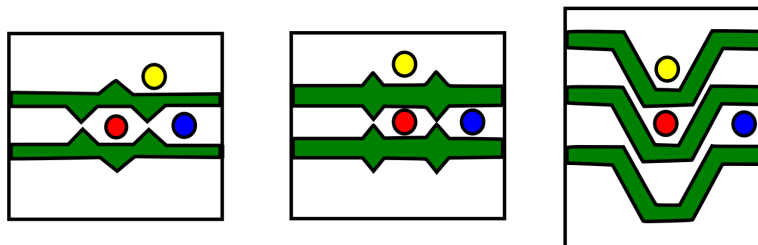


Figure 3.2: Scketch of different geometries assumed on simulation

3.1 Simulation results

Simulations have been performed using a direct¹ ray-tracing Monte Carlo routine. Light generation is represented by a number of rays that are traced from the fluorescence spot to all directions. At the generation point each ray carries the same amount of optical power. During an interaction (e.g. specular reflection, diffusive reflection, transmission, absorption) a ray may generate other rays distributing optical power. Light collected over a defined area is simply the total amount of optical power carried by impinging rays. In simulations the rays take origin from fluorescence spots highlighted as red sites in figure 3.2. Two figures of merit have been introduced to describe light propagation. The two quantities are intended to quantify the light that is collected from a detector that is not directly coupled to the light generating spot, or, in other words, which belongs to a different measurement site. The two quantities, namely light cross-talks, are defined as the ratio between the light collected from a ‘neighbor’ detector and the light collected from the detector directly coupled with the fluorescent spot.

¹The adjective “*direct*” in the noun is commonly use to differentiate this kind of software from Ray-tracer rendering engines, where rays are traced from the camera to a source, while in this simulations are traced from the source to the detector. There are many direct Ray-tracer, both open-source and commercial, that are well-suited for this kind of simulations. I tried [TracePro](http://lambdares.com/software_products/tracepro/) http://lambdares.com/software_products/tracepro/ and [SLitrani](#) [82]

In Figure 3.3 and figure 3.4 light cross-talk in geometry A and B for two different measurement sites (the blue and yellow ones in figure 3.2 A and B, respectively). The two grid geometries are quite similar; in particular we can notice that, as should be expected, triangular elements are less effective in shadowing light than rectangular elements. This is due to the presence of apertures for fluid flow through fluid path. It can be also noticed that the quantity of generated light that pass through apertures, and which is collected by NPD detectors in blue measurement site of figure 3.2, increases by increasing the septa height.

These considerations led us to design the v-shaped geometry, in this geometry apertures for fluid flow are short channels between two septa. In this case light cross sharing values across sites belonging to the same fluid path² are negligible with respect to the two previous geometries. This is due to a larger distance between the reactors, the diagonal of the square grid, and to the presence of channels. In figure 3.5 light sharing for blue and yellow sites of geometry C in figure 3.2 have been reported. As expected, they are quite similar to light sharing for yellow sites of geometry A and B, because septa elements have a similar geometry.

From a practical standpoint, light cross sharing acts as a noise source in the measure, decreasing the signal to noise ratio. The quantity of noise allowed in a measure depends by the minimal signal to noise ratio needed to perform the analysis; for this reason it is not possible to introduce at this point a proper metrics because the overall description of the measure is out of the purpose of this chapter. Indeed other noise sources (as an example the noise that can be generated from the scattering of the excitation light and the poissonian noise of the measure) have to be taken in account to conduct a complete discussion (see as example [83]). To draw a conclusion we can report that v-shaped geometry is a better solution especially for

² calculated but not reported

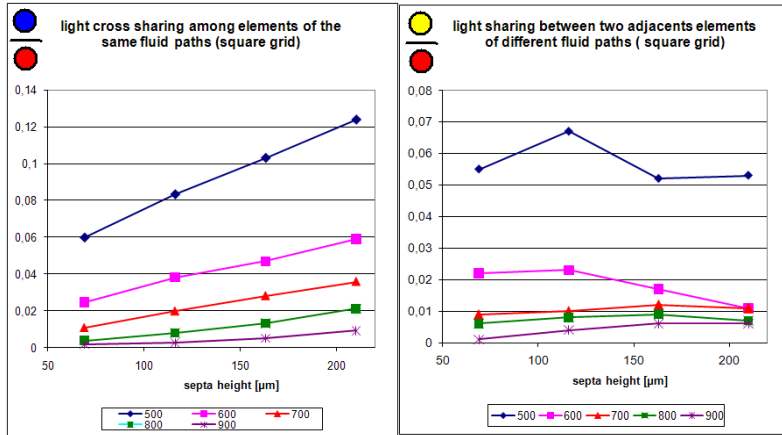


Figure 3.3: Optical cross-talk calculated in 2D array of NPD detectors that are displaced in a square grid

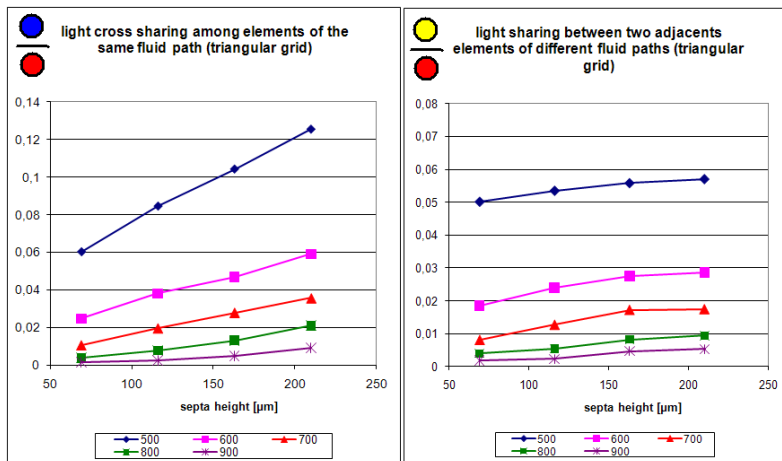


Figure 3.4: Optical cross-talk calculated in 2D array of NPD detectors that are displaced in a triangular grid

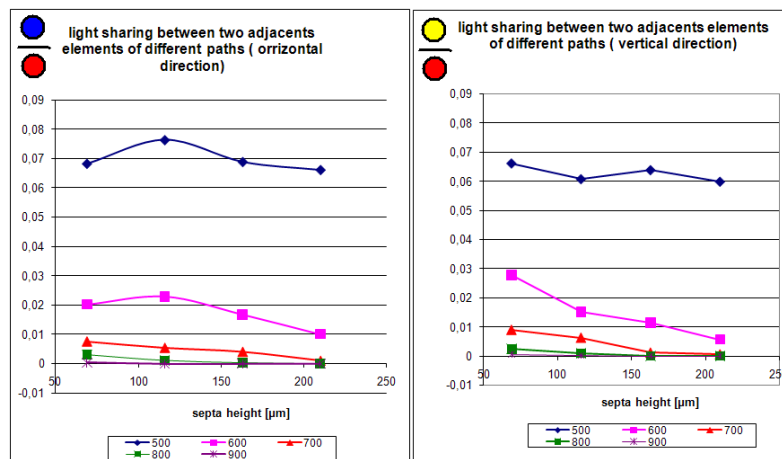


Figure 3.5: Optical cross-talk calculated in 2D array of **NPD** detectors that are displaced in a v-shape configuration.

light cross sharing among measurements sites belonging to the same fluid path.

3.2 Conclusions

A micro-reactor array for fluorescence markers-based bio-affinity assays have been simulated taking into account geometrical and fluidic constraints in view of realizing a lab-on-chip system using a **PDMS** based fluidic. Optical simulations, using a Monte Carlo ray-trace routine, have been performed in order to explore optical properties of different fluidic solution. We have identified some promising geometries and we have discussed their properties.

Chapter 4

CMOS for gamma detection

The **NPD** so far characterized has also been used to evaluate the application of the **HV CMOS** technology to γ -ray detection. The characterization has been performed in the framework of the **SPADnet** collaboration and have been aimed at:

- a very first evaluation of the main practical issues on using a standard **CMOS 0.35 μm HV** technology provided by **AMS** for this application. In particular the first aspect that has been explored is the feasibility of optical coupling with crystals. The optical coupling is obtained with the aid of optical glues and resins, and, the compatibility with this medium and the surface obtained with the **HV AMS 0.35 μm CMOS** process has been tested;
- a verification of the obtained performance with respect to a reference detector. As a reference detector a 1 mm^2 area **SiPM**, produced by **SRS** has been used.

The accomplished experimental activity can be divided in three steps that will be discussed in the following sections.

	horizontal	vertical
Average [<i>mm</i>]	2.084	2.011
Uncertainty [<i>mm</i>]	0.035	0.045
Propagated error [<i>mm</i>]	0.073	0.090

Table 4.1: Measurement of uncertainty in the positioning

4.1 Coupling procedure

The **NPD** detector and the crystal have different dimensions and a coupling procedure had to be developed in order to avoid setup misalignment. In particular the **NPD** detector area is $260 \times 260 \mu m^2$ and has been realized in a silicon die that contains several other detectors and test structures. The chip die is glued and bonded in a ceramic package¹. This package has been used to align the pixel with the scintillator, a **LYSO** crystal² of $1 \times 1 mm^2$ area and $15 mm$ length. It can be foreseen that a misalignment of the sensors with respect to the package can cause a reduction of the detection efficiency. For this reason an evaluation of the error in the position of the die with respect to the ceramic package has been performed taking photos of 10 samples of **FBK** chips that contains the **FBK** pixel. The 11 photos in figure 4.1 have been taken with a Leica microscope using the same magnification. The **FBK** pixel is the little dark square visible near the top-left corner of the die. The last photo has been used to evaluate the real dimensions in the 11 photos, knowing that the pitch of the pads in the package is $1.27 mm$. The linear distance in pixels between two points of the photos was measured over the image using the open-source software Gimp³ and its ruler tool. A different uncertainty has been measured along the vertical and the horizontal directions as reported in table 4.1.

¹ JEDEC Type “A” plastic leaded chip carrier

²Hilger crystal

³<http://www.gimp.org/>

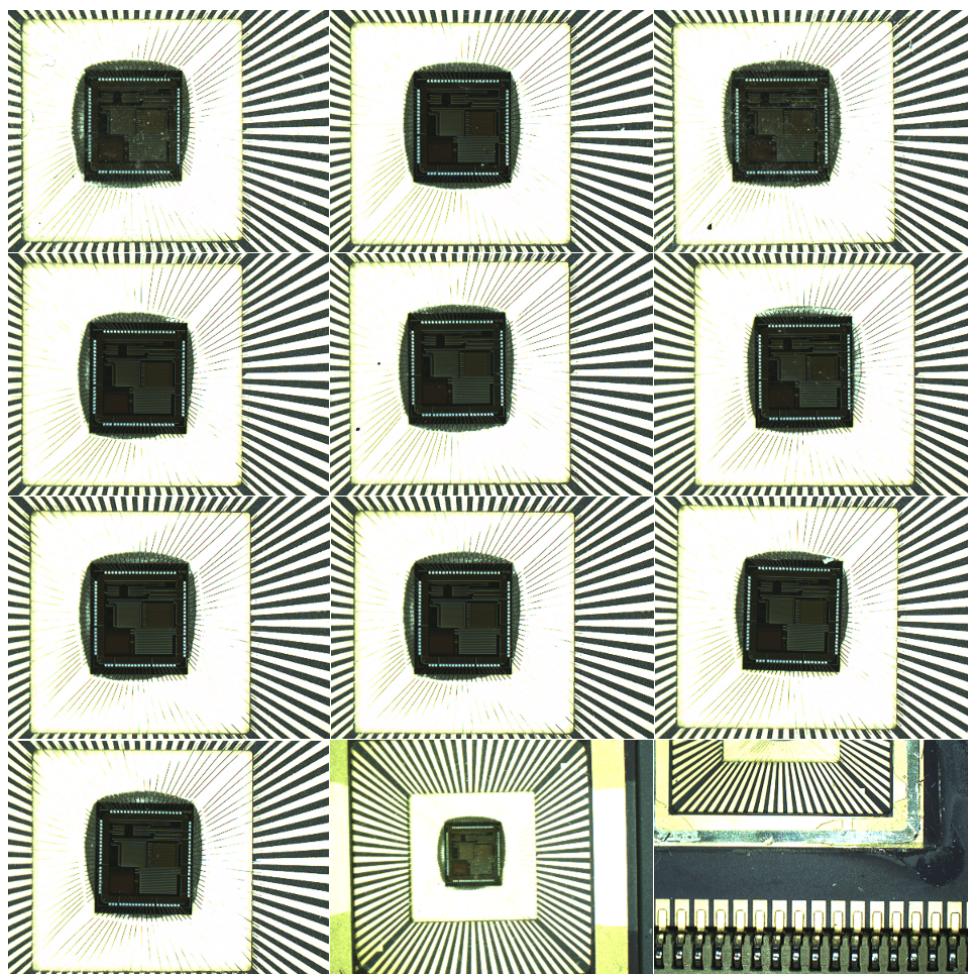


Figure 4.1: Photos of the ten samples used to estimate the misalignment of the sensor with respect to the package. The last two photos have been used to extract the measurement in *mm* reported in table 4.1

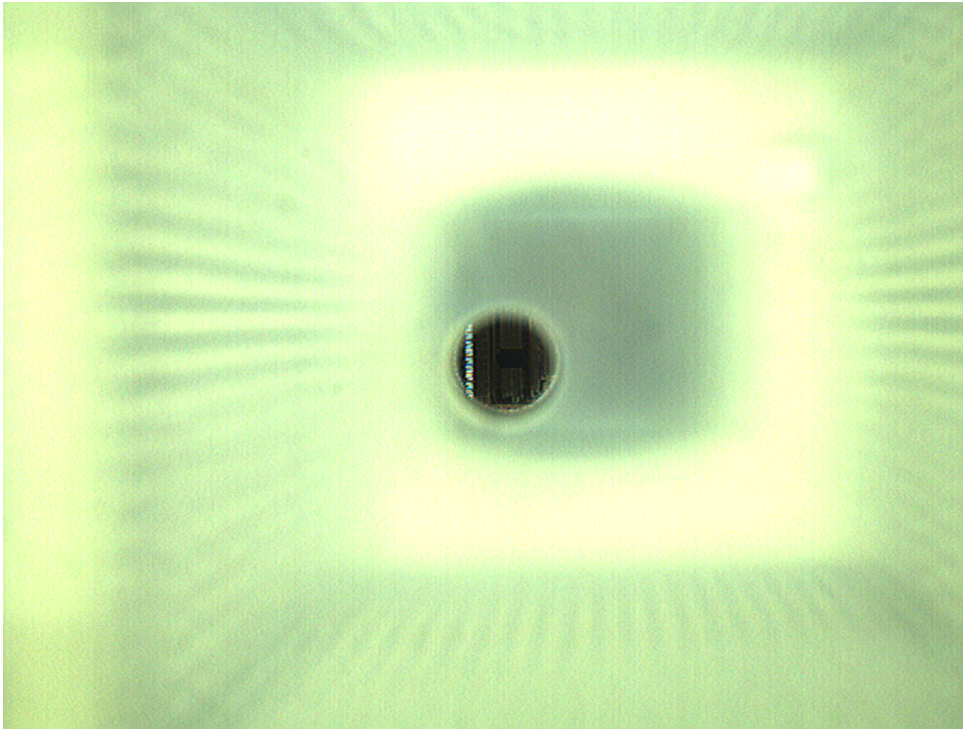


Figure 4.2: Position of the hole in the plastic support and the sensor die.

In order to allow an easier coupling procedure between crystal and sensors a Plexiglas guide, that fits the dimension of the ceramic package, has been built by the mechanical service of the Physics Department at the University of Trento. A hole of 1.4 mm in diameter was drilled on the Plexiglas adapter to guide the crystal over the **FBK** pixel. In Figure 4.2 the position of the pixel is shown with respect to the plastic support hole. Some bonding pads are still visible on the left and therefore are exposed to the contact with the crystal. This unwanted effect was unavoidable due the limited spacing between the sensor active area and the pad ring.

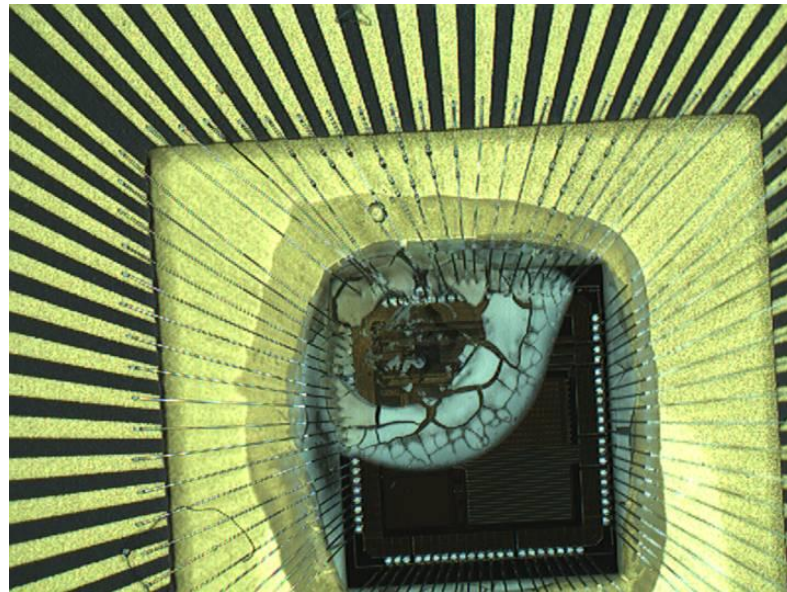


Figure 4.3: A photo of the chip after some days of measurements.

4.2 Optical Glue

An optical grease⁴ has been chosen to couple with the **LYSO** crystal both the **SiPM** and the **NPD** detector. The chosen optical grease dries out if exposed to the air for long periods (days). The dried grease is a problem with the actual setup. In figure 4.3 the **NPD** detector is shown after some days of measurements. The problem is related to the transparency of the medium that decreases once it has dried, and to the bonding which can be damaged if the crystal is detached from the surface of the sensor. In figure 4.4 a photo of the analog **FBK SiPM** is shown. The photon sensitive area is the inner 1 mm^2 area. On the lower right corner of the device we can notice the resin used to protect the bonding wire during the alignment procedure.

⁴Cargille Optical Grease. Initially we evaluated the use of Meltmount thermo- plastic material to couple the **SiPM** with the crystal but due to the mechanical fragility of the joint the Cargille optical Grease has been finally chosen.

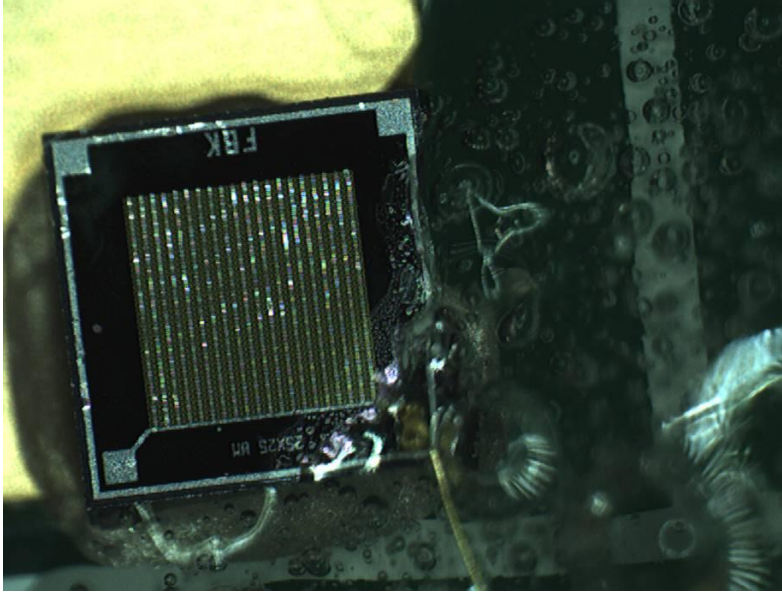


Figure 4.4: **FBK SRS** analog **SiPM**.

4.3 Gamma detection

In order to evaluate the performance of the **FBK** pixel used as a γ -ray detector, and to compare the results with the performance of the **FBK SiPM**, we used the experimental configuration depicted in figure 4.5. We coupled the **SiPM** and the **NPD** prototype to the two sides of the same crystal and we compared the efficiency in detecting gammas that are produced by radioactive sources placed in the proximity of the crystal. We defined the efficiency as the number of events that the two sensors are able to detect in a minute. An oscilloscope [76] measures the time elapsed during the acquisition of a given number of triggers. The two sensors generate the trigger in two different ways. The **SiPM** generates an analog signal directly read by one channel of the digital oscilloscope and the trigger is generated when the rising edge of the signal exceeds a defined threshold (see figure 4.7). To generate a trigger from the **FBK** pixel a firmware developed for the **FPGA** board has been used because, as previously noticed, the **NPD** does not provide an analog output. As described in chapter 2 the **SOI CMOS**

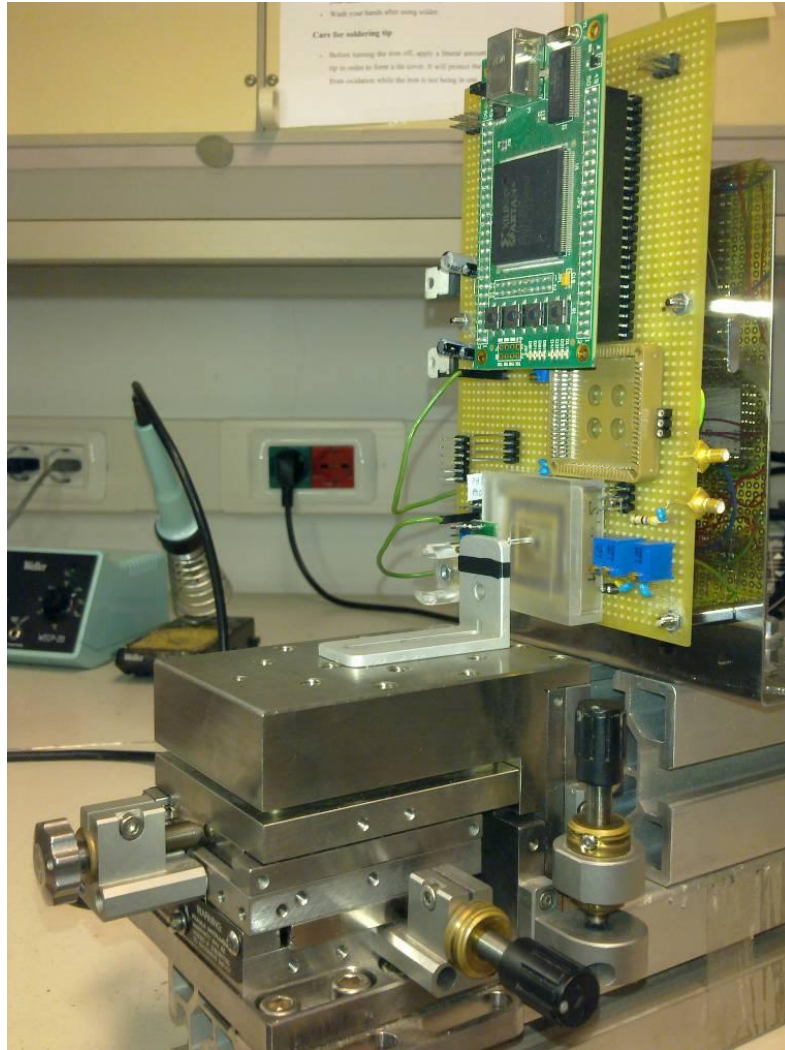


Figure 4.5: Mechanical setup to hold the **CMOS SPAD** detector and the **SiPM** coupled to **LYSO** crystal. The Plexiglas guide used to align the **FBK** pixel with the crystal keeps also the sensor in the horizontal position. The **SiPM** is the green device attached to the aluminum holder in the photo. A 3 axis micrometer has been used to align the **SiPM** with the crystal.



Figure 4.6: Experimental setup used for the experiments with γ -ray sources. It can be noticed the position of the sources that are contained in the red and blue boxes. Two different sources (low activity ^{133}Ba and ^{22}Na) have been used to reach a number of events well discernable from the background radiation activity. The sources are positioned as close as possible to the crystal.

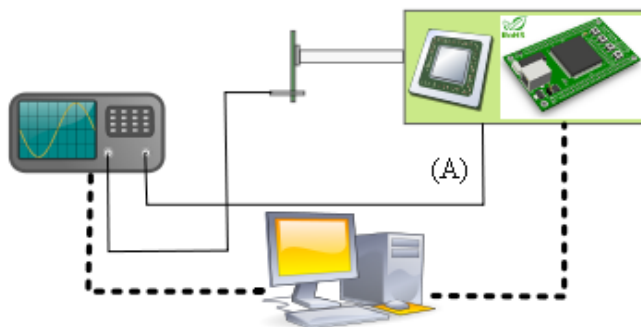


Figure 4.7: Sketch-up of the measurement

detector was designed to count photons that arrive on the surface of the **NPD** prototype during a given time-window and to register the measured value in a digital shift register. To perform the measurement the **FPGA** first opens the exposure time window and reads the shift register every $6 \mu s$, fast enough to prevent false positives related to pixel noise. Then **FPGA** performs a fast data extraction from the **SPAD CMOS** shift register and a comparison of the integrated value with a threshold of three photons.

If a number of photons greater than the threshold is revealed the **FPGA** produces the gamma detected signal (signal A in figure 4.7) that is connected to the second oscilloscope channel. The mechanical setup shown in figure 4.5 has been built to perform the measurements.

In figure 4.6 a photo of the final setup taken from the top side can be seen.

In table 4.2 are reported the number of events triggered by the oscilloscope per minute, i.e. the activity, measured using the **SiPM** as trigger (**SiPM** trigger - sources) and the activity measured setting the “gamma detected” signal as trigger (**CMOS SPAD** trigger - sources). It has been reported also the background activity measured setting the gamma-detected signal as trigger.

The measured ratio between the activity of the two sources measured

	SiPM trigger-sources	CMOS SPAD trigger-sources	background radiation
Average activity [events/min]	617.80	144.22	63.12
Std. Dev. [events/min]	20.52	6.54	3.38

Table 4.2: Experimental results of CMOS SPAD vs SiPM in detecting gamma events.

with SiPM and with the FBK pixel is 4.28. This activity is measured at the two ends of the same $1 \times 1 \times 15$ mm LYSO crystal, under the same geometrical condition. If we assume that the number of events detected by the two sensors is proportional to the detection area we can compare this number with the ratio of the two areas corrected using the fill factor. The ratio between the SiPM corrected area and the FBK pixel corrected area is 5.54. The number should be further corrected using the PDE of the two sensors. Unfortunately the PDE has not been measured for the SiPM biased with the overvoltage used during the experiment. Moreover, the SiPM PDE is measured with a collimated light source and is not directly applicable to the angular distribution of the light that is generated by the crystal. From the values reported in literature we can assume that the two PDEs are similar. The residual difference between the measured value and the expected value can be explained considering the experimental difficulties encountered in the construction of the setup, especially in trying to couple with the same optical efficiency the two detectors at both ends of the crystal.

4.4 Conclusions

The validity of the CMOS SPAD solution has been confirmed by the results obtained using the NPD prototype where, thanks to the high fill factor (48%), it was possible to do a quantitative comparison with SiPMs,

representing the state-of-the-art technology for solid-state PET detectors. The two technologies exhibit similar relative (i.e. normalized to the device area) sensitivity. Unfortunately the small active area of this sensor did not allow carrying out a comparison of the energy and timing resolution performance between CMOS SPAD and SiPM.

Chapter 5

Light yield in crystals

In the previous experience an inherent assumption has been done. The assumption is that the two detectors are exposed to the same mean amount of light collected at the two sides of the same crystal. The assumption is adequate for the purpose of the previous experiment, that, as stated, can be considered more as a proof of concept than the characterization of a detector, but, in general it is not true for two different detectors. In fact the hypothesis doesn't take in consideration the differences at the interfaces between the two sensors. In this chapter the propagation of light between the interface and the detector is discussed, as well as the effect of the wrapping in the light guide properties of the crystal. In particular an experimental evaluation of the dependence of the light yield at two ends of an **LYSO** has been performed using two **SiPMs**. As previously observed in 4.4, the **NPD** detector prototype is too small and too difficult to use as detector in a gamma ray experiment. On the other hand the **SiPM** is well suited for this application by which the **SiPM** development has been driven during the last ten years. Moreover, thanks to the collaboration with **FBK SRS**, it has been possible to obtain precious information about the surface coating of the device. This information have been here exploited to propose a simulation framework that can be used to apply the values

of PDE, measured using collimated light sources, to non collimated light sources. This section is focused on the SiPMs (the NPD prototype is no more used and discussed), and introduces the following part of this thesis, where the use of γ -ray detectors built using SiPMs are discussed for TOF Ps application.

5.1 Case history

The configuration used in the characterization of the NPD, with two detectors glued at both sides of the crystal, has been re-configured using only SiPMs to obtain an experimental data set. This configuration has been studied in literature with both experimental and theoretical approaches using PMT, HPD and SiPM. In particular, using PMT as detectors, the Crystal Clear Collaboration¹ at CERN, deeply studied during the 90's the scintillation properties of *Bismuth Germanate* (BGO), *Yttrium Aluminum Perovskite* (YAP) and LYSO, as well as the effect of wrappings in light propagation. In particular, if we consider a detector coupled to a crystal having a prism shape similar to the one used in our previous characterization (i.e with a square base and length ten times longer than the base side), it has been demonstrated that the *Distance Of Interaction* (DOI) can be estimated from the quantity of light reaching the detector. In the introduction it has been noticed that prototypes of PET scanners [67, 68] that exploit the DOI determination have been recently proposed. The relation between DOI and the quantity of light reaching the detector side can be studied using Monte-Carlo simulations and verified with an experiment. Let us consider a detector composed by a crystal with a length of 20 mm and a base of $3 \times 3 \text{ mm}^2$. A Monte-Carlo first evaluation of the behavior of the

¹ “The main aim of this project was to develop scintillating materials which would be suitable for use at the LHC collider. Indeed, none of the existing scintillators at that time had the appropriate characteristics for use in the extremely demanding LHC application.” <http://crystalclear.web.cern.ch>

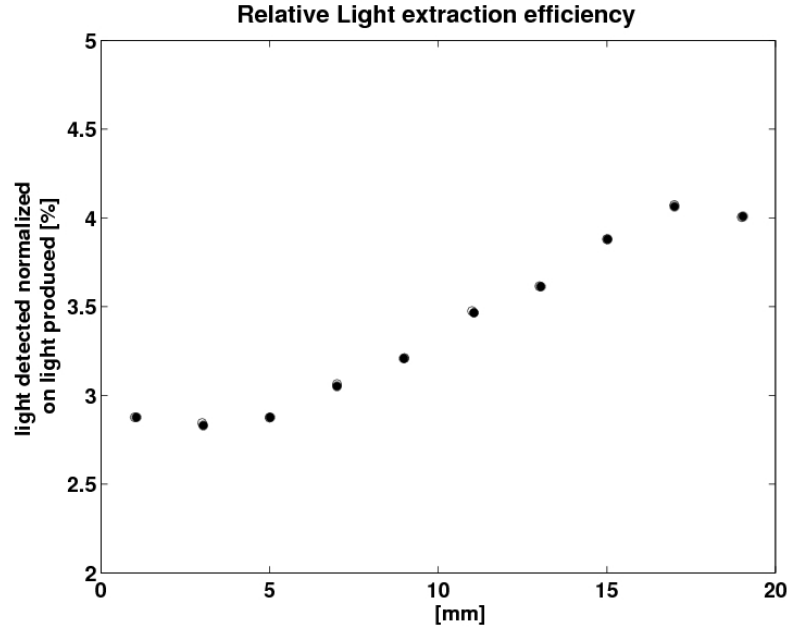


Figure 5.1: Simulation of light output versus DOI in a crystal of 20 mm . The detector is placed at $x = 20$ mm

light traveling inside the crystal has been performed building the geometry of the crystal in a direct Ray-tracer and assuming a diffusive wrapping of the crystal. Simulating bounces of rays from point sources placed along the the axis of the crystal we can study the dependence of the quantity of light reaching the detector side and the coordinates along the axis.

In figure 5.1 the simulated light output, for a detector placed at 20 mm , is shown as a function of the event position along the crystal axis.

Apart from the very ends of the crystal, where the number of interactions between light and wrap is lower, a quite good linear dependence of the light output on the position is observed. The maximum ratio between the light outputs at the two ends of the crystal is equal to 1.33, meaning that when a gamma ray interacts near one end of the crystal, i.e. in the proximity of one of the two detectors, the ratio between the two signals yielded by the two sensors should be 1.33.

In our experimental setup, we used an optical grease (Rhodorsil pate

7), having an index of refraction of 1.4, to couple two nominally identical SiPMs placed at the opposite faces of a 20 mm crystal wrapped with Teflon. The two SiPMs have 3600 cells, each of $50 \times 50 \mu m^2$, with a total area of $3 \times 3 mm^2$. The rest of the experimental apparatus is very simple. As in the previous experiment two channels of the digital scope have been used to read-out the voltage drop on the 50-ohm input resistance produced by the current bursts of each SiPM. No further amplification or signal shaping were used, so that the area of the digitized output (expressed in $[V \cdot s]$) is directly proportional to the number of photons detected.

A ^{22}Na γ -ray source has been positioned near the center of the crystal. In this configuration we can assume that all the points of the crystal absorb a gamma ray with a probability that depends on the distance between that point and the source, and on the amount of material placed in between.

The crystal can be simplified as a wave-length shifter that linearly transforms the energy of a γ -ray in a number of photons. The photons are collected at the two ends of the crystal with the losses described by figure 5.1. As previously introduced (see equation 1.2.1), the area of the signal of the SiPMs can be assumed as linearly dependent from the impinging photon flux. As a result, the area of the signals of each of the two SiPMs in the detector can be assumed as proportional to the energy of the incoming γ -rays.

The energy spectra for the two individual SiPMs are reported in figure 5.2. In both graphs we can recognize two peaks corresponding to the two characteristics ^{22}Na γ -rays, having energies at 511 keV and 1.275 MeV. Values extracted from the gaussian fitting of the 511 keV peak are reported in the captions. It can be seen that the signals from the two devices are different: this is due to the different gain resulting from using the same bias voltage for both SiPMs although their breakdown voltages are slightly different. From figure 5.2 it can be noticed that the energy resolution values

are poor. This is not surprising with this setup, because the light output depends heavily on the point of interaction and this has a detrimental effect on the energy resolution.

If we linearly combine the output of the two detectors, we obtain the energy spectrum shown in figure 5.3, which exhibit an energy resolution still not optimized but definitely much better than the two energy resolutions measured with the single detectors. This confirms that the outputs of the two single channels are strongly linearly self-correlated.

This effect is further demonstrated by the graph of the signal correlation shown in figure 5.4, where a symmetrical cloud of points can be observed. The lowest border of this scatter plot is due to the interactions occurring near the SiPM connected to Ch. 1 of the scope (corresponding to the x axis), whereas the upper border is due to the interactions occurring at the other end (SiPM connected to Ch. 2, y axis). In this scatter plot, points relevant to the peak at 1.275 MeV are easily visible in the upper right zone, as isolated points. As expected, they are well aligned perpendicularly to the symmetry axes of the scatter plot.

The linear regression fit to the data is found to have a slope of $\simeq 1.32$, in agreement with the different gains of the two SiPMs. By chance this number is very close to the simulated ratio of maximum and minimum light outputs of figure 5.1. This is the reason why the bisector in figure 5.4 well fits the lower border of the scatter plot. Although this aspect should be further investigated, it is indicating that simulations correctly predict the position dependence of the light output.

5.2 PDE and crystals

To estimate the number of photons detected by a SiPM for a given incident photon flux equation 1.2.1 could be used. In this formula the number of

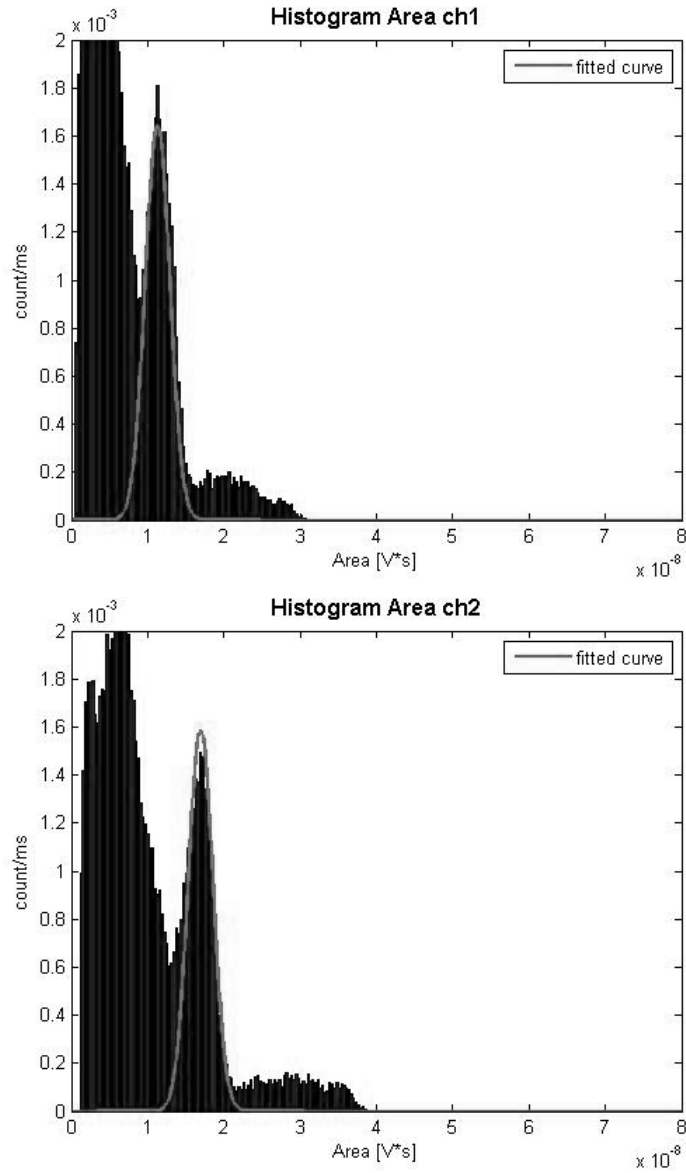


Figure 5.2: Energy spectra of the signal read on ch1 (top), and ch2 (bottom). The values of peak positions are: ch1 1.129, ch2 1.69 [$V \cdot se - 8$] The values of Energy resolutions are: ch1 46.72%, ch2 31.15 %.

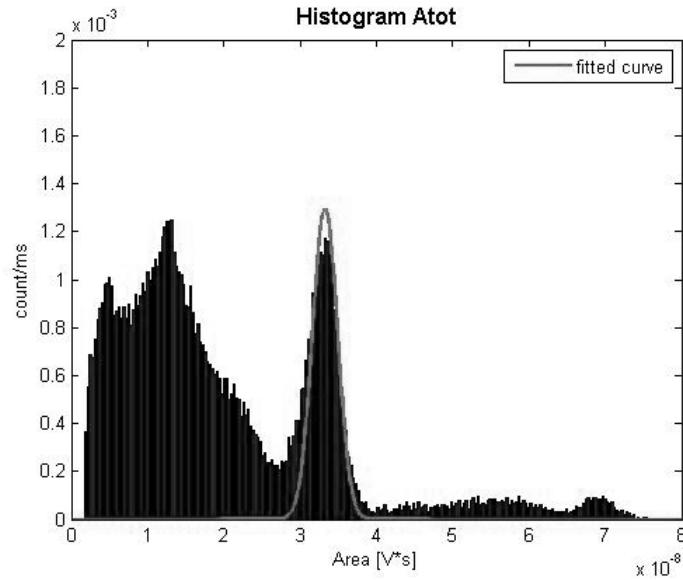


Figure 5.3: Energy spectrum of the signal obtained by the linear combination of the two channels. Value for Energy resolutions is: 16.12%. Peak position is $3.32 [10^{-8}V \cdot s]$

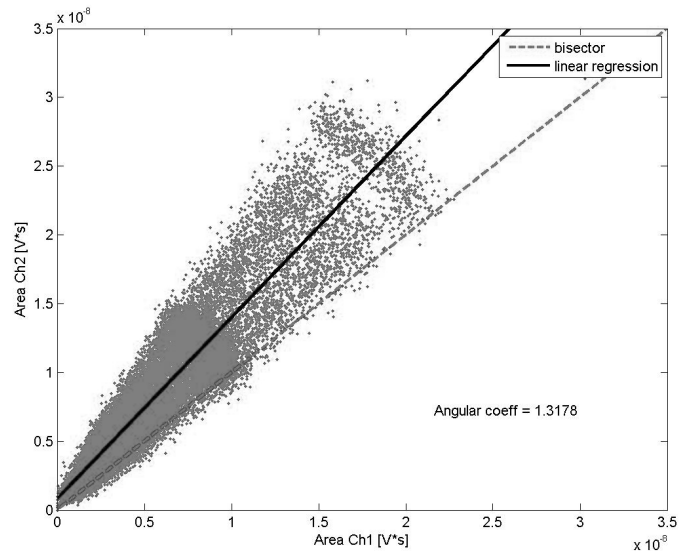


Figure 5.4: Correlation of signals of the two **SiPMs** coupled at the opposite sides of a $3 \times 3 \times 20 \text{ mm}^3$ crystal coated with Teflon wrap.

detected photons is expressed multiplying the flux of photons by the **SiPM PDE**. As previously stated the measurement of **PDE** is done by using collimated light sources. This is an experimental condition that differs from scintillator light output. Indeed scintillator light output is spread with a large angular power distribution that depends on many system factors. In a particular assembly, the performance are critically dependent on some practical setup choices, such as the optical grease used as coupling medium, the geometry of the crystals and their coatings.

In the literature, some studies of systems composed by detector-scintillator assemblies are carried out using experimental practice, optical simulations or a mixed approach [84] [85].

In the following a method to calculate the output of a detector for a non collimated light flux is proposed. This method can be applied to study the light propagation inside the scintillator crystal and how it is affected by the properties of different coatings and interfaces. Using this method the relative importance of different factors in determining the light output can be estimated.

5.2.1 Optical Simulation

In this section the quantities extracted from the simulations have been defined. In the following, the discussion will refer to the set-up depicted in figure 5.5. In the simulation gamma rays travel parallel to the crystal axis entering from the surface A^i in figure 5.5.

The ratio of detected photons, $P_{detected}$, to the photons generated by the deposition of the whole energy of a γ -ray, P_{gamma} , can be defined as "light output", η , as suggested in [86].

It can be expressed as the product of three factors with the **PDE**:

$$\eta \equiv \frac{P_{detected}}{P_{gamma}} = \eta_{crys} \cdot \eta_{med} \cdot \eta_{coat} \cdot PDE \quad (5.1)$$

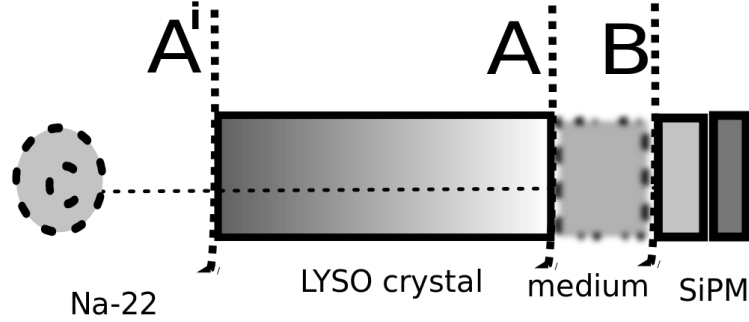


Figure 5.5: Sketch of the simulated setup, showing the radioactive source, the crystal, the optical grease and the detector (SiPM)

$\eta_{crys} = f(\alpha, x, y)$ is the light output at interface A of figure 5.5. This quantity describes the light propagation inside the crystal and depends on the angle of incidence α , formed by the light and the normal to the surface A, and on the position of the light generation inside the crystal (x indicates the position along the crystal axis while y indicates the distance between the point of interaction and the axis in a section parallel to the surface A). This dependence will be studied in section 5.2.3, where it is discussed how the simulated angular distribution of η_{crys} changes varying the point of interaction.

$\eta_{med} = f(\alpha, n_{medium})$ is the light output at interface B of figure 5.5. The angular distribution of η_{med} depends on the refractive index of the medium. This dependence is analyzed in 5.2.4. In this case the average light output after a large number of gamma interactions has been studied. To model the energy deposition of a large number of γ -rays inside the crystal the model presented in section 5.2.2 has been used.

$\eta_{coat} = f(\alpha, coating)$ is the light output of the **SiPM** coating. Its angular distribution is determined by the number, the thickness and the refractive index of the dielectric layers that are deposited over the **SiPM**. This quantity is discussed in 5.2.5.

Results for the average light outputs (i.e. the sum of light outputs calculated for different angles, η_{cris} , η_{med} and η_{coat}) are reported in 5.2.6.

5.2.2 Energy Deposition

The simplest approximation of gamma-crystal interaction, namely the Lambert-Beer Law, has been used to describe gamma-matter interaction. The Lambert-Beer Law states that a gamma ray has probability equal to

$$P(x) = e^{-\frac{x}{d}} \quad (5.2)$$

of non interacting after having traveled a distance x in a crystal. The extinction coefficient d or absorption length, is a value that is normally given by the crystal producer. In the interaction with the crystal, the gamma ray deposits all its energy. In the experimental activity Hilger Crystals **LYSO** scintillators have been used having a $\frac{1}{d}$, defined in previous equation, of $0.87cm^{-1}$. The value of the extinction coefficient has been used to divide the crystal in subsequent volumes. In each of these volume the gamma ray has a similar probability of depositing its energy.

In the following the volumes calculated in this way has been called "equal probability volumes". In the Montecarlo optical simulations the following has been assumed: all the light produced by the gamma energy deposition is generated from one single point, located along the crystal axis at the center of an equal probability volume. This simplification is similar to that introduced in [86] and is discussed in the next chapter.

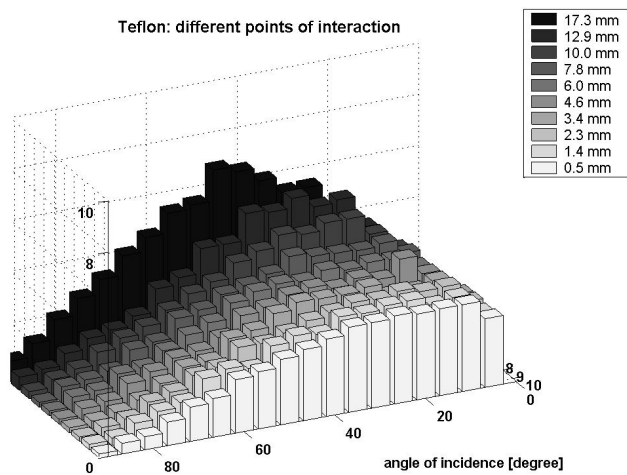


Figure 5.6: Light power distribution at the crystal interface for different points of interaction - Diffusive coating. The diffusive coating is typically obtained in experimental practice wrapping the crystal with Teflon

5.2.3 Relative light distribution at crystal interface

The histograms in figure 5.6 and 5.7 give the simulated angular distribution of the incident light at surface A of figure 5.5, in the case of a diffusive and a mirror coating respectively. The distribution is expressed in terms of percentage of light incident with respect to the light generated. The parameter η_{cris} , reported in 5.2.6, is given by the sum of the percentages over all the angles of incidence.

The axial coordinates that we used in this calculation are the centers of the previously introduced equal probability volumes and are reported in the legend of figures 5.6 and 5.7 as axial distance from surface A^i . We can note that in the Teflon case the light distribution changes, for a given angle of incidence, changing the point of interaction. In particular it increases for interactions that occur closer to the surface A and this increment is larger for low angles of incidence. In figure 5.7 we can note that with mirror

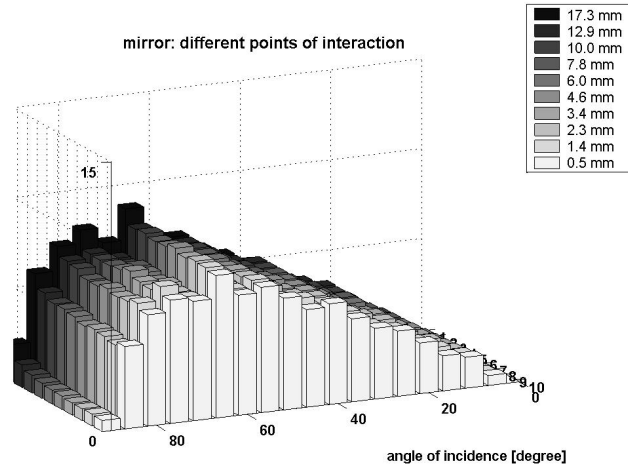


Figure 5.7: Light power distribution at the crystal interface for different points of interaction - Mirror coating

coating only minor changes are predicted from simulator.

5.2.4 Light distribution at sensor interface

The angular distribution of incident light at interface A of figure 5.5 is modified according to Snell Law when the light enters in the subsequent medium. Cerium doped silicate based crystals have a high refractive index, so that, passing through the interface to a medium with a lower index of refraction, it causes a decrease of the transmitted power and a redistribution of the light power incident at low angle.

Figure 5.8 shows how the two light distributions, relative to the diffusive interface (top) and the mirror interface (bottom) respectively, are modified by the coupling medium properties. The initial distributions are obtained by summing all the light distribution of calculated equal probability volumes. The light distribution for the diffusive coating is less affected by the interface; generally speaking, simulations predict that a larger quantity of

light reaches the detector if the crystal is coated with a diffusive layer, this observation is confirmed by experimental practice [87].

5.2.5 Light transport inside SiPM coating

Light propagation through an arbitrary number of dielectrics layer has been modeled solving optics equations with the calculation procedure explained in [88].

$$\frac{(rTE + \cos(2\phi) \rho_r - \sin(2\phi) \rho_i) ((\cos(2\phi) \rho_r - \sin(2\phi) \rho_i) rTE + 1)}{((\cos(2\phi) \rho_r - \sin(2\phi) \rho_i) rTE + 1)^2 + (\sin(2\phi) \rho_r)^2} \quad (5.3)$$

By this procedure, knowing the thickness and the refractive index of every layer deposited over SiPMs, the transmission coefficient can be calculated at a given λ (which in our case is 425 nm , the peak emission of the crystal), as a function of the angles of incidence at the outermost layer (surface B of figure 5.5).

In figure 5.2.5 some examples of such calculations have been reported for different semi-infinite mediums (with a different index of refraction) which simulate the grease coupling the scintillator to the SiPM.

5.2.6 Simulation resume

Results for the light outputs at each interface, η_{cris} , η_{med} and η_{coat} , summed over the angles, are reported in table 5.1. Multiplying the products of one column for the PDE gives η , the total light output in that configuration.

5.3 Conclusions

In this chapter a simple experimental setup has been proposed to verify the detection properties of two SiPMs, coupled at two ends of a scintillator,

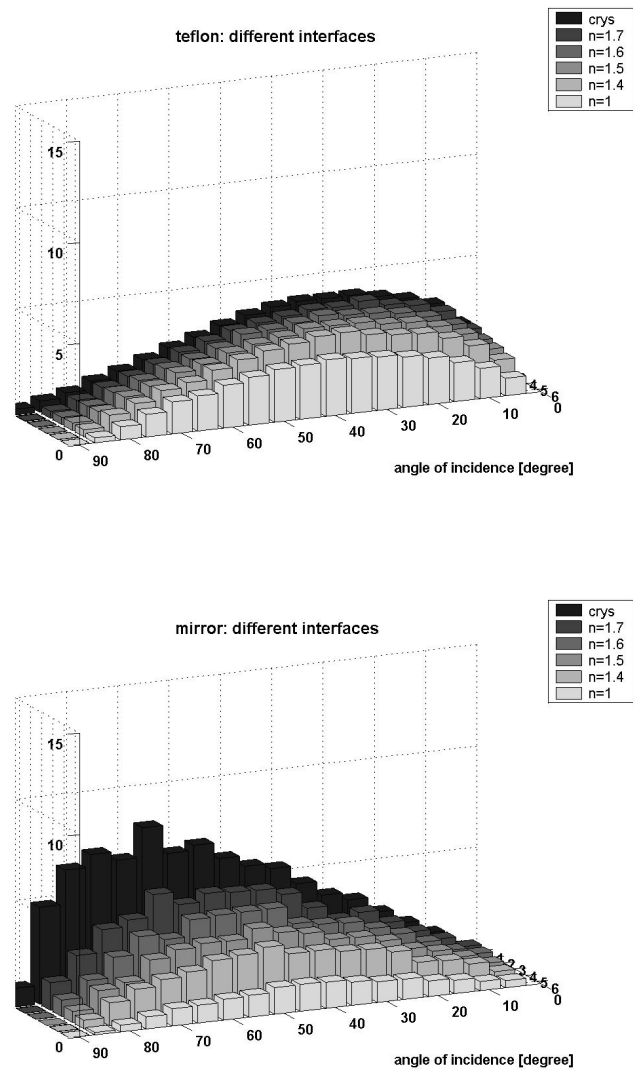


Figure 5.8: Angular distribution of the light output for different refractive indexes of the coupling medium: (top) Diffusive coating, and (bottom) mirror coating.

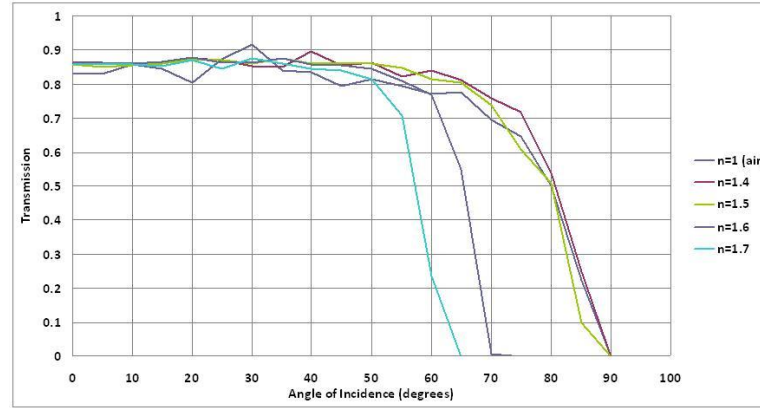


Figure 5.9: light transmission to the **SiPM** for different angles of incidence at the surface B for different mediums, i.e. the coupling grease between the crystal and the **SiPM**. In the legend n is the index of refraction of such medium

light outputs	$n=1.7$	$n=1.6$	$n=1.5$	$n=1.4$	$n=1$
teflon coating					
η_{crys}	0.47	0.47	0.47	0.47	0.47
η_{med}	0.98	0.96	0.94	0.90	0.68
η_{coat}	0.69	0.76	0.83	0.84	0.80
mirror coating					
η_{crys}	0.83	0.83	0.83	0.83	0.83
η_{med}	0.67	0.55	0.46	0.38	0.17
η_{coat}	0.53	0.67	0.81	0.82	0.80

Table 5.1: Calculated values for light output at different refraction index coefficients. In the first half light output for teflon coating are tabulated, in the second half data for mirror coating are reported

wrapped with white diffusive Teflon coating. The setup has been proposed to verify the extend of the previous assumption that, in a similar setup the light is distributed equally at the two ends of the crystal. As discussed, the results are coherent with that simulated with the aid of a Monte-Carlo ray-tracer.

Starting from this experience, a simulation framework that allows to apply the measured value of **PDE** to not collimated light sources has been proposed. The simulation calculates the angular power distribution of a light source and how it is modified by the interaction with a series of optical elements before light absorption.

This method has been applied to the light output of a scintillator crystal coupled to a **SiPM**, assuming a deposition of energy in the crystal that follows the Lambert beer law. In this way the weights of three factors in the optical system composed by a **LYSO** crystal and a **SiPM** has been studied, i.e. the three indexes of refraction of the coupling medium, of the crystal and of the detector coating.

To draw a conclusion we can state that a mirror coating gives some advantages in terms of energy resolution, since the light output is not position dependent. On the other hand the same simulations predict that the overall light output is more prone to be affected passing through successive optical elements due to an angular distribution shifted towards great angles.

It is fair to note that many experimental issues can afflict the application of this kind of models. In particular the application of this model would lose motivation in presence of bubbles (see figure 5.10), imperfection of crystal and glues, scratches, etc. On the other hand this imperfection are difficult to model and can be in some sort avoided with a careful experimental practice.

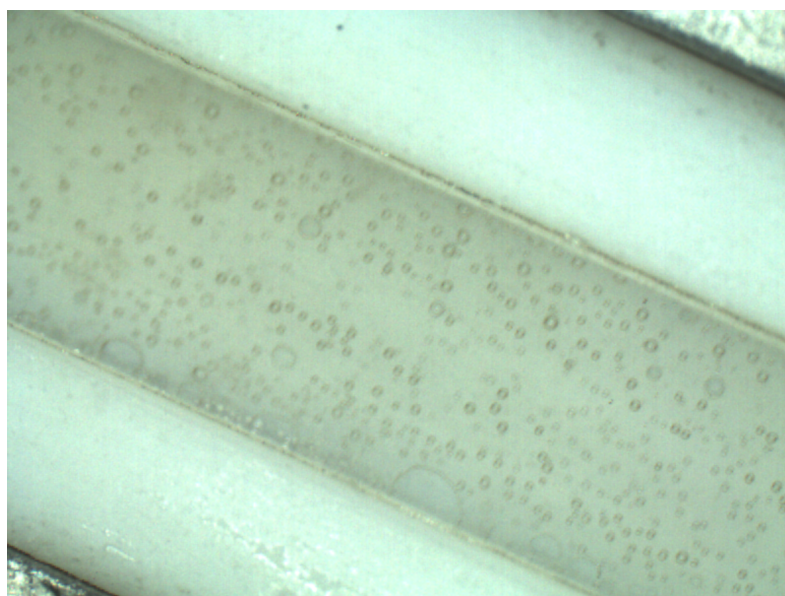


Figure 5.10: micro-photography of bubbles between a crystals wrapped with Teflon in one experiment

Chapter 6

Energy deposition

In the discussion of the previous chapter the energy deposition of γ -rays are assumed following a Lambertian Beer Law. To refine the model SLitrani¹ [82], a C++ library to simulate photon transport using Monte-Carlo methods, has been used to simulate the interaction between γ -ray and matter. SLitrani is based on ROOT, a C++ framework developed by CERN for data analysis [77]. In this short description I will focus on the physic assumption that lies behind the code of the C++ class TLitgamma in SLitrani, putting in the footnotes some indications that should help the reader that wants to follow the discussion in the code source of the program². TLitgamma models the interaction between γ -rays and matter and has been exploited to write the simulation routine used in the following chapter.

6.1 SLitrani structure

The geometry of the simulation is implemented using the geometry package of the ROOT framework. The emission of γ -rays are associated to a volume of the ROOT geometry and can be defined as one of the follows: (i) γ -

¹This library, rather than others (as example the well known GATE and EGS4), has been chosen because it allows the accurate simulation of the light emitted from a scintillator

²The code is publicly available at <http://gentitfx.fr/SLitrani/code/SLitraniCode/TLitGamma.html>

rays are emitted from any point inside the generating volume with an equal probability, or (ii) **γ -rays** are emitted from a specific surface of the geometric volume, or (iii) **γ -rays** are emitted from a point source located in a geometric point inside the volume. The first possibility is useful to model the self-activity of **LYSO** crystals that is due to the decay of the *radionuclide isotope 176 of Lutetium* (^{176}Lu). The former has been used to optimize the shields of the setups in the following chapter.

The program model two types of interaction: Photoelectric effect³ and Compton scattering. The pair production is not implemented and this limits the validity of the results of simulation to **γ -rays** that have an energy in the range where Compton and Photoelectric effects dominates. The SLitrani code calculates both the Photoelectric cross section σ_{PE} and the Compton cross section σ_{KN} , as is described in the following subsection, and then follows the algorithm presented in [90]. This algorithm can be illustrated using the flux diagram in figure 6.1.

In particular, in order to choose between the two process which one has to be applied during an interaction, SLitrani generates a random variable and compares to the ratio between the cross section σ_{PE} and the sum of the two cross sections⁴:

$$\frac{\sigma_{PE}}{\sigma_{PE} + \sigma_{KN}} \quad (6.1)$$

6.2 Cross section calculation

The Photoelectric cross section⁵ cannot be expressed by a simple analytical formula. The values are available in form of tabled data or empirical formulas, with sets of tabled coefficients. As example, tabled data can be

³The recoil electrons are not tracked and thus, with the provided libraries, Cerenkov emission can not be simulated. On the other hand the number of recoil electrons produced at low energy is small [89]

⁴see the code in function TLitGamma::DepositEnergy()

⁵private property TLitGamma::fXsecPhotoEl



Figure 6.1: Flux diagram of γ -ray generation loop as it is implemented in the SLitrani TGamma class. Being based on the algorithm presented in [90] the flux diagram is pretty similar to the one presented in the original article.

obtained browsing the NIST XCOM data base [91] while empirical formula can be found in the source code of the GEANT [92] program. The photoelectric cross section data are provided to the SLitrani framework tabulated for energy values and interpolated with a cubic polynomial. This interpolation follows the recommendations regarding the procedures of data fitting provided by the authors of the NIST XCOM database⁶. After a Photoelectric interaction, if the volume is a scintillator, a number of photons are generated following a linear relationship with the deposited energy. The scintillating photons are supposed to be generated exactly in the point where absorption occurs. This assumption holds if the range of the recoil electrons is small. Unfortunately with SLitrani is not possible to simulate the behavior of the recoil electrons but we can refer to simulations in literature performed using different frameworks. As example in [93] are reported results obtained from ROSI (ROentgen SIMulation) simulations that predicts that a beam of electrons, with an energy of $511keV$, should deposit the 95% of its energy in a range of $114 \mu m$, if directed to a **LYSO** crystal, and of $217 \mu m$ if directed to a **YAP** crystal.

The calculation of σ_{KN} ⁷ is based on the Klein-Nishina probability distribution that gives the differential cross section⁸ of photons scattered from a single electron. Following this distribution we can state that the cross section is given by:

$$\frac{d\sigma_{KN}}{d\Omega} = \frac{r_e^2}{2} \frac{1}{1 + \gamma(1 - \cos \theta)^2} \left[1 + \cos^2 \theta + \frac{\gamma^2(1 - \cos \theta)^2}{1 + \gamma(1 - \cos \theta)} \right] \quad (6.2)$$

where γ is the incident energy in electron mass units⁹, $\gamma = E_0/mc^2$, and

⁶see Interpolation and Combination: at <http://physics.nist.gov/PhysRefData/Xcom/Text/chap3.html>

⁷private property TLitGamma::fXsecPhotoEl

⁸the cross section for a collision process resulting in the emission of particles or photons at a specific angle relative to the direction of the incident particles, per unit angle or per solid angle.

⁹In SLitrani there is the TLitPhys class to store physical constants. The quantities used in this calculation are stored as TLitPhys::fMe and TLitPhys::fMeg

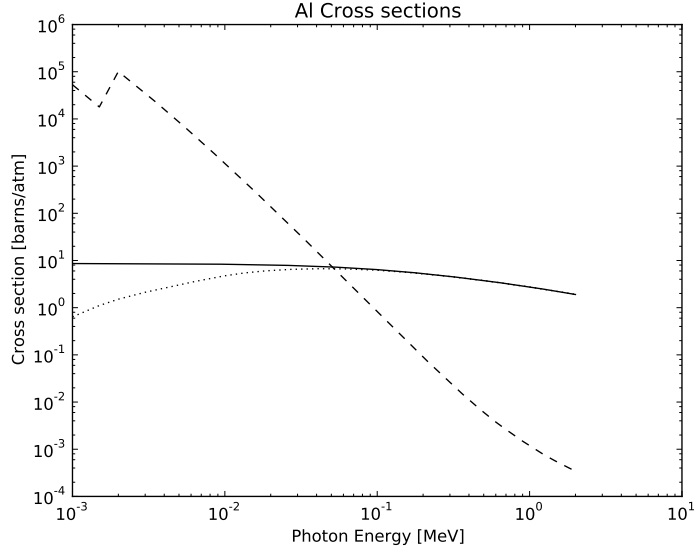


Figure 6.2: Data of Photoelectric and Compton cross sections of Aluminum as extracted from XCOM database (dashed lines) and values of σ_{KN} calculated using Klein-Nishina formula (continuous line). The values can be compared with the ones reported in [90]

r_e is the classical electron radius, $r_e = 2.82 \cdot 10^{-15} m$.

The integral over the solid angle gives a total cross section:

$$\sigma_{KN} = 2\pi r_e^2 \left[\frac{1 + \gamma}{\gamma^2} \left(\frac{2(1 + \gamma)}{1 + 2\gamma} - \frac{\ln(1 + 2\gamma)}{\gamma} \right) + \frac{\ln(1 + 2\gamma)}{2\gamma} - \frac{1 + 3\gamma}{(1 + 2\gamma)^2} \right] \quad (6.3)$$

If we multiply this cross section by the atomic number Z of an atom we obtain the cross section for incoherent scattering; if we want to calculate the cross section of a compound we have to multiply the weighted sum of the atomic numbers where the weight are the stoichiometric coefficients of the formula. This approach overestimates the value of the Compton cross section for low energy values, as can be noticed in the graph of figure 6.2.

6.3 Example of calculations

In figure 6.3 is reported an example of the calculus of the γ -ray transmission in NaI:Tl crystals. A collimated bounce of 511 keV γ -rays has been simulated as impinging perpendicularly on the surface of the crystals. The crystals have large area and thickness in the range 0.2 - 2 [cm]. After traveling inside the crystal, only a portion of the impinging γ -rays is transmitted. If I is the intensity of the out-coming bounce of γ -rays and I_0 is the intensity of the impinging bounce, transmission is defined as the ratio $\frac{I}{I_0}$, and can be directly compared with the probability $P(x)$ defined in equation 5.2.2. In figure 6.3 are reported, for the comparison, the Lambert-Beer transmission calculated assuming linear attenuation coefficient ($\frac{1}{d}$ in equation 5.2.2) of 0.31 and 0.34 [cm^{-1}]. The two coefficients are the ones reported in literature for NaI:Tl crystal. As can be noticed, the Lambert-Beer law under-estimates the transmission with respect to SLitrani calculation at bigger thickness. A reason could be that the Lambert-Beer linear attenuation coefficients are experimentally evaluated, putting sample of the crystal with different thickness between a γ -ray source and a calibrated detector. In this way the portion of γ -ray scattered at surface due to Compton interaction is counted as absorbed. Moreover the SLitrani Library does not model elastic-scattering.

6.4 Conclusions

In this chapter the γ -ray-matter interaction implemented in the open-source SLitrani library has been illustrated. The library has been used to perform the calculation of the following chapter to find the thickness of absorbing shields. From a comparison with the simpler Lambert-Beer model, it can be noticed that the calculation performed with the SLitrani

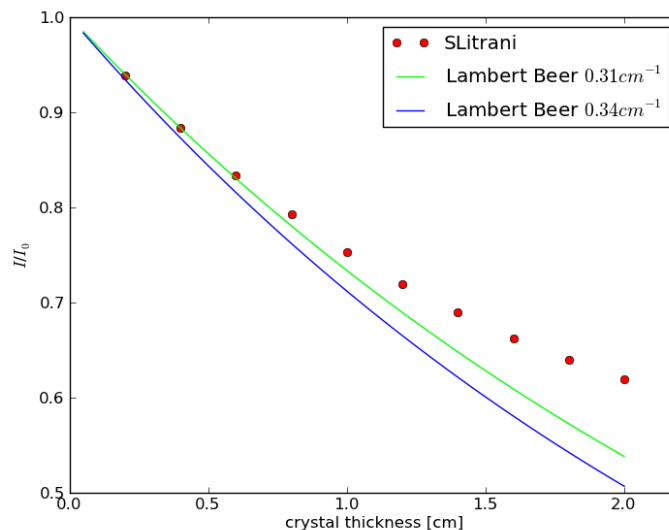


Figure 6.3: SLitrani calculated transmission in crystals of **NaI:TI** having different thickness. In figure are also reported Lambert-Beer calculation. The assumed Lambert-Beer linear attenuation coefficients are 0.31 and 0.34 [cm^{-1}].

algorithm [90] under-estimate the absorption for thickness greater than few millimeters. We can conclude that the thickness of a thick shields designed with SLitrani should be over-sized respect the one calculated with the Lambert-Beer model.

Chapter 7

TOF of Positronium

The outstanding usability that **SiPM** offers, thanks to its dimension and robustness, has been exploited in the design of a new detector for a ***o*-Ps TOF** apparatus. As introduced in section 1.5, a ***o*-Ps TOF** apparatus has been developed by the **IdEA** group of University of Trento in the framework of **AEGIS** collaboration. In figure 7.1 a photo of the Trento experiment is depicted. In this apparatus the e^+ are emitted from a ^{22}Na radioactive source and are selected in velocity, or moderated, by impinging on a foil of tungsten. The fraction of moderated e^+ s is then accelerated by a linear accelerator to a kinetic energy in the order of some keV .

In figure 7.1 is visible the exteriors of the last part of the accelerator (marked with a). The e^+ s hit the sample that can be cooled down with the aid of a cryostat mounted in the lower part of the apparatus (b). **PMT**-based detectors (c) are mounted in a mobile support and form a ring.

The geometry of the setup, based on **PMTs** and **NaI:Tl** crystals, is better visualized with the cross-section reported in figure 7.2. In the caption of the figure the description of the measurement is reported as it has been introduced in section 1.5. The **TOF** experiments, conducted with this laboratory e^+ beam, are time consuming because the apparatus accelerates only about $1 - 5 \times 10^4 e^+/s$. With the present setup acquiring a **TOF**

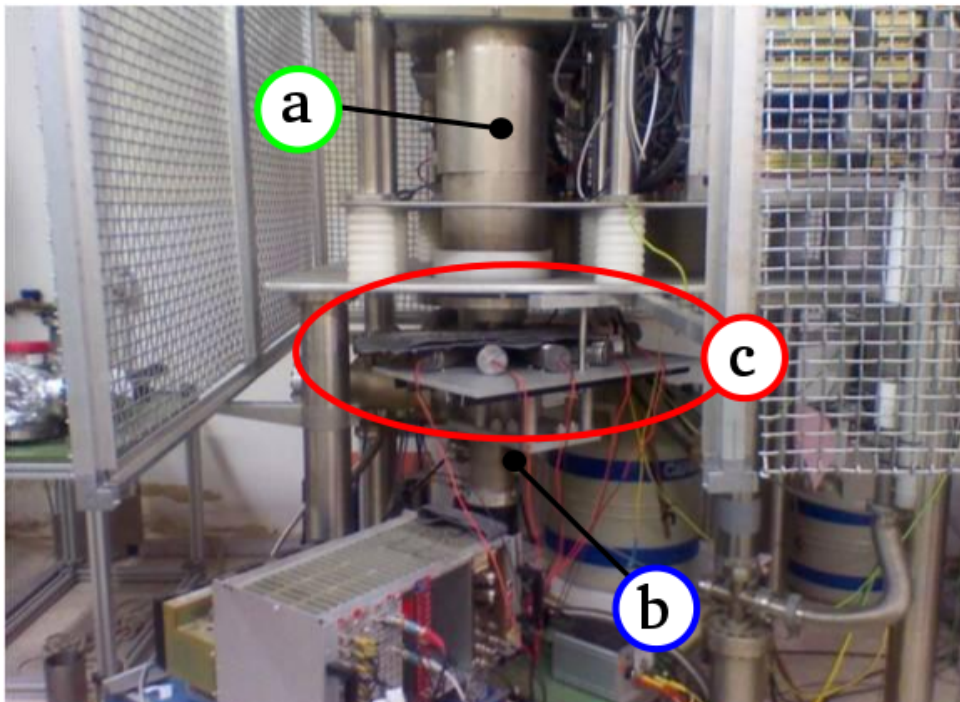


Figure 7.1: Apparatus for cold o -Ps production and characterization of the IdEA Laboratory. Are visible: (a) exterior of the last section of the e^+ accelerator, (b) exterior of the cryostat used to cooled down the sample, (c) the ring of six PMT-based detectors.

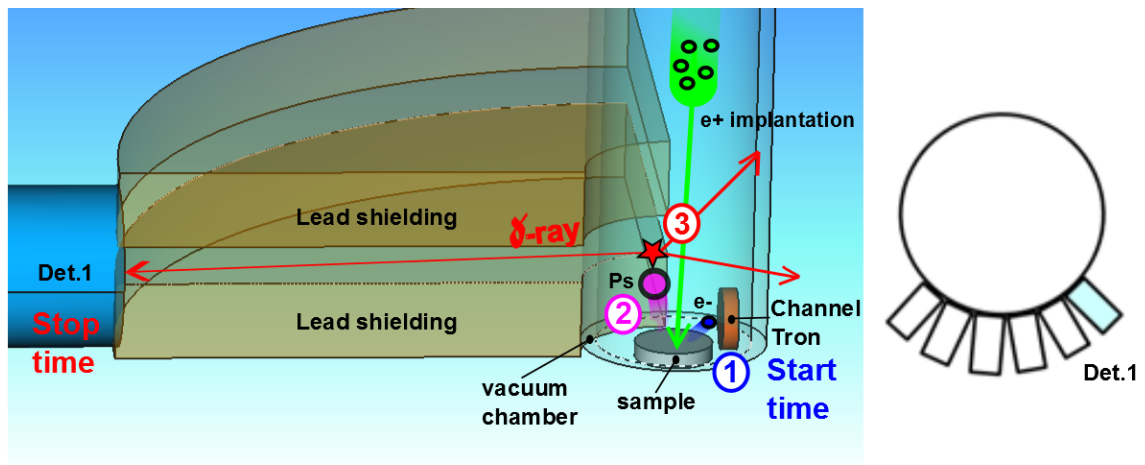


Figure 7.2: Sketch up of the current **PMT**-based configuration and **TOF** measurements. The figure on left represents one of the six **PMT**-based detector currently mounted on the apparatus (as depicted on the right). A bounce of e^+ is linear accelerated towards a cooled porous sample of Silicon. Hitting the surface of the sample, the bounce of e^+ produced a cloud of scattered e^- (1), that is revealed by a ChannelTron. The signal of the ChannelTron fixes the start-time of the experiment. A part of the *o*-Ps that is formed into open pores may escape from the sample (2) and may be re-emitted in the vacuum with a velocity (or temperature) that results from the interactions with the walls of the pores during its travel towards the sample surface. The emitted *o*-Ps travels in the vacuum until annihilation, with the following emission of three γ -rays (3)

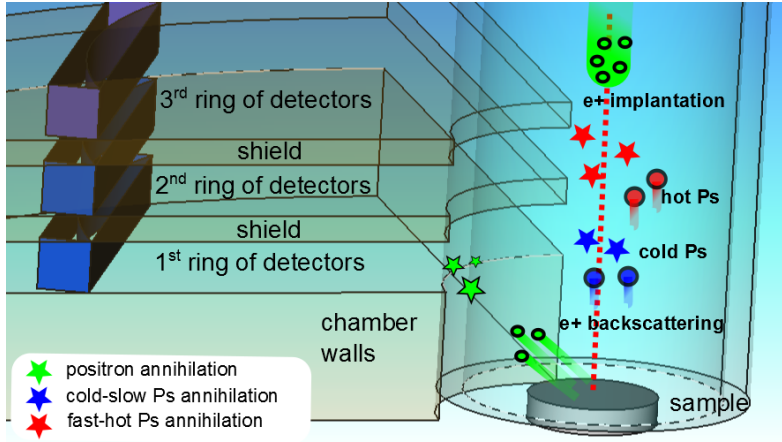


Figure 7.3: Sketch of the setup as can be built using the SiPM-based detector. depicted in the photos of figure

spectrum with 2000 *o*-Ps annihilation events requires about 2-3 measurement days [74]. Therefore the TOF apparatus of Trento is going to be displaced at the high intense e^+ source *Neutron induced Positron Source Munich* (NEPOMUC), that is hosted at the reactor FRMII in Munich and that has one of the world's highest e^+ intensity. The NEPOMUC source, providing $1 \times 10^6 e^+/s$ to the TOF apparatus, will permit to carry out the same measurement in about 1 hour. A further increment of the number of positrons would lead to pile-up problems in the measurements. A typical TOF experiment requires at least three measurements at three different distances from the sample, and a more refined experiment would require increasing the statistics of about a factor of five. An experiment with an intense source will require about 15 hours and this acquisition time has to be decreased in order to avoid the surface contamination of the sample during measurements at cryogenic temperatures.

To further decrease the acquisition time the only solution is to increase the number of detectors in the ring and to add further rings of detectors, separating each ring from the others using shields, as depicted in figure 7.3.

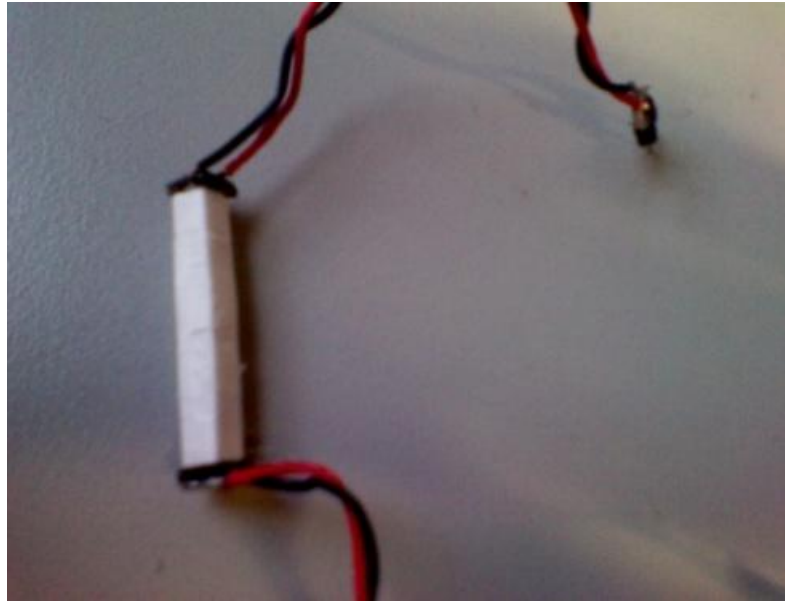


Figure 7.4: Sketch of the setup as can be built using the SiPM-based detector. depicted in the photos of figure 7.4

In figure 7.4 is pictured one of the possible simple detectors that can be built with SiPMs and that should be suitable for this application. The SiPM area is $4 \times 4 \text{ mm}^2$ and the length of the crystal is 30 mm , similar to the geometry that has been studied in chapter 5. A preliminary characterization work has been performed to investigate the use of this detector in the application. The first experiment has been conducted replacing one of the PMT-based detector of the apparatus with the detector of figure 7.4. The results are reported in a submitted article [94] and demonstrate that:

- the SiPM-based γ -ray detector can be used to substitute the PMT-based γ -ray detector, having satisfying performances in terms of energy and time resolution.
- A crystal material without self-activity is needed for this application, due to the low number of events. As example BGO should be suitable while LYSO can not be used due to the intrinsic background generated by the ^{176}Lu decay.

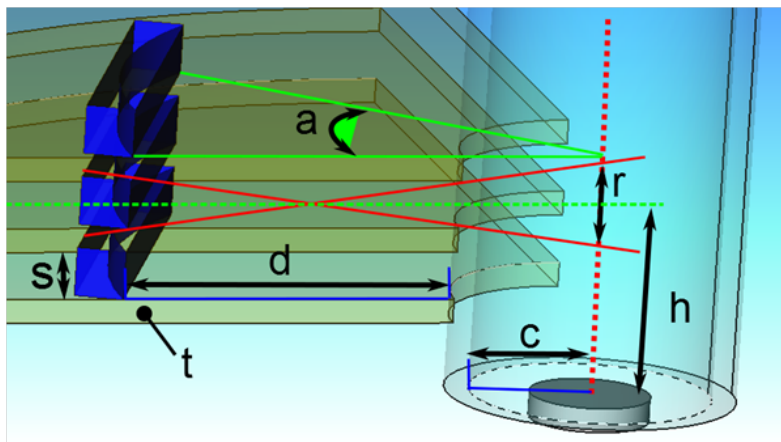


Figure 7.5: Main quantities used in the design procedure: (a) angle of view, (r) vertical resolution, (s) slit dimension, (t) thickness of the screen, (d) distance of detectors from the chamber wall, (c) chamber radius, (h) detector's ring height.

In figure 7.5 are sketched the main degrees of freedom in the design of a new multi-ring setup. Referring to the notation of the figure, the present apparatus, with only one ring of PMT-based detectors, presents the following characteristics: a slit (s) of 5 mm , a distance from the chamber wall (d) of 100 mm , a chamber radius (c) of 30 mm , a vertical resolution (r) of 8 mm and an angle of view (a) of 65° .

7.1 TOF Measurements

In order to explain which factors play the main role in the design of the setup, further details about the *o*-Ps TOF measurement have to be introduced. In a TOF measurement the detected *o*-Ps annihilations are much less frequent than annihilation of backscattered and re-emitted e^+ hitting the chamber walls, as depicted in figure 7.3.

In figure 7.6 a TOF spectrum measured with the present setup in a silicon oxide based porous sample, where *o*-Ps is formed in the porous bulk and emitted into vacuum (red curve), is compared to a background

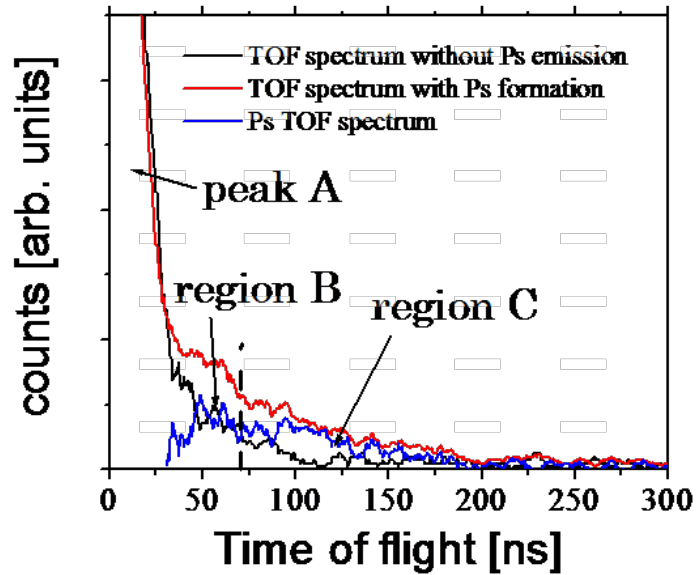


Figure 7.6: The raw *o*-Ps TOF spectrum (in blue) is obtained subtracting the background (in black) from the measured TOF spectra (in red), as it is measured at 10 *mm* above the sample surface. We can notice three features labeled with: A (prompt peak), B (region of the fast-hot *o*-Ps) and C (region of the slow-cold *o*-Ps).

TOF spectrum measured in a Si sample without *o-Ps* formation in the bulk (black curve). Both spectra were acquired at 10 *mm* of vertical height and with the same measuring time. The difference between the two spectra gives us the **TOF** spectrum of the emitted *o-Ps* (shown in blue in figure 7.6). The peak A, namely the prompt peak, is mainly due to the annihilation on the chamber walls of e^+ which are backscattered from the sample during implantation or re-emitted from the sample surface (see figure 7.3). The tail in the prompt peak, distinguishable between about 25 and 75 *ns*, is due to surface processes: (i) a small fraction of fast *o-Ps* is formed at the surface of the sample by backscattered and epithermal e^+ (see [95]); (ii) backscattered e^+ can undergo multi-reflection on the chamber walls giving delayed annihilations (see [95]); (iii) re-emitted epithermal e^+ annihilating on the chamber walls can also contribute. The tail is expected to be the same in porous and not-porous sample, because the surface is silicon oxide in both samples. Analysis of **TOF** spectra of emitted *o-Ps* are usually done transforming the time spectra in the corresponding energy spectra $N(E)$ (see [73] and [74] for details). The energy spectrum of the present measurement can be approximated by two Beam Maxwellian distributions [73, 74], each one expressed by the formula:

$$N(E) dE = A e^{-\frac{E}{k_B T}} dE$$

where A is a normalization factor, E is the *o-Ps* kinetic energy, k_B the Boltzmann constant and T is the *o-Ps* temperature. For the present spectrum, the temperatures of the two Maxwellian distributions result $T_B \sim 1430$ *K* and $T_C \sim 300$ *K*, respectively [74]. The number of hot-fast *o-Ps* events with $T_B \sim 1430$ *K* gives, for each bin, the highest contribution to the **TOF** spectrum in the region below about 70 *ns*. While the number of cold-slow *o-Ps* events with temperature $T_C \sim 300$ *K* becomes preponderant for each bin above 70 *ns*. Thus, for the purpose of the following

discussion, the TOF spectrum of the emitted o -Ps has been divided into two regions: a region B, below 70 ns, and a region C, above 70 ns, where the annihilations of fast-hot o -Ps and of cold-slow o -Ps, are predominant, respectively. In the design of the new multi-ring setup, we have to optimize the geometry of the system to minimize the acquisition time for region C maintaining a suitable signal to noise ratio for the region B. The noise on the TOF spectrum of emitted o -Ps is a poissonian noise that results from the subtraction of the background and measured TOF spectra. In the region B the signal to noise ratio is worse due to the presence of the prompt peak. As a matter of comparison, with the current setup and present samples the number of events of the background prompt peak is approximately 16 times bigger than the number of events in the region B. It is worth noting that decreasing the sample temperature [73] also the temperature of the two o -Ps distributions decreases. The region B and C, as well their boundary, shift to larger times, thus reducing the superimposition between the prompt peak and region B. As a consequence the signal to noise ratio in region B increases. On the basis of the previous considerations, two concurrent constraints have to be taken into account in the optimization procedure of the new setup:

- the first constraint is the velocity of the cold-slow o -Ps and its small amount. In a setup with several rings of detectors as depicted in figure 7.3, the velocity of the cold-slow o -Ps limits both the number of rings and the thickness of the shields between the rings. Due to the o -Ps lifetime of 142 ns and its slow velocity, rings of detectors placed too far from the sample are not exposed to a significant amount of survived o -Ps. Moreover, because of the little amount of cold-slow o -Ps, the detectors must be placed as close as possible to the axis of the camera to increase the field-of-view. The two effects become more important as the velocity of the cold-slow o -Ps atoms decreases, i.e.

as the sample temperature decreases.

- the second constraint comes from the number of the noisy events. As in the **PMT** setup, the thickness of the shields is $\sim 2\text{ cm}$, all the detected events are mainly originated by annihilations occurring in front of the slit. On the contrary, in the multi-ring setup, the reduction of the shield thickness, required by the first constraint, has two effects:
 - (i) it increases the poissonian noise in the region B because the e^+ backscattered annihilations, occurring at the chamber wall, are less shielded,
 - (ii) it causes false counts due to the detection of ***o*-Ps** that does not annihilate in front of the ring, i.e. cross-talk between the measurements of adjacent detectors, as occurs in common **γ -ray** cameras.
 Both (i) and (ii) act as a constraint tending to increase the thickness of the shields and to force the position of the detectors far away from the chamber walls. The poissonian noise (i) is more difficult to avoid due to the high ratio between the background prompt peak and the fast-hot ***o*-Ps** signal in the region B. Then (i) has been used to optimize the thickness of the shields and (ii) has been used to optimize the position of the detectors with respect to the chamber walls.

7.2 Figures of Merit

Three figures of merit have been introduced to discuss the performance of a system composed of different number of rings. The first figure of merit (M1) is used to evaluate the yield of the system respect to a reference by taking into account the first constraint described above. The second figure of merit (M2) is used to find the best shield thickness (t) minimizing the increase of the poissonian noise in the multi-ring setup (point (i) of the second constraint). Finally, the third figure of merit (M3) allows setting

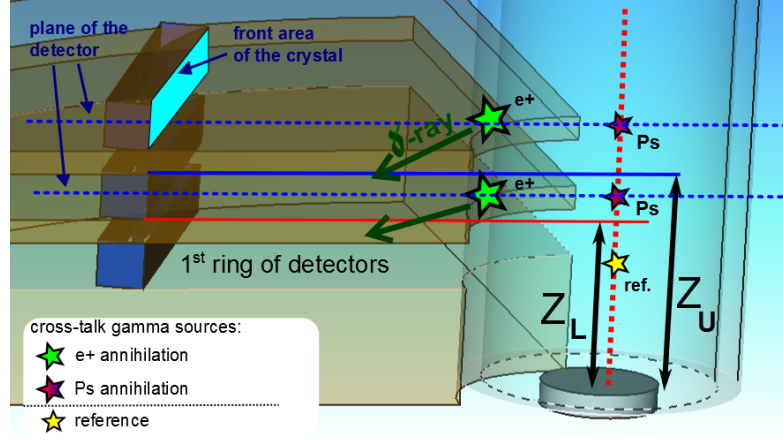


Figure 7.7: Quantities used in the formalization of the design procedure. Positions of the γ -rays point sources used in the Monte-Carlo simulations

the best value of the detector distance (d) by considering the cross-talk of adjacent detectors in detecting o -Ps (point (ii) of the second constraint). M1 is calculated taking into account the geometry of the setup and the o -Ps energy distribution. As previously introduced, the o -Ps energy distribution can be approximated by two Beam Maxwellian distributions, thus the velocity, v_{\perp} , of the o -Ps can be expressed as

$$\frac{1}{2}m_{Ps}v_{\perp}^2 = k_B T$$

where m_{Ps} is the o -Ps rest mass, that is equal to 2 times the electron rest mass. Using the velocity v_{\perp} , and assuming that the o -Ps is emitted perpendicular to the sample surface, the fraction of emitted o -Ps that reaches the lower edge of the ring of a given detector (Z_L in figure 7.7), of the ring of a given detector is $e^{\frac{Z_L}{v_{\perp}\tau}}$, where τ is the lifetime of o -Ps (142 ns). As well, the fraction of o -Ps reaching the upper edge Z_U is $e^{\frac{Z_U}{v_{\perp}\tau}}$. Then the fraction, F_1 of the emitted o -Ps that annihilates in the front of the detector can be approximately calculated with:

$$F_1 = e^{\frac{Z_L}{v_{\perp}\tau}} - e^{\frac{Z_U}{v_{\perp}\tau}} \quad (7.1)$$

The fraction, F_2 of *o*-Ps annihilation γ -rays that reach the crystals in the ring is proportional to the field-of-view of the ring. The field-of-view can be expressed as the ratio between two areas:

- the front area of the crystals in the detector rings and
- the area of the sphere, centered at the intersection between the chamber axis and the detector's plane, and with radius equal to the distance of the detector from the chamber axis.

The product $F_1 \cdot F_2$ proportional to the detected *o*-Ps atoms, has been used as a score to characterize the detection efficiency of different setups. The ratio between the score of a new SiPM-based setups and the score of a reference setup has been used as figure of merit, M1, to evaluate the improvement in performances. In order to quantify the number of noisy events, and consequently to calculate M2 and M3, a Monte-Carlo simulation routine, based on the open-source C++ library SLitrani [82] described in chapter 6, has been written. The routine starts generating γ -rays from γ -ray sources which are defined by the energy, by the coordinates in the setup, by the direction of emission and by the number of γ -rays emitted, namely the luminosity. Successively the routine follows the propagation of the γ -ray in the surrounding medium, calculating step by step the mean free path of the γ -rays basing on data from NIST [91], for the photoelectric effect, and Klein-Nishina formula for the Compton effect. Tungsten has been assumed as shield material while BGO has been assumed as crystal material. In order to obtain figures of merit, the number of noisy detected events has been normalized to the number of detected events generated by a reference 511 keV source. This reference source is placed at the same quota of the 1st ring of detectors and along the sample axis (reference annihilation star in figure 7.7) and it emits a bounce of collimated γ -rays rays in the direction of the first detector. The purpose of this source is to simulate

the *o*-Ps annihilations that occurs in front of the 1st ring of detector. The increment in the poissonian noise and the cross-talk, described in points (i) and (ii) of the second constraint, have been simulated by using point 511 keV γ -ray sources in the following way:

- in order to evaluate the increment of the poissonian noise with respect to **PMT** setup, we have to estimate the increment of the noisy events in the region B due to the worse shielding in the multi-ring setup. We remind that these noisy events arise mainly from a diffused annihilation of backscattered positrons on the chamber wall. Suppose to compare the noisy events detected by: a) the **PMT** with its 2 cm shield put in the same position of the 1st ring detector and b) the 1st ring detector in the multi-ring setup. For the 1st ring detector, the parts of chamber wall that are less effectively shielded, with respect to the **PMT**, are the ones that are in front of the 2nd , 3rd , 4th detector ring slits. This arises from the fact that the thick shield of the **PMT** setup has been substituted with the thin shields between the rings. The increment of the poissonian noise, due to the diffuse annihilation occurring in front of the 2nd , 3rd , 4th detector rings, have been simulated using point γ -ray sources placed at the center of the corresponding detector ring slit, along the chamber wall and collimated towards the detectors of the 1st ring (see figure 7.7). As previously evaluated by the analysis of the measurements of figure 7.6, the noisy events in the **PMT** are 16 times the signal of *o*-Ps (reference source). Therefore the luminosity of each source has been conservatively settled 20 times greater than the luminosity of the reference source. The sum of events generated from the sources placed in the front of 2nd , 3rd , 4th detector rings, and reveled by the detectors of the 1st ring, gives the increment of the noisy events. Therefore the normalization of this sum, with regard to the detected events coming from the reference source, gives the figure

of merit M2. The assumed hypotheses are very conservative because:
 -the noise due to the prompt peak on the region B is expected to decrease with the decreasing of the sample temperature, as previously described.

-with the choice of collimated point sources, we do not take into account the solid angle effect that would decrease the detected events as a function of the distance of the source from the detector.

- in order to study the cross-talk, produced by *o-Ps* annihilation between the adjacent rings of detectors, three sources have been placed at the height of the 2nd , 3rd , 4th detector rings and directed versus the 1st detector ring, as in the previous case, but set along the chamber axis. In this case the number of detected events have been normalized by using a source having equal luminosity to obtain the third figure of merit M3. It's worth reminding that the *o-Ps* annihilation emits γ -rays with energy below or equal to 511 keV , then the choice to simulate all the cross-talk events with sources of 511 keV is conservative.

As a rule of thumb a threshold of 5 % has been assumed in evaluating the three figures of merit, i.e:

-a change in the multi-ring setup that affects the value of M1 more than 5 % has been considered significant,

-a value of M2 and M3 less than 5 % has been considered as indicating a level of noisy events that does not affect significantly the measurements.

7.3 Discussion

In the design of *SiPM*-based setup a slit of 4 mm , a chamber radius (c in figure) of 10 mm and angle of view of 180° have been assumed. In the

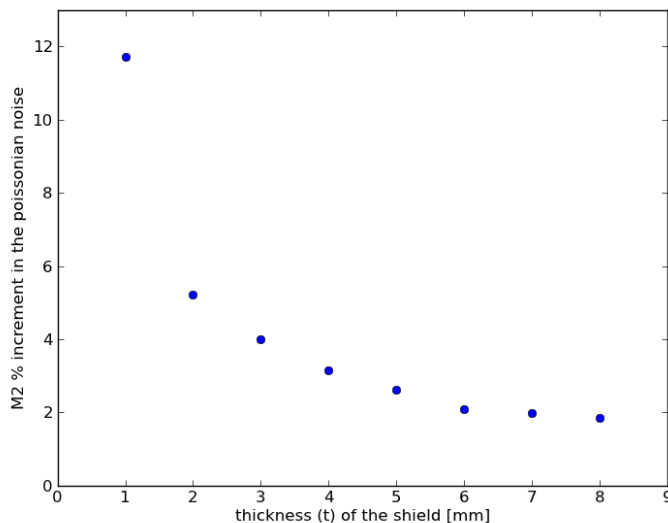


Figure 7.8: Figure of Merit M2 as a function of the screen thickness for a system composed by four rings of detectors. In the Monte-Carlo simulations the detectors have been placed at a distance of 100 *mm* from the chamber wall

following subsections we starts using the figure of merit M2 to optimize thickness of the shield (t) in order to mantain an acceptable signal to noise ratio in the measurement of region B (Ps with T 1430 K). Thi optimization is performed at 100 *mm* of distance from the chamber wall. Using the figure of merit M3 and assuming the optimized screen thickness, the distance of the detectors from the chamber wall is optimized in order to improve the number of events detected in the region C (*o*-Ps with T 300 K). In the end the figure of merit M1 is used to show how the number of detected events are influenced by the temperature cooling-down the sample.

7.3.1 Choice of the shield thickness

In order to find the minimum thickness of the absorber (t in figure 7.5), a first series of Monte-Carlo simulations has been done varying the thickness of the shields, assuming four rings of detectors and a distance (d) of the

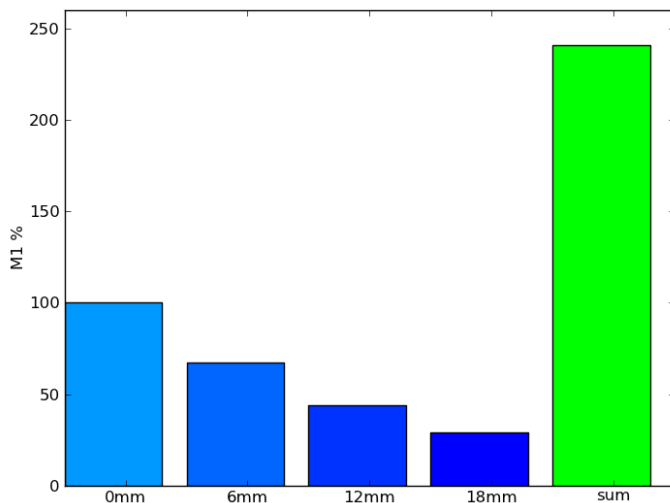


Figure 7.9: Figure of merit M1 assuming a shield thickness of 2 mm and a distance from the chamber wall of 100 mm . The temperature of the o -Ps assumed in the calculation of M1 is 1430 K . The reference setup has a single ring of detectors positioned at a distance (d) of 100 mm from the chamber wall, a slit (s) of 4 mm , a chamber radius (c) of 10 mm , covering a 180° angle of view.

detector ring from the chamber wall of 100 mm . In the graph of figure 7.8 the calculated values of M2 for different shields thickness have been reported. As result we can notice that a shield thickness of 2 mm is enough to satisfy the threshold of 5 % assumed for M2. The figure of merit M1 has been calculated assuming a shield thickness of 2 mm and a o -Ps velocity mean corresponding to a Ps distribution with a temperature of 1430 K . In the calculation of M1, the reference setup has been conceived as the present setup with PMT based detectors positioned at a distance (d) of 100 mm from the chamber wall, a slit (s) of 4 mm , a chamber radius (c) of 10 mm , covering a 180° angle of view.

The results have been reported, for each ring of detectors, in the form of histograms in figure 7.9. The rings of detector have been labeled in figure 7.9 with the vertical positions of their mid point. The 1st ring of detectors is

placed at the same vertical position of the reference detector. M1 decreases, from the 100 % value, with the increase of the vertical position because of the lower number of annihilation present at a higher distance from the sample. The cumulative figure of merit of a setup composed by the first 4 ring of detectors is also reported. As can be noticed, a setup composed by four rings of detectors has a figure of merit M1 of about 240 %.

7.3.2 Distance from the chamber wall

The advantage in using the SiPM-based multi-ring detector is even greater if the experiment is only devoted to the study of the cold-slow fraction of the *o*-Ps emission in the region C. In this case the ring of detectors, differently from PMT, can be placed closer to the chamber walls thanks to the compactness of the SiPM-based detectors. This new configuration clearly worsen the noisy in the region B. Being the region C of the TOF spectra outside the prompt peak, the noisy events are due to the cross-talk as valued by the figure of merit M3.

In the graph of figure 7.10 the resulting values of M3, varying the distance (d) from the chamber wall, have been reported. From figure 7.10 we can notice that a distance of 40 *mm* from the chamber wall is enough to guarantee a value of M3 lower than the threshold of 5 %.

In the histograms of figure 7.11, the values of M1 were re-calculated for each ring of detectors re-placed at $d = 40$ *mm* considering the cold part of the spectrum, i.e. a *o*-Ps velocity corresponding to a *o*-Ps distribution with a temperature of $T = 300$ *K* . The reference set-up was kept at 100 *mm* distance from the chamber wall, in order to quantify the advantages of approaching the ring-detectors to the chamber wall. The sum of the M1 values (363 %) of the series is reported in the last bar of the histogram on the right. The vertical resolution, (r) in figure 7.5, at $d = 40$ *mm* is 6 *mm* and it equals the vertical distance between the mid positions of two

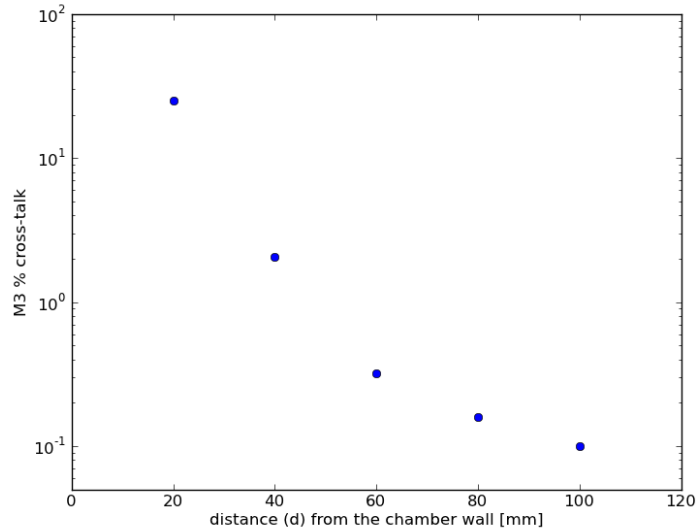


Figure 7.10: Figure of merit M3 as a function of the distance from the chamber wall for a system composed by four ring of detectors. In the Monte-Carlo simulations the thickness of the shield has been settled to 2 *mm* .

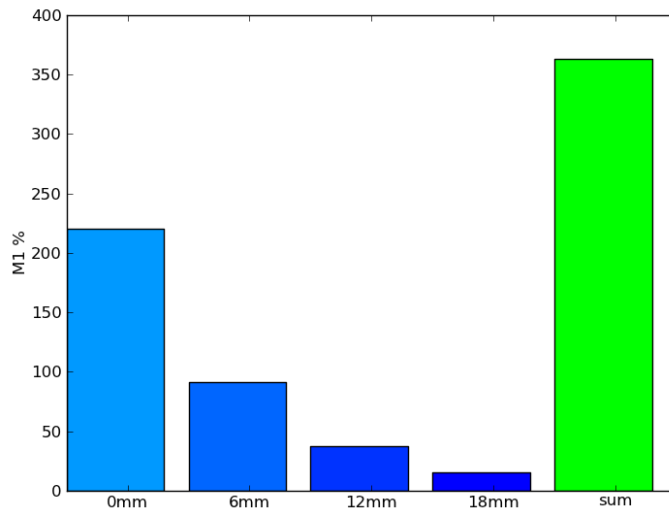


Figure 7.11: Figure of merit M1 assuming a shield thickness of 2 *mm* and a distance from the chamber wall of 40 *mm* . The temperature of the *o*-Ps is 300 *K* . The reference setup has a single ring of detectors positioned at a distance (d) of 100 *mm* from the chamber wall, a slit (s) of 4 *mm* , a chamber radius (c) of 10 *mm* , covering a 180° angle of view.

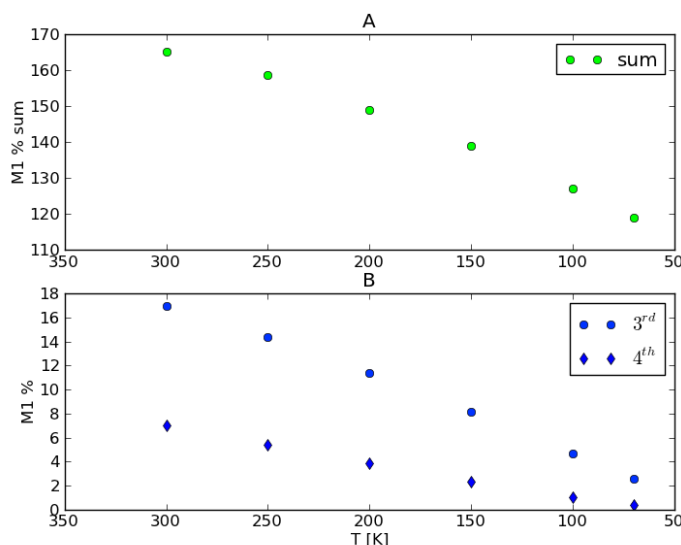


Figure 7.12: A: Figure of merit M1 of a four multi-ring detector at different cold temperatures with respect to the single ring. Both setups have detectors positioned at a distance (d) of 40 mm from the chamber wall, a slit (s) of 4 mm, a chamber radius (c) of 10 mm. B: Contributions of the farthest detectors to the sum of figure A.

adjacent detector rings.

7.3.3 Temperature of the sample

To estimate the effectiveness of the multi-ring approach in measuring *o*-Ps TOF with the sample at different temperatures, the values of M1 can be calculated for each detector ring using as reference the 1st ring of detectors. In this case, the sum of M1 give the overall increment in the detected events of the multi-rings with respect to the detected events of the 1st ring. The rings, as above, are positioned at a distance (d) of 40 mm from the chamber wall, with a slit (s) of 4 mm, a chamber radius (c) of 10 mm, and covering a 180° angle of view.

In figure 7.12-A the sum of M1 values report has been reported. As can be noticed, the cumulative M1 value is 160 % at 300 K and decreases to 120 % at 70 K. Decreasing the sample temperature, the velocity of the

thermalized Ps also decreases. In this case very few *o*-Ps atoms annihilate in front of the farthest rings. The contribution of the farthest two rings of detectors to the sum of Fig. 7.12-A is reported separately in figure 7.12-B. This figure shows the sample temperature at which the use of these rings is unsuitable. With the threshold of 5 %, the 3rd ring of detectors is not useful for temperature below 100 K while the 4th ring for temperatures below 250 K . As shown, an optimized multi-ring set up allows for an improvement in the performances of a TOF apparatus. In particular if the above results are scaled for the present Trento TOF setup, with a different chamber radius (c) and angle of view (a), the total counting rate is found to increase 600 % for the cold-slow *o*-Ps. Moreover the vertical resolution (r) of the multi-ring set up is 1.3 times better.

7.4 Conclusions

In this chapter the performances in *o*-Ps TOF experiments of a γ -ray detector composed of a LYSO scintillator and two SiPMs, has been analyzed. The results were compared with those obtained with a standard detector, consisting in an NaI:Tl scintillator coupled to a PMT. The main advantage in using SiPMs is in the possibility to use small 4x4 mm² scintillators which can be put directly inside the shields, making possible to easily optimize the design of a multi-ring detector. It was shown that a four rings detector can be designed taking into account the noisy events in order to find the minimum thickness of the shields and the optimum distance from the chamber wall. The multi-ring approach increases the counting rate allowing at the same time to achieve a better spatial resolution.

Chapter 8

Conclusions

In this thesis the main topics that have been discussed are: (i) the use of **SiPM**-based detectors in an apparatus for **TOF** of **Ps**, (ii) the use of a prototype detector for fluorescence lifetime time-gated spectroscopy in a micro-reactor array for fluorescence markers-based bio-affinity assay. Both the two discussions are based on Monte-Carlo simulations that have been carried out using direct ray-tracers.

In the first case the constraints have been defined taking into account the experimental data acquired with current **PMT**-based setup. In particular both the effect of poissonian noise and cross-talk have been estimated in the discussion. It has been shown that the use of the **SiPM**-based detectors simplify the placement of the detectors and permits to build adaptable geometries. The adaptable configuration should permit to increase up to six times the acquisition speed in the experiment with respect of the actual setup. This increment, which is extrapolated in chapter 7, is fundamental to carry on requested experiences at cold temperature of the sample. The detectors have been conceived as built using **SiPMs**, having area $4 \times 4 \text{ mm}^2$, coupled to scintillator with length 30 mm . The light transport in this kind of detector has been simulated in chapter 5, with particular emphasis on the importance of angular distributions of light at interfaces. The reported

method used in these simulations permits to adapt the **PDE**, which is measured with collimated light sources, to non collimated light sources.

The deployment of the **NPD** detector in a micro-reactor array for fluorescence markers-based bio-affinity assays has been discussed in chapter 3. In this case the constraints have been defined starting from the geometries of the septa in the fluidic layer that are realizable in **PDMS**. The cross-talk between adjacent detectors has been evaluated to reach promising geometries of the 2D array grid and of the septa. In chapter 2 the **NPD** detector has been characterized and it has been shown that it is well suited for lab-on-chip applications. Its points of strength are the high **FF** and its low data-throughput. Moreover it has been shown that the drawbacks, that are expected for **CMOS SPAD** arrays (the **DCR** and the optical cross-talk), could be mitigated in this detector by disabling the noisiest **SPADs** in the array.

Finally, thanks to its high **FF**, it has been possible to use the **NPD** detector in a proof-of-concept experiment that was aimed to a first evaluation of the $0.35 \mu\text{m}$ **HV CMOS** technology for **γ -ray** detection. In this proof-of-concept an **NPD** detector and a **SiPM** have been coupled to the same **LYSO** crystal. Due to the small area of the **NPD** detector it was not possible to perform a complete characterization. Despite this limitation, by normalizing to the relative areas of the two devices, we were able to observe that the two technologies exhibit similar sensitivity.

8.1 Future Perspectives

In the first overview of section 1.1 a list of challenging applications that can be faced by silicon single-photon sensors has been presented. The list has been compiled requiring that the chosen application is related to **γ -ray** or Fluorescence Lifetime spectroscopies. Many of these applications

are hot-topics in research and thus it is not hard to foresee that the use of silicon single photon sensors, thanks to their small cost, simplicity in the management and their high degree of customization, will become commonly used in the near future. If the discussion is broadened to other fields, the set of photon starved applications, that can be dealt with the use of silicon single-photon sensors, is nowadays expanding so rapidly that becomes difficult to draw its boundaries. The problems that have to be faced at the boundaries of this expansion are related to the high number of different expertises needed in the design of new apparatus. Moreover the design of single photon apparatus are complicated by the fact that signal-to-noise ratio has to be carefully considered in formalizing the constraints of the design procedure. System models are able to take in account many aspects of the measurements and act as workbenches when different experts discuss new photon-starved applications. For these reasons, simulations and discussions similar to the ones presented in this thesis, are increasingly used.

Aknoledgements

I am grateful to Gian-Franco and David for their guidance, encouragements and friendship. I would like to express my gratitude to Lucio Pancheri, Marina Popleteeva, Laura Pasquardin, Lorenzo Lunelli, Gabriele Giacomini, Alessandro Tarolli, Claudio Piemonte, Elisabetta Mazzuca, Sebastiano Mariazzi, Lea Di Noto, Marco Bettonte and Roberto Brusa. They have assisted me, guided and inspired.

Bibliography

- [1] M. D. Eisaman et al. “Single-Photon sources and detectors”. In: *Review of Scientific Instruments* 82 (July 2011). DOI: [10.1063/1.3610677](https://doi.org/10.1063/1.3610677).
- [2] R. Hadfield. “Single-photon detectors for optical quantum information applications”. In: *Nature Photonics* 3 (2009), pp. 696–705. DOI: [10.1038/nphoton.2009.230](https://doi.org/10.1038/nphoton.2009.230).
- [3] *Selection Guide by Application*. Hamamatsu Photonics K.K. URL: http://jp.hamamatsu.com/resources/products/etd/pdf/PMT_16-21_e.pdf.
- [4] Steven A. Soper, Quincy L. Mattingly, and Pradeep Vegunta. “Photon Burst Detection of Single Near-Infrared Fluorescent Molecules”. In: *Analytical Chemistry* 65.6 (Mar. 1993), pp. 740–747.
- [5] X. Michalet et al. “Single-quantum dot imaging with a photon counting camera”. In: *Current Pharmaceutical Biotechnology* 10.5 (Aug. 2009), pp. 543–558.
- [6] Th Förtscher. “Zwischenmolekulare Energiewanderung und Fluoreszenz”. In: *Annalen der Physik* 437.1-2 (1948), pp. 55–75. DOI: [10.1002/andp.19484370105](https://doi.org/10.1002/andp.19484370105).
- [7] M. Peter and s.M Aweer-Beg. “Imaging molecular interactions by multiphoton flim”. In: *Biology of the Cell* 96 (2004), pp. 231–234. DOI: [10.1016/j.biolcel.2003.12.006](https://doi.org/10.1016/j.biolcel.2003.12.006).
- [8] Nils G. Walter et al. “Do-it-yourself guide: How to use the modern single molecule toolkit”. In: *Nature Methods* 5.6 (June 2008), pp. 475–489. DOI: [10.1038/nmeth.1215](https://doi.org/10.1038/nmeth.1215).
- [9] I. Nissinen et al. “A Sub-ns Time-gated CMOS Single Photon Avalanche Diode Detector for Raman Spectroscopy”. In: *Proceedings of IEEE European Solid State Device Conference 2011* (2011), pp. 375–378. DOI: [10.1109/ESSDERC.2011.6044156](https://doi.org/10.1109/ESSDERC.2011.6044156).

- [10] Vasilis Ntziachristos and Britton Chance. “Breast imaging technology: Probing physiology and molecular function using optical imaging”. In: *Breast Cancer Research* 3 (2000), pp. 41–46. DOI: [10.1186/bcr269](https://doi.org/10.1186/bcr269).
- [11] Antonio Pifferi et al. “Time-Resolved Diffuse Reflectance Using Small Source-Detector Separation and Fast Single-Photon gating”. In: *Physical Review Letters* 100.13 (2008), p. 138101. DOI: [10.1103/PhysRevLett.100.138101](https://doi.org/10.1103/PhysRevLett.100.138101).
- [12] R.P. Ekins and F.W. Chu. “Multianalyte Microspot Immunoassay - Microanalytical Compact Disc of the Future”. In: *Clinical Chemistry* 37.11 (1991).
- [13] Marta Bally et al. “Optical microarray biosensing techniques”. In: *Surface and interface Analysis* 38 (2006), pp. 1442–1458. DOI: [10.1002/sia.2375](https://doi.org/10.1002/sia.2375).
- [14] Bruce R. Rae et al. “A CMOS Time-Resolved Fluorescence Lifetime Analysis Micro-System”. In: *Sensors* 9 (2009), pp. 9255–9274. DOI: [10.3390/s91109255](https://doi.org/10.3390/s91109255).
- [15] S.R. Cherry and M. Dahlbom. *PET: Physics, instrumentation, and scanners*. New York: Springer, 2004.
- [16] C.S. Levin and E.J. Hoffman. “Calculation of positron range and its effect on the fundamental limit of positron emission tomography system spatial resolution”. In: *Physics in medicine and biology* 44 (1999), p. 781.
- [17] J.V. Jelley. “Cerenkov radiation and its applications”. In: *British Journal of Applied Physics* 6 (1955), p. 227.
- [18] R. Robertson et al. “Optical imaging of Cerenkov light generation from positron-emitting radiotracers”. In: *Physics in medicine and biology* 54 (2009), N355.
- [19] A.E. Spinelli et al. “Cerenkov radiation allows in vivo optical imaging of positron emitting radiotracers”. In: *Physics in medicine and biology* 55 (2010), p. 483.
- [20] G.S. Mitchell et al. “In vivo Cerenkov luminescence imaging: a new tool for molecular imaging”. In: *Philosophical Transactions of the Royal Society A: Mathematical, Physical and Engineering Sciences* 369.1955 (2011), pp. 4605–4619.
- [21] *KM3NeT Technical Design Report for a Deep-Sea Research Infrastructure in the Mediterranean Sea Incorporating a Very Large Volume Neutrino Telescope*. Tech. rep. KM3Net consortium, 2011.
- [22] *KM3Net web page: <http://www.km3net.org>*. URL: <http://www.km3net.org>.
- [23] D. Stoppa and A. Simoni. “Single-Photon Detectors for Time-of-Flight Range Imaging”. In: *Single-Photon Imaging* (2011), pp. 275–300.

- [24] Andreas Velten et al. “Recovering three-dimensional shape around a corner using ultrafast time-of-flight imaging”. In: *Nature Communications* 3.745 (Mar. 2012). DOI: [doi:10.1038/ncomms1747](https://doi.org/10.1038/ncomms1747).
- [25] B.K. Lubsandorzhev. “On the history of photomultiplier tube invention”. In: *Nuclear Instruments and Methods in Physics Research A* 567.1 (Nov. 2006), pp. 236–238. DOI: [10.1016/j.nima.2006.05.221](https://doi.org/10.1016/j.nima.2006.05.221).
- [26] *Photomultiplier Handbook*. Burle Industries Inc. 1980.
- [27] G. Ambrosi et al. “Time resolving characteristics of HPK and FBK silicon photomultipliers for TOF and PET applications”. In: *Nuclear Instruments and Methods in Physics Research Section A* 617.1-3 (2010), pp. 242–243.
- [28] D. Renker. “Photosensors”. In: *Nuclear Instruments and Methods in Physics Research A* 527 (2004), pp. 15–20. DOI: [10.1016/j.nima.2004.03.010](https://doi.org/10.1016/j.nima.2004.03.010).
- [29] D. Gajanana et al. “A front end ASIC for the readout of the PMT in the KM3NeT detector”. In: *Proceedings of Topical Workshop On Electronics For Particle Physics 2010* (Sept. 2010). DOI: [10.1088/1748-0221/5/12/C12040](https://doi.org/10.1088/1748-0221/5/12/C12040).
- [30] M. Akatsu et al. “MCP-PMT timing property for single photons”. In: *Nuclear Instruments and Methods in Physics Research A* 528.11 (Aug. 2004). DOI: [10.1016/j.nima.2004.04.207](https://doi.org/10.1016/j.nima.2004.04.207).
- [31] *Hamamatsu Catalog: High-Speed Gated Image Intensifier Units*. Hamamatsu Photonics K.K. July 2009.
- [32] R. Cubeddu et al. “Time Resolved Fluorescence Imaging in Biology and Medicine”. In: *Journal of Physics D: Applied Physics* 35.9 (2002), R61. DOI: [10.1088/0022-3727/35/9/201](https://doi.org/10.1088/0022-3727/35/9/201).
- [33] *Hamamatsu Catalog: Gated ICCD Camera Series*. Hamamatsu Photonics K.K. 2008.
- [34] RJ McIntyre. “Theory of microplasma instability in silicon”. In: *Journal of Applied Physics* 32.6 (1961), pp. 983–995.
- [35] R.H. Haitz. “Mechanisms contributing to the noise pulse rate of avalanche diodes”. In: *Journal of Applied Physics* 36.10 (1965), pp. 3123–3131.
- [36] Sergio Cova et al. “Avalanche Photodiodes and Quenching Circuits for Single-Photon Detection”. In: *Applied Optics* 35.12 (1996). DOI: [10.1364/AO.35.001956](https://doi.org/10.1364/AO.35.001956).
- [37] Gian-Franco Dalla Betta et al. “Avalanche Photodiodes in Submicron CMOS Technologies for High-Sensitivity Imaging”. In: *Advances in Photodiodes*. InTech, Mar. 2011. Chap. 11.

- [38] C. D’Ambrosio and H. Leutz. “Hybrid Photon Detectors”. In: *Nuclear Instruments and Methods in Physics Research A* 501 (2003), pp. 463–498. DOI: [10.1016/S0168-9002\(03\)00431-5](https://doi.org/10.1016/S0168-9002(03)00431-5).
- [39] T. Tick et al. “Status of the Timepix MCP-HPD development”. In: *Proceedings of Topical Workshop On Electronics For Particle Physics 2010* (Sept. 2010). DOI: [10.1088/1748-0221/5/12/C12020](https://doi.org/10.1088/1748-0221/5/12/C12020).
- [40] D. Renker. “Geiger-mode avalanche photodiodes, history, properties and problems”. In: *Nuclear Instruments and Methods in Physics Research Section A: Accelerators, Spectrometers, Detectors and Associated Equipment* 567.1 (2006), pp. 48–56.
- [41] V. Saveliev. “The recent development and study of silicon photomultiplier”. In: *Nuclear Instruments and Methods in Physics Research Section A: Accelerators, Spectrometers, Detectors and Associated Equipment* 535.1 (2004), pp. 528–532.
- [42] C. Piemonte et al. “Characterization of the first prototypes of silicon photomultiplier fabricated at ITC-irst”. In: *Nuclear Science, IEEE Transactions on* 54.1 (2007), pp. 236–244.
- [43] G. Collazuol et al. “Single photon timing resolution and detection efficiency of the IRST silicon photo-multipliers”. In: *Nuclear Instruments and Methods in Physics Research Section A: Accelerators, Spectrometers, Detectors and Associated Equipment* 581.1-2 (2007), pp. 461–464.
- [44] G. Llosá et al. “Novel silicon photomultipliers for PET applications”. In: *Nuclear Science, IEEE Transactions on* 55.3 (2008), pp. 877–881.
- [45] A. Rochas et al. “Single photon detector fabricated in a complementary metal–oxide–semiconductor high-voltage technology”. In: *Review of scientific instruments* 74 (2003), p. 3263.
- [46] A. Rochas et al. “First fully integrated 2-D array of single-photon detectors in standard CMOS technology”. In: *Photonics Technology Letters, IEEE* 15.7 (2003), pp. 963–965.
- [47] L. Pancheri and D. Stoppa. “Low-noise CMOS single-photon avalanche diodes with 32 ns dead time”. In: *Solid State Device Research Conference, 2007. ESSDERC 2007. 37th European*. IEEE. 2007, pp. 362–365.
- [48] H. Finkelstein, M.J. Hsu, and S.C. Esener. “STI-bounded single-photon avalanche diode in a deep-submicrometer CMOS technology”. In: *Electron Device Letters, IEEE* 27.11 (2006), pp. 887–889.

- [49] C. Niclass et al. “A single photon avalanche diode implemented in 130-nm CMOS technology”. In: *Selected Topics in Quantum Electronics, IEEE Journal of* 13.4 (2007), pp. 863–869.
- [50] M. Gersbach et al. “A single photon detector implemented in a 130nm cmos imaging process”. In: *Solid-State Device Research Conference, 2008. ESSDERC 2008. 38th European*. IEEE. 2008, pp. 270–273.
- [51] M. Gersbach et al. “A low-noise single-photon detector implemented in a 130 nm CMOS imaging process”. In: *Solid-State Electronics* 53.7 (2009), pp. 803–808.
- [52] J.A. Richardson, L.A. Grant, and R.K. Henderson. “Low dark count single-photon avalanche diode structure compatible with standard nanometer scale CMOS technology”. In: *Photonics Technology Letters, IEEE* 21.14 (2009), pp. 1020–1022.
- [53] M. Gersbach et al. “A parallel 32×32 time-to-digital converter array fabricated in a 130 nm imaging CMOS technology”. In: *ESSCIRC, 2009. ESSCIRC'09. Proceedings of*. IEEE. 2009, pp. 196–199.
- [54] D. Stoppa et al. “A 32×32 -pixel array with in-pixel photon counting and arrival time measurement in the analog domain”. In: *ESSCIRC, 2009. ESSCIRC'09. Proceedings of*. Ieee. 2009, pp. 204–207.
- [55] J. Richardson et al. “A 32×32 50ps resolution 10 bit time to digital converter array in 130nm CMOS for time correlated imaging”. In: *Custom Integrated Circuits Conference, 2009. CICC'09. IEEE*. IEEE. 2009, pp. 77–80.
- [56] L. Pancheri and D. Stoppa. “A SPAD-based pixel linear array for high-speed time-gated fluorescence lifetime imaging”. In: *ESSCIRC, 2009. ESSCIRC'09. Proceedings of*. Ieee. 2009, pp. 428–431.
- [57] David Eric Schwartz, Ping Gong, and Kenneth L. Shepard. “Time Resolved Förster-resonance-energy-transfer DNA assay on an active CMOS microarray”. In: *Biosensors and Bioelectronics* 24 (2008), pp. 383–390. DOI: [10.1016/j.bios.2008.04.015](https://doi.org/10.1016/j.bios.2008.04.015).
- [58] David Eric Schwartz, Edoardo Charbon, and Kenneth L. Shepard. “A Single-Photon Avalanche Diode Array for Fluorescence Lifetime Imaging Microscopy”. In: *IEEE Journal of Solid-State Circuits* 43.11 (Nov. 2008). DOI: [10.1109/JSSC.2008.2005818](https://doi.org/10.1109/JSSC.2008.2005818).

- [59] Cristiano Niclass et al. “A 128x128 Single-Photon Image Sensor with Column-Level 10-bit Time-to-Digital Converter Array”. In: *IEEE Journal of Solid-State Circuits* 43.12 (2008), pp. 2977–2989.
- [60] Gerard Giraud et al. “Fluorescence lifetime biosensing with DNA microarrays and a CMOS-SPAD imager”. In: *BIOMEDICAL OPTICS EXPRESS* 1.5 (Dec. 2010). Demonstration of rapid TCSPC data acquisition for fluorescence lifetime imaging and multiplexing of a DNA microarray using a CMOS-SPAD array camera, p. 1302.
- [61] Chockalingam Veerappan et al. “A 160x128 Single-Photon Image Sensor with On-Pixel 55ps 10b Time-to-Digital Converter”. In: *International Solid State Circuits Conference 2011* (2011), pp. 312–313.
- [62] H. C. Gerritsen et al. “Fluorescence lifetime imaging in scanning microscopes: acquisition speed, photon economy and lifetime resolution”. In: *Journal of Microscopy* 206.3 (June 2002), pp. 218–224.
- [63] Day-Uei Li et al. “Hardware implementation algorithm and error analysis of high-speed fluorescence lifetime sensing system using center-of-mass method”. In: *Journal of Biomedical Optics* 15.1 (Feb. 2010), p. 017006. DOI: [10.1117/1.3309737](https://doi.org/10.1117/1.3309737).
- [64] Thomas Frach et al. “The Digital Silicon Photomultiplier-Principle of Operation and Intrinsic Detector Performance”. In: *Proceedings of IEEE Nuclear Science Symposium Conference Record 2009* (2009), pp. 1959–1965.
- [65] T.K. Lewellen. “Recent developments in PET detector technology”. In: *Physics in medicine and biology* 53 (2008), R287.
- [66] J. Trummer et al. “Scintillation properties of LuYAP and LYSO crystals measured with MiniACCOS, an automatic crystal quality control system”. In: *Nuclear Science Symposium Conference Record, 2005 IEEE*. Vol. 5. IEEE. 2005, pp. 2807–2810.
- [67] P. Beltrame et al. “AX-PET: Concept, Proof of Principle and First Results with Phantoms”. In: *IEEE Nuclear Science Symposium Conference Record* (2010). AX-PET presentation. A collaborative effort to build a parallax free PET using LYSO long crystals and WLS coupled to Hamamatsu SiPM, pp. 2754–2757.
- [68] E. Bolle et al. “COMPET – high resolution and high sensitivity PET scanner with novel readout concept: Setup and simulations”. In: *Nuclear Instruments and Methods in Physics Research A* 648 (2011). Description of a geometrical new arrangement of crystal for PET following ax-PET results and axial pet concepts, S93–S95. DOI: [10.1016/j.nima.2010.12.097](https://doi.org/10.1016/j.nima.2010.12.097).

- [69] C. Casella. *Ax-PET: Demonstration of a novel PET concept*. Detector seminar held at CERN , March 2012. Slides available on internet. URL: <http://indico.cern.ch/conferenceDisplay.py?confId=175430>.
- [70] S. Berko and H. N. Pendleton. “Positronium”. In: *Annual Review of Nuclear and Particle Science* 30 (1980), p. 543.
- [71] M. Charlton. “Antihydrogen production in collisions of antiprotons with excited states of positronium”. In: *Physics Letters A* 143.3 (Jan. 1990). DOI: [10.1016/0375-9601\(90\)90665-B](https://doi.org/10.1016/0375-9601(90)90665-B).
- [72] A. Kellerbauer et al. “Proposed antimatter gravity measurements with an antihydrogen beam”. In: *Nuclear Instruments and Methods in Physics Research B* 266 (2008), pp. 351–356. DOI: [10.1016/j.nimb.2007.12.010](https://doi.org/10.1016/j.nimb.2007.12.010).
- [73] S. Mariuzzi, P. Bettotti, and R.S. Brusa. “Positronium Cooling and Emission in Vacuum from Nanochannels at Cryogenic Temperature”. In: *Physical review letters* 104.24 (2010), p. 243401.
- [74] Lea Di Noto et al. “Time of Flight system to investigate Positronium Cooling”. In: *European Physical Journal* (2012). DOI: [10.1140/epjd/e2012-20674-7](https://doi.org/10.1140/epjd/e2012-20674-7).
- [75] Y. Nagai. “Origins of positronium emitted from SiO₂”. In: (1998).
- [76] *ZTEC 4211 digital oscilloscope*. ZTEC Instruments, Inc. URL: http://www.ztecinstruments.com/products/oscilloscopes/ZT4211-01_PXI/.
- [77] Rene Brun and Fons Rademakers. “ROOT - An Object Oriented Data Analysis Framework”. In: *Nuclear Instruments and Methods in Physics Research A* (1997), pp. 81–86. URL: <http://root.cern.ch>.
- [78] N. Metropolis. “The beginning of the Monte Carlo method”. In: *Los Alamos Science* 15.584 (1987), pp. 125–130.
- [79] Ivan Rech et al. “Optical crosstalk in single photon avalanche diode arrays: a new complete model”. In: *Optics Express* 16.12 (June 2008), p. 8381.
- [80] Ivan Rech et al. “A New Approach to optical Crosstalk Modeling in Single-Photon Avalanche Diodes”. In: *IEEE Photonics Technology Letters* 20.5 (Mar. 2008). DOI: [10.1109/LPT.2007.915654](https://doi.org/10.1109/LPT.2007.915654).
- [81] Joseph R. Lakowicz. *Principles of Fluorescence Spectroscopy, 3rd edition*. Springer, 2006.

- [82] Francois-Xavier Gentit. “Litrani: a general purpose Monte-Carlo program simulating light propagation in isotropic or anisotropic media”. In: *Nuclear Instruments and Methods in Physics Research A* 486 (2002). The paper of F.-X. Gentit that has to be cited for each SLitrani pub., pp. 35–39. DOI: [10.1016/S0168-9002\(02\)00671-X](https://doi.org/10.1016/S0168-9002(02)00671-X). URL: [./cloud001/Gentit2002.pdf](http://cloud001/Gentit2002.pdf).
- [83] H.P. Lehr, A. Brandenburg, and G. Sulz. “Modeling and experimental verification of the performance of TIRF-sensing systems for oligonucleotide microarrays based on bulk and integrated optical planar waveguides”. In: *Sensors and Actuators B: Chemical* 92.3 (2003), pp. 303–314.
- [84] P. Liaparinos et al. “Evaluating the radiation detection of the RbGd₂Br₇: Ce scintillator by Monte Carlo methods”. In: *Nuclear Instruments and Methods in Physics Research Section A* 569.2 (2006), pp. 355–358.
- [85] D. Wahl, V. B. Mikhailik, and H. Kraus. “The monte-carlo refractive index matching technique for determining the input parameters for simulation of the light collection in scintillating crystals”. In: *Nuclear Instruments and Methods in Physics Research A* 570 (2007). Article that explains the use and the origins of the diffusion length implemented in the TLitMedium class of SLitrani., pp. 529–535. DOI: [10.1016/j.nima.2006.10.099](https://doi.org/10.1016/j.nima.2006.10.099).
- [86] E. Lorincz et al. “Modeling and Optimization of Scintillator Arrays for PET Detectors”. In: *Nuclear Science, IEEE Transactions on* 57.1 (2010), pp. 48–54. DOI: [10.1109/TNS.2009.2038215](https://doi.org/10.1109/TNS.2009.2038215).
- [87] U. Heinrichs et al. “Statistical studies on the light output and energy resolution of small LSO single crystals with different surface treatments combined with various reflector materials”. In: *Nuclear Instruments and Methods in Physics Research Section A: Accelerators, Spectrometers, Detectors and Associated Equipment* 486.1 (2002), pp. 60–66.
- [88] Fernando Tommasini and Alberto Morgante. *Correnti, Radiazione e Quanti. Introduzione all'Elettromagnetismo, alla Relativita Ristretta a e all'Ottica moderna*. Mar. 2007.
- [89] Bruno Benedetto Rossi. *High Energy Particles*. Englewood Cliffs, N.J.: Prentice-Hall, 1965.
- [90] F. Arqueros and G. D. Montesinos. “A simple algorithm for the transport of gamma rays in a medium”. In: *American Journal of Physics* 71.1 (Jan. 2003). The model for cross section interaction implemented in TlitGamma. DOI: [10.1119/1.1509416](https://doi.org/10.1119/1.1509416).

-
- [91] M.J. Berger et al. *XCOM: Photon Cross Section Database*. [Online] Available: <http://physics.nist.gov/xcom>. National Institute of Standards and Technology, Gaithersburg, MD. (version 1.5). 2010. URL: <http://www.nist.gov/pml/data/xcom/index.cfm>.
- [92] S. Agostinelli et al. “GEANT4: a simulation toolkit”. In: *Nuclear Instruments and Methods in Physics Research Section A: Accelerators, Spectrometers, Detectors and Associated Equipment* 506.3 (2003), pp. 250–303.
- [93] Norman Uhlmann et al. “Design and material considerations for a 3D-position sensitive scintillation detector as absorber for a high resolution Compton-Camera”. In: *IEEE Nuclear Science Symposium Conference Record* (2003). Study of the deposited energy in a compton scatter scintillator-based camera., pp. CC1–CC4.
- [94] Elisabetta Mazzuca et al. “Compact gamma detectors based on FBK SiPMs for a Ps Time Of Flight apparatus”. Submitted to *Journal of Instrumentation*. 2012.
- [95] R. S. Brusa and A. Dupasquier. *Physics with many Positrons*. Vol. 174. Proceedings of the International School of Physics ”Enrico Fermi”. IOS Press, 2010. ISBN: ISBN 978-1-60750-646-1.

List of Tables

1.1	Examples of commercial available single-photon detectors .	13
4.1	Measurement of uncertainty in the positioning	48
4.2	Experimental results of CMOS SPAD vs SiPM in detecting gamma events.	56
5.1	Calculated values for light output at different refraction index coefficients. In the first half light output for teflon coating are tabulated, in the second half data for mirror coating are reported	73

List of Figures

1.1	A <i>ps</i> Laser diode (p) is used to excite the fluorophore (f). The fluorescent emission (l) is collected by the detector (d) through two different sampling time windows (w) to calculate the light emission decay time (dt), namely the Lifetime, of the fluorophore (f).	19
1.2	PET detector	20
1.3	A bounce of e^+ is linear accelerated towards a cooled porous sample of Silicon. Hitting the surface of the sample, the bounce of e^+ produced a cloud of scattered e^- (1), that is revealed by a ChannelTron. The signal of the ChannelTron fixes the start-time of the experiment. A part of the <i>o</i> -Ps that is formed into open pores may escape from the sample (2) and may be re-emitted in the vacuum with a velocity (or temperature) that results from the interactions with the walls of the pores during its travel towards the sample surface. The emitted <i>o</i> -Ps travels in the vacuum until annihilation, with the following emission of three γ -rays (3).	23
2.1	Micro photograph of the NPD detector	30
2.2	Functional description of the NPD detector	30

2.3	DCR cumulative distribution of the NPD detector at three different excess bias voltage values	31
2.4	DCR dependence of the NPD detector from excess bias voltage	32
2.5	Measurement of the cross-talk in the NPD detector. Order of magnitude of the DCR, expressed in Hz , is reported on the colormap	33
2.6	NPD detector dynamic range	34
2.7	NPD time resolution	35
2.8	Measurement of the offset between two imposed phase delays (DCM1 and DCM2) and the values that were programmed. The measure was obtained using a Tektronix DPO Oscilloscope.	37
3.1	Scketch of the setup	40
3.2	Scketch of different geometries assumed on simulation	42
3.3	Optical cross-talk calculated in 2D array of NPD detectors that are displaced in a square grid	44
3.4	Optical cross-talk calculated in 2D array of NPD detectors that are displaced in a triangular grid	44
3.5	Optical cross-talk calculated in 2D array of NPD detectors that are displaced in a v-shape configuration.	45
4.1	Photos of the ten samples used to estimate the misalignment of the sensor with respect to the package. The last two photos have been used to extract the measurement in mm reported in table 4.1	49
4.2	Position of the hole in the plastic support and the sensor die.	50
4.3	A photo of the chip after some days of measurements.	51
4.4	FBK SRS analog SiPM.	52

4.5	Mechanical setup to hold the CMOS SPAD detector and the SiPM coupled to LYSO crystal. The Plexiglas guide used to align the FBK pixel with the crystal keeps also the sensor in the horizontal position. The SiPM is the green device attached to the aluminum holder in the photo. A 3 axis micrometer has been used to align the SiPM with the crystal.	53
4.6	Experimental setup used for the experiments with γ -ray sources. It can be noticed the position of the sources that are contained in the red and blue boxes. Two different sources (low activity ^{133}Ba and ^{22}Na) have been used to reach a number of events well discernable from the background radiation activity. The sources are positioned as close as possible to the crystal.	54
4.7	Sketch-up of the measurement	55
5.1	Simulation of light output versus DOI in a crystal of 20 mm . The detector is placed at $x = 20$ mm	61
5.2	Energy spectra of the signal read on ch1 (top), and ch2 (bottom). The values of peak positions are: ch1 1.129, ch2 1.69 [V · se - 8] The values of Energy resolutions are: ch1 46.72%, ch2 31.15 %.	64
5.3	Energy spectrum of the signal obtained by the linear combination of the two channels. Value for Energy resolutions is: 16.12%. Peak position is 3.32 [10 ⁻⁸ V · s]	65
5.4	Correlation of signals of the two SiPMs coupled at the opposite sides of a 3×3×20 mm ³ crystal coated with Teflon wrap.	65

5.5	Sketch of the simulated setup, showing the radioactive source, the crystal, the optical grease and the detector (SiPM) . . .	67
5.6	Light power distribution at the crystal interface for different points of interaction - Diffusive coating. The diffusive coating is typically obtained in experimental practice wrapping the crystal with Teflon	69
5.7	Light power distribution at the crystal interface for different points of interaction - Mirror coating	70
5.8	Angular distribution of the light output for different refractive indexes of the coupling medium: (top) Diffusive coating, and (bottom) mirror coating.	72
5.9	light transmission to the SiPM for different angles of incidence at the surface B for different mediums, i.e. the coupling grease between thr crystal and the SiPM. In the legend n is the index of refraction of such medium	73
5.10	micro-photography of bubbles between a crystals wrapped with Teflon in one experiment	75
6.1	Flux diagram of γ -ray generation loop as it is implemented in the SLitrani TGamma class. Being based on the algorithm presented in [90] the flux diagram is pretty similar to the one presented in the original article.	79
6.2	Data of Photoelectric and Compton cross sections of Aluminum as extracted from XCOM database (dashed lines) and values of σ_{KN} calculated using Klein-Nishina formula (continuous line). The values can be compared with the ones reported in [90]	81

6.3	SLitrani calculated transmission in crystals of NaI:Tl having different thickness. In figure are also reported Lambert-Beer calculation. The assumed Lambert-Beer linear attenuation coefficients are 0.31 and 0.34 [cm^{-1}].	83
7.1	Apparatus for cold <i>o</i> -Ps production and characterization of the IdEA Laboratory. Are visible: (a) exterior of the last section of the e^+ accelerator, (b) exterior of the cryostat used to cooled down the sample, (c) the ring of six PMT-based detectors.	86
7.2	Sketch up of the current PMT-based configuration and TOF measurements. The figure on left represents one of the six PMT-based detector currently mounted on the apparatus (as depicted on the right). A bounce of e^+ is linear accelerated towards a cooled porous sample of Silicon. Hitting the surface of the sample, the bounce of e^+ produced a cloud of scattered e^- (1), that is revealed by a ChannelTron. The signal of the ChannelTron fixes the start-time of the experiment. A part of the <i>o</i> -Ps that is formed into open pores may escape from the sample (2) and may be re-emitted in the vacuum with a velocity (or temperature) that results from the interactions with the walls of the pores during its travel towards the sample surface. The emitted <i>o</i> -Ps travels in the vacuum until annihilation, with the following emission of three γ -rays (3)	87
7.3	Sketch of the setup as can be built using the SiPM-based detector. depicted in the photos of figure	88
7.4	Sketch of the setup as can be built using the SiPM-based detector. depicted in the photos of figure 7.4	89

7.5	Main quantities used in the design procedure: (a) angle of view, (r) vertical resolution, (s) slit dimension, (t) thickness of the screen, (d) distance of detectors from the chamber wall, (c) chamber radius, (h) detector's ring height.	90
7.6	The raw <i>o</i> -Ps TOF spectrum (in blue) is obtained subtracting the background (in black) from the measured TOF spectra (in red), as it is measured at 10 <i>mm</i> above the sample surface. We can notice three features labeled with: A (prompt peak), B (region of the fast-hot <i>o</i> -Ps) and C (region of the slow-cold <i>o</i> -Ps).	91
7.7	Quantities used in the formalization of the design procedure. Positions of the γ -rays point sources used in the Monte-Carlo simulations	95
7.8	Figure of Merit M2 as a function of the screen thickness for a system composed by four rings of detectors. In the Monte-Carlo simulations the detectors have been placed at a distance of 100 <i>mm</i> from the chamber wall	99
7.9	Figure of merit M1 assuming a shield thickness of 2 <i>mm</i> and a distance from the chamber wall of 100 <i>mm</i> . The temperature of the <i>o</i> -Ps assumed in the calculation of M1 is 1430 <i>K</i> . The reference setup has a single ring of detectors positioned at a distance (d) of 100 <i>mm</i> from the chamber wall, a slit (s) of 4 <i>mm</i> , a chamber radius (c) of 10 <i>mm</i> , covering a 180° angle of view.	100
7.10	Figure of merit M3 as a function of the distance from the chamber wall for a system composed by four ring of detectors. In the Monte-Carlo simulations the thickness of the shield has been settled to 2 <i>mm</i>	102

-
- 7.11 Figure of merit M1 assuming a shield thickness of 2 *mm* and a distance from the chamber wall of 40 *mm* . The temperature of the *o*-Ps is 300 *K* . The reference setup has a single ring of detectors positioned at a distance (d) of 100 *mm* from the chamber wall, a slit (s) of 4 *mm* , a chamber radius (c) of 10 *mm* , covering a 180° angle of view. 102
- 7.12 A: Figure of merit M1 of a four multi-ring detector at different cold temperatures with respect to the single ring. Both setups have detectors positioned at a distance (d) of 40 *mm* from the chamber wall, a slit (s) of 4 *mm* , a chamber radius (c) of 10 *mm* . B: Contributions of the farthest detectors to the sum of figure A. 103

Acronyms:

In the electronic version links should open the corresponding web pages.

PDE	<i>Photon Detection Efficiency</i>	8
DCR	<i>Dark-Count Rate</i>	8
FWHM	<i>Full Width Half-Maximum</i>	9
e⁺	<i>positron</i>	6
e⁻	<i>electron</i>	6
Ps	<i>Positronium</i>	6
p-Ps	<i>para-positronium</i>	6
o-Ps	<i>ortho-positronium</i>	6
γ-ray	<i>Gamma-ray</i>	1
DOI	<i>Distance Of Interaction</i>	60
PMT	<i>Photo Multiplier Tube</i>	8
HPD	<i>Hybrid Photo-Detectors</i>	13
MCP-PMT	<i>Multi Channel Plate PMT</i>	10
MCP-HPD	<i>Multi Channel Plate Hybrid Photo-Detector</i>	13
GII	<i>Gated Image Intensifier Unit</i>	11
CCD	<i>Charge-Coupled Device</i>	11
SPAD	<i>Single Photon Avalanche Diode</i>	11

G-APD	<i>Geiger Avalanche Photodiode</i>	12
CMOS	<i>Complementary Metal Oxides Semiconductor</i>	13
FF	<i>Fill Factor</i>	13
SiPM	<i>Silicon Photo-Multiplier</i>	14
WLS	<i>Wave Length Shifter</i>	22
PDMS	<i>Polydimethylsiloxane</i> (wikipedia)	40
LYSO	<i>Ortho Silicate of Lutetium</i>	21
NaI:TI	<i>Sodium Iodide activated with Thallium</i>	24
YAP	<i>Yttrium Aluminum Perovskit</i>	60
BGO	<i>Bismuth Germanate</i>	60
²²Na	<i>radionuclide isotope 22 of Sodium</i>	
¹³³Ba	<i>radionuclide isotope 133 of Barium</i>	
¹⁷⁶Lu	<i>radionuclide isotope 176 of Lutetium</i>	78
NPD	<i>NAOMI-Pixel Device</i>	18
HV	<i>High Voltage</i>	16
PLL	<i>Phase Locked Loop</i>	29
FPGA	<i>Field-Programmable Gate Array</i>	20
DCM	<i>Digital Clock Manager</i>	36
LIDAR	<i>Light Detection And Ranging</i> (wikipedia)	8
CLSM	<i>Confocal Laser Scanning Microscopy</i> (wikipedia)	2
NSOM	<i>Near-field Scanning Optical Microscopy</i>	2
FRET	<i>Förster Resonance Energy Transfer</i> (wikipedia)	2
TCSPC	<i>Time Correlated Single Photon Counting</i> (wikipedia)	2
TOF	<i>Time of Flight</i>	8

DOT	<i>Diffuse Optical Tomography</i> (wikipedia)	4
PET	<i>Positron Emission Tomography</i> wikipedia	6
FLIM	<i>Florescence Lifetime Imaging Microscopy</i> (wikipedia)	2
CLI	<i>Cerenkov Luminescence Imaging</i> ([18])	7
SPADnet	<i>Single Photon Avalanche Diode network</i> (project web page) 21	
NAOMI	<i>NAno On MIcro</i> (project web page)	18
AEgIS	<i>Antihydrogen Experiment: gravity, Interferometry, Spectroscopy</i> (project web page)	22
AMS	<i>Austria Micro System</i> (foundry web page)	18
INFN	<i>Italian National Institute of Nuclear Physics</i>	15
FBK	<i>Fondazione Bruno Kessler</i> (web page)	15
SOI	<i>Smart Optical Sensors and Interfaces</i> (group web page)	18
SRS	<i>Silicon Radiation Sensors</i> (group web page)	16
IdEA	<i>Hydrogen, Energy, Environment</i> (group web page)	22
NEPOMUC	<i>Neutron induced Positron Source Munich</i> (web page) ...	88

Publications

- *Compact gamma detectors based on FBK SiPMs for a Ps Time Of Flight apparatus.* E. Mazzuca, M. Benetti, S. Mariazzi, R.S. Brusa, G.-F. Dalla Betta, C. Piemonte. *Journal of Instrumentation* (2012), submitted.
- *Simulation and characterization of different setups for gamma ray detection using SiPMs and LYSO scintillators.* M. Benetti, A. Tarolli, G. Giacomini, C. Piemonte, G.-F. Dalla Betta. *Nuclear Instruments and Methods in Physics Research*, (2011), A 10.1016/j.nima.2011.06.105
- *Characterization of a CMOS SPAD sensor designed for fluorescence lifetime spectroscopy.* M. Benetti, M. Popleteeva, L. Pancheri, G.-F. Dalla Betta, D. Stoppa. *Proceedings of IEEE Prime*, (2011), Pp. 185-188
- *CMOS Single-Photon Detector For Advanced Fluorescence Sensing Applications.* M. Benetti, M. Popleteeva, L. Pancheri, C. Collini, E. Morganti, L. Lorenzelli, L. Lunelli, L. Pasquardini, C. Pederzoli, G.-F. Dalla Betta, D. Stoppa. *Proceedings of IEEE BioPhotonics*, (2011), Pp. 1-3
- *Highly parallel SPAD detector for time-resolved lab-on-chip systems.* M. Benetti, D. Iori, L. Pancheri, F. Borghetti, L. Pasquardini, L. Lunelli, C. Pederzoli, L. Gonzo, G.-F. Dalla Betta, D. Stoppa. *Proceedings of SPIE Photonics Europe*, (2010), 77231Q